



Skolkovo Institute of Science and Technology

SIMULATIONS OF HIGH TEMPERATURE SPIN DYNAMICS

Doctoral Thesis

by

GRIGORII STARKOV

DOCTORAL PROGRAM IN PHYSICS

Supervisors

Professor Boris Fine

Professor Anatoly Dymarsky

Moscow - 2019

Abstract

The analysis of high-temperature spin dynamics is of practical importance for the development of quantum technologies based on the manipulation of nuclear spins in solids by the techniques of Nuclear Magnetic Resonance (NMR).

In this thesis, we develop a hybrid quantum-classical method for first-principles calculations of high-temperature spin dynamics. The method is based on dividing the lattice of quantum spins into a central quantum cluster and an environment, with the latter being approximated by classical spins. The quantum cluster and the classical environment interact by exerting effective magnetic fields on each other.

In order to test the method, we apply it to the calculations of Free Induction Decay (FID) in the context of NMR. Method's predictions are compared with directly computed FIDs for various one- and two- dimensional models, and with experimentally measured FIDs for real materials, such as CaF_2 , ^{29}Si -enriched silicon and calcium fluorapatite $\text{Ca}_{10}(\text{PO}_4)_6\text{F}_2$. In almost all cases considered, the excellent performance of the hybrid method is observed.

Publications

- Starkov, G. A. and Fine, B. V. Hybrid quantum-classical method for simulating high-temperature dynamics of nuclear spins in solids. *Phys. Rev. B* 98, 214421 (2018).
- Navez, P., Starkov, G. A. and Fine, B. V. Classical spin simulations with a quantum two-spin correction. *The European Physical Journal Special Topics* 227, 2013–2024 (2019).

Acknowledgements

First of all, I would like to thank professor Boris Fine for his limitless patience and unbounded optimism. The research presented in this thesis was based on a tiring process of trials and errors. I am indebted to Boris for his constant reminder not to give up and push forward.

I am grateful to Anatoly Dymarsky, Walter Hahn, Oleg Lychkovsky and Alexander Rozhkov for the fruitful discussions and their words of wisdom.

My life as a PhD student would not be so enjoyable without my fellow PhD students Anastasia Aristova and Andrei Tarkhov.

Finally, I would like to thank my wife Olga for her constant support.

This work was supported by a grant from the Russian Science Foundation (Project No.17-12-01587).

Contents

| | | |
|----------|---|-----------|
| 1 | Spin-spin relaxation in Nuclear Magnetic Resonance | 1 |
| 1.1 | Introduction | 1 |
| 1.2 | Basics of NMR | 2 |
| 1.2.1 | Non-interacting spins in external magnetic field | 2 |
| 1.2.2 | Interactions | 4 |
| 1.2.3 | Free Induction Decay | 5 |
| 1.2.4 | Unlike Spins | 9 |
| 1.3 | Theoretical setting | 12 |
| 1.4 | Literature overview | 14 |
| 1.4.1 | Analytical approaches | 14 |
| 1.4.2 | Numerical approaches | 18 |
| 1.5 | Main ideas of the thesis | 22 |
| 1.6 | Organization of the thesis | 23 |
| 2 | Properties of the infinite temperature ensemble | 25 |
| 2.1 | Distribution of wave functions in the Hilbert space | 25 |
| 2.2 | Infinite-temperature correlators of the first and the second orders | 27 |
| 2.3 | Quantum typicality | 29 |
| 2.4 | Suppression of the expectation values of quantum operators by factor $1/\sqrt{D+1}$ | 30 |
| 2.5 | Infinite-temperature correlators of arbitrary order | 31 |
| 2.6 | Symmetry of infinite-temperature correlation functions | 34 |
| 2.6.1 | The quantum case | 34 |
| 2.6.2 | The classical case | 36 |
| 3 | The Hybrid Method | 37 |
| 3.1 | Hybrid lattice and its equations of motion | 37 |
| 3.2 | Correlation functions | 40 |
| 3.3 | Uncertainty estimate | 41 |

| | | |
|----------|--|-----------|
| 4 | Application to model spin lattices | 43 |
| 4.1 | One- and two-dimensional model lattices | 43 |
| 4.2 | Discussion | 44 |
| 5 | Application of the Hybrid Method to the calculations of FIDs in real materials | 52 |
| 5.1 | FIDs in CaF_2 | 52 |
| 5.2 | FID in isotopically enriched ^{29}Si silicon | 59 |
| 5.3 | Calculation of FID in the presence of disorder and unlike spins: the case of calcium fluorapatite. | 66 |
| 5.3.1 | Structure of calcium fluorapatite | 66 |
| 5.3.2 | Defects and disorder | 68 |
| 5.3.3 | Results | 70 |
| 6 | Analysis of the Hybrid Method | 72 |
| 6.1 | Symmetry of the hybrid correlation functions | 72 |
| 6.2 | Moment expansion | 74 |
| 6.2.1 | Taylor expansion in the quantum and the classical cases | 75 |
| 6.2.2 | Taylor expansion in the hybrid case | 78 |
| 6.2.3 | Analysis of the expansion in the hybrid case | 79 |
| 7 | Conclusions and outlook | 82 |
| 7.1 | Conclusions | 82 |
| 7.2 | Outlook | 83 |
| 7.2.1 | Possible extensions | 83 |
| 7.2.2 | Applications | 84 |
| A | Details of simulations | 85 |
| A.1 | The setup of the simulation schemes | 85 |
| A.1.1 | Quantum simulations | 85 |
| A.1.2 | Classical simulations | 85 |
| A.1.3 | Hybrid simulations | 86 |
| A.2 | Scaling of statistical errors | 87 |
| A.3 | Numerical integration of equations of motion | 88 |
| A.4 | Statistics behind the plots | 89 |
| B | Overview of SpinLattice library | 91 |
| B.1 | The choice of the programming language | 91 |
| B.2 | Quick start guide | 92 |

Chapter 1

Spin-spin relaxation in Nuclear Magnetic Resonance

1.1 Introduction

The subject of this thesis is the relaxation in lattices of interacting quantum spins in the limit of infinite temperature. The study of this particular class of problems is largely motivated by the task of first-principles calculation of the Free Induction Decay (FID) in solids in the context of Nuclear Magnetic Resonance (NMR). Aside from this narrowly focused context, however, the choice of this particular setup is also dictated by a few theoretical considerations of a general character. First, the problem is representative of a much broader class of non-perturbative non-equilibrium phenomena in the regime of strong dynamical correlations. Therefore, a new method for solving the NMR FID problem is likely to have applications to other settings. Secondly, spin systems are simpler than the ones containing translational degrees of freedom, because Hilbert spaces of the constituent spins, as well as that of the whole system, are finite, which makes them more amenable to numerical simulations.

Interacting spins on a regular lattice typically exhibit non-Markovian dynamics, because there is no clear separation of time-scales: dynamics of macroscopic observables takes place on the same characteristic time-scale as the motion of individual spins. As a consequence, the analytical solutions are available only for a handful of integrable cases. Despite the finiteness of Hilbert space, the direct numerical approach is not fruitful either, because the required computing resources scale exponentially with the number of spins, which strongly limits the size of a system amenable to direct treatment. It is, certainly, a limitation, because we are interested in lattices large enough, so that finite size effects can be neglected. In light of these facts, the development of new efficient approximate numerical

methods gains prominent importance.

Determination of the FID shape in solids is a very well defined problem in the context of NMR. The existing theory allows reliable determination of the coupling constants between nuclear spins as well as their interaction with external magnetic fields. The task of first-principles FID calculations is to obtain the FID shape given the particular set of coupling constants. In a typical NMR experiment, the largest energy scale is determined by the temperature. The energy of Zeeman coupling with the external magnetic field and the energy of inter-nuclear couplings are much smaller. As a result, our interest in this type of problems naturally leads us to consider the infinite temperature limit. It should be also noted that the limit of infinite temperature is interesting in its own right from the theoretical point of view: the equilibrium correlations are nonexistent in this case, yet the dynamical correlations are highly non-trivial due to their non-Markovian character.

1.2 Basics of NMR

In this Section, I briefly discuss the basics of NMR. A detailed account of the theory can be found in the NMR textbooks, e.g., [1] and [2].

Here and mostly throughout the thesis, I will use the convention that reduced Planck constant \hbar is equal to 1. The care is only required when comparing the results of simulations with experimental data: in this case, one needs to keep track of \hbar explicitly.

1.2.1 Non-interacting spins in external magnetic field

The Hamiltonian of a free quantum spin in external magnetic field \mathbf{B} is

$$\mathcal{H} = -\gamma \mathbf{S} \cdot \mathbf{B}, \quad (1.1)$$

where γ is the gyromagnetic ratio and $\mathbf{S} \equiv (S^x, S^y, S^z)$ is a vector of spin projection operators. With the help of the spin commutation relations

$$-i [S^\alpha, S^\beta] = \varepsilon_{\alpha\beta\gamma} \cdot S^\gamma, \quad (1.2)$$

one is able to derive the equations of motion in Heisenberg representation:

$$\dot{\mathbf{S}} = -i [\mathbf{S}, \mathcal{H}] = \gamma \mathbf{S} \times \mathbf{B}. \quad (1.3)$$

The classical counterpart of this system is described by a classical vector of angular momentum $\mathbf{s} \equiv (s^x, s^y, s^z)$ with associated magnetic momentum $\gamma \mathbf{s}$. Sim-

ilarly to the quantum case, the Hamiltonian takes the form

$$H = -\gamma \mathbf{s} \cdot \mathbf{B}, \quad (1.4)$$

and the equations of motion can be derived with the use of Poisson brackets [3, 4]

$$\{s^\alpha, s^\beta\}_P = e^{\alpha\beta\gamma} s^\gamma, \quad (1.5)$$

from which it follows that

$$\dot{\mathbf{s}} = \{\mathbf{s}, H\}_P = \gamma \mathbf{s} \times \mathbf{B}. \quad (1.6)$$

If we take the quantum average of equation (1.3) with respect to some quantum state, we get precisely the classical equation (1.6), provided we identify components of vector \mathbf{s} with quantum expectation values of spin projections. Thus, as far as the dynamics of a single spin in an external magnetic field is concerned, we can use the classical picture. The motion of a spin is the precession around the direction of the external magnetic field with Larmor frequency $\Omega = -\gamma B$. Here, the negative sign of the frequency corresponds to the counter-clockwise precession around the direction of the external magnetic field.

Let us now consider a spin in a static magnetic field \mathbf{B}_0 , whose direction we choose as the z -axis. Let us also apply a transverse magnetic field \mathbf{B}_\perp rotating with angular frequency ω . We identify its initial direction with the x -axis. The full external magnetic field is

$$\mathbf{B} = B_\perp (\hat{x} \cos \omega t + \hat{y} \sin \omega t) + B_0 \hat{z}. \quad (1.7)$$

It is convenient to switch to a reference frame rotating together with the transverse field \mathbf{B}_\perp . If we assume that the x - and the y -axes of the laboratory and the rotating frames coincide at $t = 0$, then the precession of the spin in the rotating frame is determined by the effective magnetic field of the form

$$\mathbf{B}_{\text{rot}} = B_\perp \hat{x} + \left(B_0 + \frac{\omega}{\gamma} \right) \hat{z}. \quad (1.8)$$

The expression for the z -component of \mathbf{B}_{rot} can be easily understood from the following argument. Let us assume that there is no transverse field and switch to the reference frame rotating with angular velocity $\omega \hat{z}$. In the new frame, the spin precesses with the angular velocity $(\Omega - \omega)$, which is produced by the effective magnetic field $(\Omega - \omega)/(-\gamma) \cdot \hat{z}$.

If the resonance condition $\omega = \Omega$ is fulfilled, the z -component of \mathbf{B}_{rot} is absent.

Hence, the spin precesses around the x -axis. If initially it was aligned with the static field \mathbf{B}_0 , then even a small resonant transverse field can produce large deviations in the direction of the spin.

NMR experiments usually use linearly polarized oscillating transverse field of amplitude much smaller than \mathbf{B}_0 , which is equivalent to the superposition of two rotating fields with angular frequencies ω and $-\omega$. If one of the components fulfills the resonance condition, the other one may be neglected, since it is far from resonance and, hence, its effect is small.

From the point of view of Quantum Mechanics, the resonant oscillating field induces transitions between adjacent energy levels. Provided we have the thermal distribution of occupancies, the net redistribution caused by transitions will increase the energy, meaning, the system will strongly absorb the energy pumped by the oscillating field. When an absorption spectrum of a spin system is measured, the peak centered on the Larmor frequency is observed. If different nuclear species with different gyromagnetic ratios are present, several peaks are observed, and the relative concentrations of different species can be determined by comparing the heights of the peaks.

1.2.2 Interactions

In reality, nuclear spins interact also with the fluctuating magnetic fields produced by the spins themselves and by other degrees of freedom of the solid, which include electrons and phonons¹. These interactions cause the finite width of absorption peaks.

The strongest interactions are with other nuclei and with electrons. In the case of electrons, we should distinguish the electrons of ionic cores and chemical bonds and conduction electrons. The common effect of both the conduction and the core electrons is the adjustment of local static fields sensed by nuclei. This adjustment is due to the magnetic susceptibility of electrons, and it leads to the shift of Larmor frequency. Depending on whether this effect is produced by the conduction electrons or the core electrons, it is called “Knight shift” or “Chemical shift” respectively. Additionally, the conduction electrons contribute to the energy relaxation of the nuclear subsystem and serve as the mediators for the transferred hyperfine coupling between the nuclear spins.

The interaction of the nuclear spins with phonons also contributes to the energy relaxation of the nuclear subsystem.

¹Electrons and phonons interact between each other themselves. As a consequence, it is more correct to think in terms of the dressed quasiparticles corresponding to electrons and phonons.

Typical hierarchy of energy scales in solid-state NMR experiments is

$$\beta^{-1} \gg \Omega \gg T_2^{-1} \gg T_1^{-1}, \quad (1.9)$$

where T_1 is the time-scale characterizing the energy relaxation of the nuclear subsystem, T_2 is the time-scale characterizing the dephasing of the nuclear subsystem due to the spin-spin interactions² and $\beta = 1/(k_B T)$ is the inverse temperature. Here, T is the temperature of the solid, and k_B is the Boltzmann constant. Since we are interested in the dynamics on the time-scale T_2 , we can safely neglect the effects of energy relaxation.

In this thesis, we consider FID calculations for non-magnetic dielectrics³, thus the effects of transferred hyperfine coupling may be neglected. Also, we focus on spins 1/2.

The relevant type of interactions for us is magnetic dipolar interactions between nuclear spins. The whole Hamiltonian including the Zeeman term then takes the form

$$\mathcal{H} = - \sum_i \gamma_i \mathbf{S}_i \cdot \mathbf{B}_i + \sum_{i < j} \frac{\gamma_i \gamma_j}{r_{ij}^2} \left[\mathbf{S}_i \cdot \mathbf{S}_j - 3 \frac{(\mathbf{S}_i \cdot \mathbf{r}_{ij})(\mathbf{S}_j \cdot \mathbf{r}_{ij})}{r_{ij}^2} \right], \quad (1.10)$$

where i are the lattice indices, $\mathbf{r}_{ij} = \mathbf{r}_j - \mathbf{r}_i$ are radius-vectors connecting different lattice sites and γ_i are fundamental nuclear gyromagnetic ratios⁴. The local static fields \mathbf{B}_i take into account the adjustments due to the magnetic response of surrounding electrons.

1.2.3 Free Induction Decay

Let us assume that all the nuclei are the same and have equivalent chemical environments as happens in some simple solids. A Free Induction Decay experiment is arranged in the following manner. A sample is placed into a large static external magnetic field \mathbf{B}_0 , the direction of which we identify with the z -axis. As a result, the sample gains a net macroscopic magnetization \mathbf{M} along the field. A short

²Since the energy is dominated by the Zeeman term, T_1 corresponds to the relaxation of the longitudinal component of magnetization. At the same time, T_2 corresponds to the relaxation of the transversal component of magnetization.

³Isotopically enriched ²⁹Si silicon, which we consider in Section 5.2, is a semiconductor. However, the concentration of charge carriers at temperatures of the experiment is low, which, for our purposes, makes this material similar to a dielectric.

⁴Sometimes, the shielding of the static magnetic field is absorbed into the definition of γ in the NMR literature. The resulting effective gyromagnetic ratios are convenient to use if one is concerned only with the positions of the absorption peaks. Since, as explained in the following subsections, the FID signal characterizes the form of the absorption peak, the position of the peak is irrelevant. Thus, everywhere in the thesis, we understand by γ the fundamental gyromagnetic ratio which is an intrinsic characteristic of the nuclei under consideration.

resonant pulse now rotates the magnetization by $\pi/2$ with respect to the y -axis, so that it now lies in the xy -plane. Let us identify the x -axis with the direction of magnetization just after the pulse. The total magnetic field experienced by each spin is the sum of the static external field and the fluctuating fields produced by other spins. As a consequence, the macroscopic magnetization will precess with Larmor frequency around the direction of the static field, but its amplitude will decay due to the dephasing by the fields fluctuating in space in time:

$$\mathbf{M}(t) = M_e(t) \cdot (\hat{x} \cos \Omega t + \hat{y} \sin \Omega t), \quad (1.11)$$

where $M_e(t)$ is a decaying function of time characterized by the timescale T_2 . The function of $M_e(t)$ is referred to as the “free induction decay” or FID.

The rotation of transverse magnetization is detected by a coil. Without the loss of generality, let us assume that the coil axis coincides with the x -axis. The voltage induced in the coil is proportional to the derivative of the x -component of the magnetization:

$$V(t) \propto \dot{M}_x(t) \simeq \Omega M_e(t) \sin \Omega t, \quad (1.12)$$

where we have used the fact that $\dot{M}_e/M_e \sim 1/T_2 \ll \Omega$. Comparing Eq. (1.12) with Eq. (1.11), we see that the envelope of the detected voltage signal gives us the relaxation $M_e(t)$ of magnetization in the reference frame rotating with Larmor frequency.

Let us discuss each of the above steps more thoroughly. The Hamiltonian of the system is

$$\mathcal{H} = \mathcal{H}_0 + \mathcal{H}_{dip}, \quad (1.13)$$

where

$$\mathcal{H}_0 = -\gamma B_0 \sum_i S_i^z, \quad (1.14)$$

and

$$\mathcal{H}_{dip} = \sum_{i < j} \frac{\gamma^2}{r_{ij}^2} \left[\mathbf{S}_i \cdot \mathbf{S}_j - 3 \frac{(\mathbf{S}_i \cdot \mathbf{r}_{ij})(\mathbf{S}_j \cdot \mathbf{r}_{ij})}{r_{ij}^2} \right]. \quad (1.15)$$

Let us also introduce operators of the total spin polarization along each of the axes:

$$\mathcal{M}_\alpha = \sum_i S_i^\alpha. \quad (1.16)$$

We will call it “magnetization”⁵ The density matrix prior to the application of the

⁵The real definition of magnetization requires Eq. (1.16) to be multiplied by the factor γ , which we chose to omit. It is completely safe to do so unless there are several spin species with different gyromagnetic ratios present.

pulse is

$$\rho_{eq} = \frac{1}{Z} e^{-\beta\mathcal{H}} \simeq \frac{1}{Z} [\mathbb{1} - \beta\mathcal{H}_0] = \frac{1}{Z} \mathbb{1} + \frac{\beta\gamma B}{Z} \mathcal{M}_z, \quad (1.17)$$

where Z is the partition function. The expansion of the exponent and the omission of the dipole-dipole part of the Hamiltonian is justified by the hierarchy of energy scales (see Eq. (1.9)). After the pulse, \mathcal{M}_z is rotated into \mathcal{M}_x , so that the density matrix acquires the form

$$\rho(0) = \frac{1}{Z} \mathbb{1} + \frac{\beta\gamma B}{Z} \mathcal{M}_x, \quad (1.18)$$

where we identified the moment just after the pulse with $t = 0$. The average value of the x -component of magnetization at time t is then

$$M_x(t) = \text{Tr} [e^{i\mathcal{H}t} \mathcal{M}_x e^{-i\mathcal{H}t} \rho(0)]. \quad (1.19)$$

When we substitute Eq. (1.18) here, only the term proportional to \mathcal{M}_x leads to a non-vanishing contribution because $\text{Tr} [e^{i\mathcal{H}t} \mathcal{M}_x e^{-i\mathcal{H}t}] = \text{Tr} [\mathcal{M}_x] = 0$. Thus, the average value of magnetization is proportional to an auto-correlation function:

$$M_x(t) \propto \text{Tr} [e^{i\mathcal{H}t} \mathcal{M}_x e^{-i\mathcal{H}t} \mathcal{M}_x]. \quad (1.20)$$

To analyze this expression further, it is useful to switch to an interaction representation with respect to the Zeeman part \mathcal{H}_0 of the Hamiltonian. For the homo-nuclear case, it is equivalent to switching to the reference frame rotating with the Larmor frequency. Let us introduce the operator of the time evolution in the interaction representation:

$$\mathcal{U}(t) = e^{-i\mathcal{H}t} e^{i\mathcal{H}_0 t}, \quad (1.21)$$

$$\dot{\mathcal{U}}(t) = e^{-i\mathcal{H}t} i(\mathcal{H}_0 - \mathcal{H}) e^{i\mathcal{H}_0 t} = -i\mathcal{U} e^{-i\mathcal{H}_0 t} \mathcal{H}_{dip} e^{i\mathcal{H}_0 t} = -i\mathcal{U}(t) \tilde{\mathcal{H}}_{dip}(t). \quad (1.22)$$

(Note that the order of operators is different from the way it is usually done for the interaction representation. The idea and the derivation is similar, however.) Using operator \mathcal{U} and the invariance of trace under the cyclic permutations of operators, one can rewrite the Eq. (1.20) in the form

$$\begin{aligned} \text{Tr} [e^{i\mathcal{H}t} \mathcal{M}_x e^{-i\mathcal{H}t} \mathcal{M}_x] &= \text{Tr} [e^{i\mathcal{H}_0 t} \mathcal{U}^\dagger(t) \mathcal{M}_x \mathcal{U}(t) e^{-i\mathcal{H}_0 t} \mathcal{M}_x] = \\ &= \text{Tr} [\mathcal{U}^\dagger(t) \mathcal{M}_x \mathcal{U}(t) e^{-i\mathcal{H}_0 t} \mathcal{M}_x e^{i\mathcal{H}_0 t}]. \end{aligned} \quad (1.23)$$

The commutation relations for magnetization operators \mathcal{M}_α are the same as for the single spin operators, hence $e^{-i\mathcal{H}_0 t} \mathcal{M}_x e^{i\mathcal{H}_0 t} = e^{-i\Omega\mathcal{M}_z t} \mathcal{M}_x e^{i\Omega\mathcal{M}_z t} = \mathcal{M}_x \cos \Omega t +$

$\mathcal{M}_y \sin \Omega t$. When \mathcal{H}_{dip} is transformed into $\tilde{\mathcal{H}}_{dip}(t)$, the terms of \mathcal{H}_{dip} which do not commute with \mathcal{H}_0 acquire factors oscillating with frequencies which are multiples of Ω . Since we are interested in the dynamics on the time-scale $T_2 \gg 1/\Omega$, we can neglect these rapidly oscillating terms while solving Eq. (1.22). As a consequence, the operator \mathcal{U} can be approximated as

$$\mathcal{U} \simeq e^{-i\mathcal{H}'_{dip}t}, \quad (1.24)$$

where \mathcal{H}'_{dip} is the part of \mathcal{H}_{dip} commuting with \mathcal{H}_0 . Its explicit form is the following [5], [1, chapter 4]:

$$\mathcal{H}'_{dip} = \sum_{i < j} \frac{\gamma^2(1 - 3 \cos^2 \theta_{ij})}{r_{ij}^3} \left[S_i^z S_j^z - \frac{1}{2}(S_i^x S_j^x + S_i^y S_j^y) \right]. \quad (1.25)$$

Substituting it into Eq. (1.23), we get

$$\begin{aligned} \text{Tr} \left[e^{i\mathcal{H}t} \mathcal{M}_x e^{-i\mathcal{H}t} \mathcal{M}_x \right] &= \\ &= \text{Tr} \left[e^{i\mathcal{H}'_{dip}t} \mathcal{M}_x e^{-i\mathcal{H}'_{dip}t} \mathcal{M}_x \right] \cos \Omega t + \text{Tr} \left[e^{i\mathcal{H}'_{dip}t} \mathcal{M}_x e^{-i\mathcal{H}'_{dip}t} \mathcal{M}_y \right] \sin \Omega t \end{aligned} \quad (1.26)$$

The second correlator is equal to zero. It is easy to see if we apply a unitary transformation corresponding to a rotation by π along the x -axis: operators \mathcal{M}_x , \mathcal{H}'_{dip} and the trace itself do not change, but \mathcal{M}_y acquires a negative sign. Finally, we get that

$$M_x(t) \propto \text{Tr} \left[e^{i\mathcal{H}'_{dip}t} \mathcal{M}_x e^{-i\mathcal{H}'_{dip}t} \mathcal{M}_x \right] \cos \Omega t. \quad (1.27)$$

By comparing it with Eq. (1.11), we see that the envelope of the signal detected in a FID experiment is proportional to the auto-correlation function of transverse magnetization in the reference frame rotating with Larmor frequency:

$$M_e(t) \propto C(t) = \text{Tr} \left[e^{i\mathcal{H}'_{dip}t} \mathcal{M}_x e^{-i\mathcal{H}'_{dip}t} \mathcal{M}_x \right]. \quad (1.28)$$

The FID is intimately linked to the line-shape function $f(u)$ of the absorption spectrum in the vicinity of the Larmor frequency. If we center the function on the position of the peak, so that $u = 0$ corresponds to the Larmor frequency, then the line shape is given by the Fourier transform of the correlation function $C(t)$ [6], [1, Chapter 4]:

$$f(u) = \mathcal{A} \cdot \int_0^{+\infty} dt C(t) \cos ut, \quad (1.29)$$

where \mathcal{A} is a normalization constant. Intuitively, it is an expected result, because $C(t)$ is a response to a quench perturbation of the system, which excites all the

frequencies in a broad window around the resonant one. Conversely, the inverse transform is

$$C(t) = \frac{2}{\pi\mathcal{A}} \cdot \int_{-\infty}^{+\infty} du f(u) \cos ut. \quad (1.30)$$

1.2.4 Unlike Spins

Let us now consider FID for the case of two types of nuclei with different gyromagnetic ratios present in the system. A pair of nuclear spins with different gyromagnetic ratios are referred in the NMR literature as “unlike spins”. We denote by S_i^σ the spin projection operators for the first group and by I_k^σ — the spin projection operators for the second group of nuclei. Let us also assume that the respective Larmor frequencies Ω_S and Ω_I of S and I nuclei are well separated, i.e. their difference is much smaller than $1/T_2$. By tuning the pulse frequency in resonance with either of the Larmor frequencies, it is possible to observe the FID of either of the groups of nuclei. We will focus on the FID of S spins. Here we elaborate the adjustments to the theory that should be made in order to take into account the presence of unlike spins (see also [1, Chapter 4.3]). The treatment of unlike spins is important for the calculations of FID in calcium fluorapatite in Section 5.3.

The full Hamiltonian of the system takes the form

$$\mathcal{H} = \mathcal{H}_0 + \mathcal{H}_{dip}, \quad (1.31)$$

$$\mathcal{H}_0 = -\gamma_S B \sum_i S_i^z - \gamma_I B \sum_k I_k^z, \quad (1.32)$$

$$\mathcal{H}_{dip} = \mathcal{H}_{SS} + \mathcal{H}_{SI} + \mathcal{H}_{II}, \quad (1.33)$$

$$\mathcal{H}_{SS} = \sum_{i<j} \frac{\gamma_S^2}{r_{ij}^2} \left[\mathbf{S}_i \cdot \mathbf{S}_j - 3 \frac{(\mathbf{S}_i \cdot \mathbf{r}_{ij})(\mathbf{S}_j \cdot \mathbf{r}_{ij})}{r_{ij}^2} \right], \quad (1.34)$$

$$\mathcal{H}_{II} = \sum_{k<l} \frac{\gamma_I^2}{r_{kl}^2} \left[\mathbf{I}_k \cdot \mathbf{I}_l - 3 \frac{(\mathbf{I}_k \cdot \mathbf{r}_{kl})(\mathbf{I}_l \cdot \mathbf{r}_{kl})}{r_{kl}^2} \right], \quad (1.35)$$

$$\mathcal{H}_{SI} = \sum_{i,k} \frac{\gamma_S \gamma_I}{r_{ik}^2} \left[\mathbf{S}_i \cdot \mathbf{I}_k - 3 \frac{(\mathbf{S}_i \cdot \mathbf{r}_{ik})(\mathbf{I}_k \cdot \mathbf{r}_{ik})}{r_{ik}^2} \right], \quad (1.36)$$

where γ_S and γ_I are the gyromagnetic ratios of S and I nuclei respectively. The $\pi/2$ pulse rotates magnetization only of the S nuclei, so that just after the pulse the density matrix takes the form

$$\rho(0) = \frac{1}{Z} \mathbb{1} + \frac{\beta \gamma_S B}{Z} \mathcal{M}_x^S + \frac{\beta \gamma_I B}{Z} \mathcal{M}_z^I, \quad (1.37)$$

where we have defined

$$\mathcal{M}_\alpha^S = \sum_i S_i^\alpha, \quad \mathcal{M}_\alpha^I = \sum_k I_k^\alpha. \quad (1.38)$$

The average value of x -component of total spin polarization at time t is⁶

$$M_x(t) \propto G_x(t) = \text{Tr} \left[e^{i\mathcal{H}t} \left(\mathcal{M}_x^S + \frac{\gamma_I}{\gamma_S} \mathcal{M}_x^I \right) e^{-i\mathcal{H}t} \left(\mathcal{M}_x^S + \frac{\gamma_I}{\gamma_S} \mathcal{M}_z^I \right) \right]. \quad (1.39)$$

By analogy with the case of a homo-nuclear system, we introduce the interaction representation with respect to the Zeeman part \mathcal{H}_0 of the Hamiltonian (see Eqs. (1.21), (1.22) and (1.23)):

$$\mathcal{U}(t) = e^{-i\mathcal{H}t} e^{i\mathcal{H}_0 t}, \quad (1.40)$$

$$\dot{\mathcal{U}}(t) = e^{-i\mathcal{H}t} i(\mathcal{H}_0 - \mathcal{H}) e^{i\mathcal{H}_0 t} = -i\mathcal{U} e^{-i\mathcal{H}_0 t} \tilde{\mathcal{H}}_{dip} e^{i\mathcal{H}_0 t} = -i\mathcal{U}(t) \tilde{\mathcal{H}}_{dip}(t). \quad (1.41)$$

Substituting this definition into Eq. (1.39) and using the invariance of the trace with respect to the cyclic permutations of the operators, we get

$$G_x(t) = \text{Tr} \left[\mathcal{U}^\dagger \left(\mathcal{M}_x^S + \frac{\gamma_I}{\gamma_S} \mathcal{M}_x^I \right) \mathcal{U} e^{-i\mathcal{H}_0 t} \left(\mathcal{M}_x^S + \frac{\gamma_I}{\gamma_S} \mathcal{M}_z^I \right) e^{i\mathcal{H}_0 t} \right]. \quad (1.42)$$

As in the previous Section, the same arguments about the averaging out of the fast oscillating terms of the dipolar-dipolar part $\tilde{\mathcal{H}}_{dip}(t) = \tilde{\mathcal{H}}_{SS}(t) + \tilde{\mathcal{H}}_{SI}(t) + \tilde{\mathcal{H}}_{II}(t)$ of the Hamiltonian in the interaction representation can be applied. Therefore, the operator \mathcal{U} can be approximated with a good accuracy by

$$\mathcal{U} = e^{-i\mathcal{H}'_{dip} t}, \quad (1.43)$$

where

$$\mathcal{H}'_{dip} = \mathcal{H}'_{SS} + \mathcal{H}'_{SI} + \mathcal{H}'_{II}, \quad (1.44)$$

$$\mathcal{H}'_{SS} = \sum_{i<j} \frac{\gamma_S^2 (1 - 3 \cos^2 \theta_{ij})}{r_{ij}^3} \left[S_i^z S_j^z - \frac{1}{2} (S_i^x S_j^x + S_i^y S_j^y) \right], \quad (1.45)$$

$$\mathcal{H}'_{II} = \sum_{k<l} \frac{\gamma_I^2 (1 - 3 \cos^2 \theta_{kl})}{r_{kl}^3} \left[I_k^z I_l^z - \frac{1}{2} (I_k^x I_l^x + I_k^y I_l^y) \right], \quad (1.46)$$

$$\mathcal{H}'_{SI} = \sum_{i,k} \frac{\gamma_S \gamma_I (1 - 3 \cos^2 \theta_{ik})}{r_{ik}^3} S_i^z I_k^z. \quad (1.47)$$

The justification of the approximation is completely analogous to the case of a

⁶Since we omitted the gyromagnetic ratio from the definition of magnetization, if the magnetizations of different types of spins appear in one equation, we need to rescale one of the contributions by the ratio of gyromagnetic ratios.

homo-nuclear system with the exception of $\tilde{\mathcal{H}}_{SI}(t)$ part of the dipolar-dipolar interaction. Non-secular terms oscillate with frequencies $\Omega_S \pm \Omega_I$ in this case. As a consequence, for our arguments to be valid, we need to require $|\Omega_S \pm \Omega_I|$ to be much larger than the energy scale $1/T_2$ of the spin-spin interactions.

With the use of this approximation, the Eq. (1.39) is rewritten in the form

$$G_x(t) = \text{Tr} \left[e^{i\mathcal{H}'_{\text{dip}}t} \left(\mathcal{M}_x^S + \frac{\gamma_I}{\gamma_S} \mathcal{M}_x^I \right) e^{-i\mathcal{H}'_{\text{dip}}t} \left(\mathcal{M}_x^S \cos \Omega_S t + \mathcal{M}_y^S \sin \Omega_S t + \frac{\gamma_I}{\gamma_S} \mathcal{M}_z^I \right) \right]. \quad (1.48)$$

Let us denote $\overline{A(t)B} = \text{Tr} \left[e^{i\mathcal{H}'_{\text{dip}}t} A e^{-i\mathcal{H}'_{\text{dip}}t} B \right]$. The Eq. (1.48) contains six different correlators:

$$\begin{array}{lll} 1. \overline{\mathcal{M}_x^S(t)\mathcal{M}_x^S}, & 2. \overline{\mathcal{M}_x^S(t)\mathcal{M}_y^S}, & 3. \overline{\mathcal{M}_x^S(t)\mathcal{M}_z^I}, \\ 4. \overline{\mathcal{M}_x^I(t)\mathcal{M}_x^S}, & 5. \overline{\mathcal{M}_x^I(t)\mathcal{M}_y^S}, & 6. \overline{\mathcal{M}_x^I(t)\mathcal{M}_z^I}. \end{array} \quad (1.49)$$

For each of the correlators except for the first one it is possible to specify a unitary transformation which changes only the sign of the second \mathcal{M} operator and, hence, the sign of the correlator itself. In particular: rotation of S spins by π around the z -axis changes the signs of the third, the fourth and the fifth correlators; rotation of I spins by π around the z -axis changes the sign of the sixth correlator; simultaneous rotation of S and I spins by π around the x -axis changes the sign of the second correlator. Since the trace is invariant with respect to unitary transformations, all the correlators except for the first one are equal to zero.

As a result,

$$G_x(t) = \text{Tr} \left[e^{i\mathcal{H}'_{\text{dip}}t} \mathcal{M}_x^S e^{-i\mathcal{H}'_{\text{dip}}t} \mathcal{M}_x^S \right] \cos \Omega_S t. \quad (1.50)$$

The envelope of the signal is proportional to the coefficient of $\cos \Omega_S t$:

$$M_e(t) \propto C_x(t) = \text{Tr} \left[e^{i\mathcal{H}'_{\text{dip}}t} \mathcal{M}_x^S e^{-i\mathcal{H}'_{\text{dip}}t} \mathcal{M}_x^S \right]. \quad (1.51)$$

As in the the homo-nuclear case, the FID is determined by the auto-correlation function of the total magnetization of the nuclear species responding to the $\pi/2$ pulse. At the same time, there is an additional dephasing due to the interactions with unlike spins.

1.3 Theoretical setting

In this thesis, we consider lattices of quantum spins 1/2 with translationally invariant Hamiltonians of the general form:

$$\mathcal{H} = \sum_{\alpha, i < j} J_{i,j}^{\alpha} S_i^{\alpha} S_j^{\alpha}, \quad \alpha \in \{x, y, z\}, \quad (1.52)$$

where S_i^{α} is the operator of spin projection on axis α for the i -th lattice site, and $J_{i,j}^{\alpha}$ are the coupling constants. In principle, it is possible to consider interaction terms with couplings between different projections of spins, which is the case, for example, for the full magnetic dipole-dipole interaction (see Eq. 1.15). Nevertheless, the form of the Hamiltonian described in Eq. (1.52) is sufficient for our goals, largely focused around the problem of FID calculations, since the truncated dipole-dipole interactions $\mathcal{H}'_{\text{dip}}$ both in homo- and hetero-nuclear cases (Eqs. (1.25) and (1.44) respectively) belong to the general class of interactions described by Eq. (1.52). At the same time, it is worth noting that the results of the thesis can be naturally extended to an even more general class of Hamiltonians.

Our considerations are equally true for Bravais lattices and for lattices with non-trivial unit cells (see [7, Chapter 4] for definitions). Additionally, we apply periodic boundary conditions in order to preserve the translational invariance.

Similar to the free spin case, one can use extended commutation relations

$$-i [S_i^{\alpha}, S_j^{\beta}] = \delta_{i,j} \cdot \varepsilon_{\alpha\beta\gamma} \cdot S_i^{\gamma}, \quad (1.53)$$

to obtain the equations of motion for the spin projection operators in the Heisenberg representation:

$$\dot{\mathbf{S}}_i = -i [\mathbf{S}_i, \mathcal{H}] = \mathbf{S}_i \times \mathbf{h}_i^{\mathcal{Q}\mathcal{Q}}, \quad (1.54)$$

where

$$\mathbf{h}_i^{\mathcal{Q}\mathcal{Q}} = - \sum_{j \neq i} \begin{pmatrix} J_{i,j}^x S_j^x \\ J_{i,j}^y S_j^y \\ J_{i,j}^z S_j^z \end{pmatrix} \quad (1.55)$$

is the operator of the local magnetic field acting on spin i .

The quantities of our interest are time auto-correlation functions of the total spin polarization $\mathcal{M}_{\alpha} = \sum_i S_i^{\alpha}$

$$C_{\alpha}(t) = \langle \mathcal{M}_{\alpha}(t) \mathcal{M}_{\alpha}(0) \rangle = \frac{1}{D} \text{Tr} [\mathcal{M}_{\alpha}(t) \mathcal{M}_{\alpha}(0)], \quad (1.56)$$

where $\langle \dots \rangle$ denotes the averaging over the infinite temperature equilibrium state, which is equivalent to taking a trace, and D is the dimensionality of the Hilbert

space.

In general, $C_\alpha(t)$ decays on the fastest microscopic timescale of the system characterized by the inverse root-mean-squared value of local fields $\mathbf{h}_i^{\mathcal{Q}\mathcal{Q}}$ given by Eq. (1.55) experienced by each spin (see Eq. (2.27)):

$$\tau_c = \left(\sum_j J_{ij}^{x^2} \langle S_j^{x^2} \rangle + J_{ij}^{y^2} \langle S_j^{y^2} \rangle + J_{ij}^{z^2} \langle S_j^{z^2} \rangle \right)^{-1/2}. \quad (1.57)$$

As a consequence, it is impossible to apply the approximations based on the separation of time-scales.

In order to correctly reproduce the properties of macroscopic systems, we need to consider the lattices large enough, so that the finite size effects are not important. At the same time, direct numerical calculation of $C_\alpha(t)$ for large lattice sizes is not feasible due to the exponentially large Hilbert spaces involved.

The infinite-temperature auto-correlation functions has an important property of being the even functions of time: $C_\alpha(t) = C_\alpha(-t)$. For the correlation functions given by Eq. (1.56), it follows from the invariance of the trace under cyclic permutations of operators:

$$\begin{aligned} \text{Tr} [\mathcal{M}_\alpha(t)\mathcal{M}_\alpha(0)] &= \text{Tr} [e^{i\mathcal{H}t}\mathcal{M}_\alpha e^{-i\mathcal{H}t}\mathcal{M}_\alpha] = \text{Tr} [\mathcal{M}_\alpha e^{-i\mathcal{H}t}\mathcal{M}_\alpha e^{i\mathcal{H}t}] = \\ &= \text{Tr} [\mathcal{M}_\alpha(0)\mathcal{M}_\alpha(-t)] = \text{Tr} [\mathcal{M}_\alpha(-t)\mathcal{M}_\alpha(0)]. \end{aligned} \quad (1.58)$$

Additionally, we can use the translational invariance of the system to recast the auto-correlation functions (1.56) in the form, which makes the spatial structure of the correlations easier to understand. Indeed, it follows from translational invariance that

$$\langle \mathcal{M}_\alpha(t)\mathcal{M}_\alpha(0) \rangle = \sum_i \langle S_i^\alpha(t)\mathcal{M}_\alpha(0) \rangle = N_{\text{cells}} \cdot \sum_{i \in \text{unit cell}} \langle S_i^\alpha(t)\mathcal{M}_\alpha(0) \rangle, \quad (1.59)$$

where N_{cells} is the number of unit cells the lattice is comprised of, and the last summation goes over the lattice sites of some arbitrary unit cell. Moreover, if the unit cell is trivial or all the lattice sites in a unit cell are equivalent (transformed into each other by discrete symmetries of the lattice), then we can omit the sum over a unit cell in Eq. (1.59) completely, so that a spin is correlated with the rest of the lattice (N_{cells} should be replaced by the number of lattice spins N in this case). More generally, if we consider a set of lattice sites \mathcal{Q}' which consists of

arbitrary full unit cells and has $N_{\mathcal{Q}'}$ spins, then we can write

$$C_{\alpha}(t) = \frac{N}{N_{\mathcal{Q}'}} \cdot \langle \mathcal{M}'_{\alpha}(t) \mathcal{M}_{\alpha}(0) \rangle, \quad \mathcal{M}'_{\alpha} = \sum_{i \in \mathcal{Q}'} S_i^{\alpha}. \quad (1.60)$$

Analogously, if the unit cell is trivial or all the lattice sites in a basis cell are equivalent, we can choose \mathcal{Q}' to be an arbitrary set of $N'_{\mathcal{Q}}$ lattice spins.

1.4 Literature overview

1.4.1 Analytical approaches

The problem of the NMR FID calculations from first principles, or, equivalently, the problem of the line-shape of the NMR absorption peak has a long history.

The first theoretical description of NMR relaxation was given by Bloch in 1946 [8]. Bloch phenomenologically introduced two exponential relaxation processes with respective time constants T_1 and T_2 . The former was the relaxation of the longitudinal component of magnetization due to thermal agitation. The latter was the relaxation of the transverse component of magnetization due to the dephasing caused by the spin-spin interactions. Bloch's theory gives an accurate description of liquid-state NMR. At the same time, it is too crude to describe solid-state NMR: in general, the spin-spin relaxation is a non-Markovian process, hence it can not be described in terms of a simple exponential decay.

The appearance of the first non-phenomenological theory addressing this problem can be attributed to the 1948 paper of Van Vleck [5], who suggested analyzing the moments of the absorption line:

$$M_n = \int_{-\infty}^{+\infty} du f(u) u^n. \quad (1.61)$$

The odd moments vanish due to the symmetry of $f(u)$, while the calculation of the even moments reduces to the evaluation of some infinite temperature equal-time correlators. In principle, it can be done in a closed form for a moment of any order. However, the resulting derivations quickly become very cumbersome due to the exponential scaling of the number of terms one has to deal with. In his paper, Van Vleck provided expressions for the second and the fourth moments. The analytical expressions for the sixth and the eighth moments were obtained much later by Jensen and Hansen [9] with the help of computers. It is worth noting that the expression for the eighth moment spans almost the whole page. Characterization of the absorption line in terms of the moments is equivalent to

the Taylor expansion of the time correlation function $C(t)$ in the vicinity of $t = 0$ (see Eq. (1.30)):

$$M_{2n} = (-1)^n \left(\frac{d^{2n}C(t)}{dt^{2n}} \right)_{t=0} / C(0). \quad (1.62)$$

Satisfactory determination of $C(t)$ for the intermediate times requires the knowledge of a large number of the expansion coefficients in the Taylor series. As their determination quickly becomes infeasible, the method of moments is not a very effective approach.

Another important milestone is the 1957 paper of Lowe and Norberg [6], where the authors showed the equivalence between the absorption peak line-shape in the frequency domain and the FID in the time domain and also proposed an expansion scheme for the calculation of the FID. The truncated dipole-dipole interaction given by Eq. (1.25) can be rewritten as the combination of Ising-type and Heisenberg-type terms:

$$\mathcal{H}'_{\text{dip}} = \sum_{i < j} \frac{\gamma^2(1 - 3 \cos^2 \theta_{ij})}{r_{ij}^3} \left[\frac{3}{2} S_i^z S_j^z - \frac{1}{2} \mathbf{S}_i \cdot \mathbf{S}_j \right]. \quad (1.63)$$

The approach of Lowe and Norberg was to construct a perturbation expansion of $e^{-i\mathcal{H}'_{\text{dip}}t}$ in terms of the Heisenberg-type terms with respect to the zeroth-order approximation involving only Ising-like terms. They carried this expansion up to the fourth order and found a reasonably good agreement with the results of their own experiment on CaF_2 , at least for the initial behaviour. However, the expansions of this kind in the powers of time are only valid for a limited initial region of time and tend to diverge for longer times. A satisfactory solution can only be reached if one finds a way to sum an infinite subsequence of the expansion series or to accurately approximate such sum.

An interesting line of works came from the application of the memory function formalism to the spin systems. In the context of this formalism, the correlation function of interest is presented as a solution to an integro-differential equation

$$\frac{dC(t)}{dt} = - \int_0^t d\tau F_1(t - \tau) C(\tau), \quad (1.64)$$

where $F_1(t)$ is the memory function. The idea here is to project out the degrees of freedom orthogonal to an observable of interest. The memory function $F_1(t)$ describes the dynamics of these degrees of freedom. The procedure is quite general and can be applied to the memory function $F_1(t)$ itself, leading to the infinite chain of integro-differential equations (see the works of Zwanzig [10] and Mori [11])

for more details):

$$\frac{dF_{n-1}(t)}{dt} = - \int_0^t d\tau F_n(t - \tau) F_{n-1}(\tau). \quad (1.65)$$

Laplace transform of equation 1.64 produces an algebraic equation of the form

$$\tilde{C}(z) = \frac{C(0)}{z + \tilde{F}_1(z)}. \quad (1.66)$$

Furthermore, Laplace transform can be applied to the memory functions of arbitrary order, leading to a representation of $\tilde{C}(z)$ as a continued fraction. Nevertheless, one should note that the calculation of a memory function is still a task no easier than the calculation of the auto-correlation function itself.

The applications to the spin systems required either the use of approximations for the memory function or the use of sophisticated fitting procedures in order to obtain the coefficients of the continued fraction. Tjon in the 1966 paper [12] approximated memory function by a Gaussian and found a reasonable agreement with experiment. However, he tested the approximation only for the case of CaF₂ and only for a short initial segment of time. This approach was later refined in the 1971 paper of Lado, Memory and Parker [13]. The authors used ideas similar to the general Zwanzig-Mori formalism. The scheme they developed allowed them to consider the corrections due to the deviations of the memory function from the Gaussian shape, which could be estimated from the knowledge of the moments of the experimental curve. This work was followed by the 1973 paper of Parker and Lado [14], where the method was applied to fit the FIDs in CaF₂. Regarding the use of continued fraction representations, I should also mention the 1975 work by Engelsberg and Chao [15] and the 1995 paper of Jensen [16]. Engelsberg and Chao employed a transformation of the continued fraction to another equivalent one, the coefficients of which were assumed to quickly converge to some limit. The fraction was effectively truncated by freezing all the coefficients starting from some level. The set of coefficients was obtained from the knowledge of the first four non-zero moments, however, the values of M_6 and M_8 were adjusted a bit to keep the spurious oscillations of the resulting curves at bay. The work of Jensen is, in some sense, the development of the work of Engelsberg and Chao. The author proposed to truncate the fraction at a level higher than the one determined by the first four known non-zero moments. In order to do that, a way to interpolate the value of the higher moment was suggested from the analysis of the approximate structure of the expressions from which the moments are determined. The results of truncation at two consequent levels were averaged, which allowed the author to overcome the problem of spurious oscillations encountered by Engelsberg and

Chao. The interpolation procedure was adjusted to fit the FID in CaF_2 , and the resulting scheme was applied to the calculation of the FID in ^{13}C -enriched diamond.

In 1967-1968, there was an interesting series of papers by Borckmans and Walgraef [17, 18, 19]. The authors derived kinetic equations for two-spin correlation functions with the use of resummation techniques developed by Prigogine and co-workers [20]. The results of their calculations were in a reasonable agreement with the experimental FID shape in CaF_2 . However, it should be noted that the procedure used by the authors was quite involved and the agreement thus obtained was, actually, not that good.

Another first-principle approach to the problem was presented in the 1976 paper of Becker, Plefka and Sauermann [21]. They truncated the hierarchy of equations of motion by decoupling the three-spin correlations in terms of the ones of the lower order. As a result, they obtained an integral equation of the form

$$C(t) = C_0(t) + \lambda \cdot \int_0^t \frac{dC_0(t')}{dt'} C(t-t') dt', \quad (1.67)$$

where $C_0(t)$ is the correlation function of the same observable as $C(t)$, but with dynamics determined only by the renormalized Ising-part of the truncated dipolar-dipolar Hamiltonian, and λ is the parameter controlling the renormalization. This paper was followed by the 1981 work of Sauermann and Wiegand [22], where the same integral equation was rederived by considering Mori frequency matrix (see [11]), and a slightly different value of the renormalization parameter λ was obtained. I should note, however, that the derivations of these papers were focused specifically on the FID in CaF_2 for the direction of the external magnetic field along [100] crystallographic axis. Hence, it is hard to argue what is the potential of the application of the approach to a broader class of problems.

An ideological continuation of this paper was the 1997 work of Fine [23]. The author obtained an integral equation, similar in structure to the one proposed by Becker, Plefka and Sauermann. However, the derivation used general physical arguments and treated the problem as kinetics in the spin phase space. The values of λ and $C_0(t)$ were determined by an ansatz facilitating interpolation between several exactly solvable cases in the space of Hamiltonian parameters. Another important feature is that the method was tested for a broad set of model systems [24] where the agreement was found to be consistently good qualitatively speaking. The quantitative agreement was not bad either, but it is something we hope to improve on.

Next in line is the approach proposed in 1976 by Lundin and Provotorov [25].

The idea was to consider the distribution of the local field produced by other spins on some particular site. The contribution to the local field was split into the correlated one coming from the nearest neighbours, and uncorrelated contribution from other spins. The distribution of the latter was assumed to be of the Gaussian form. This work was followed by the 1984 paper of Lundin and Makarenko [26] and by the 1992 paper of Lundin [27]. This idea of treating the outer shell of the system differently from the core is quite insightful and is something we build upon in this thesis. However, Lundin and coauthors completely neglected correlations between these two parts of the system, which hinders an accurate determination of the FID for intermediate and longer times.

An interesting approach I would like to mention is the one proposed in the 1996 paper of Lundin [28]. It is based on the following idea. The long-time asymptotic behaviour of the FID is determined by the singular point of its Laplace transform with the largest value of the real part. The parameters controlling the asymptotics are the real and imaginary parts of the singular point and the character of singularity (the order of the pole, for example). If we now look at the hierarchy of the equations of motion for the correlation functions of different orders, which is generated by repeatedly differentiating Eq. (1.56) with the help of Eq. (1.54), then the fact that the information about long-time behaviour is encoded in such a few parameters makes it plausible to suggest that all the correlation functions should be similar in this regime. Lundin used this idea to connect the third order correlation function with the FID, effectively truncating the whole hierarchy. The problem is, however, that the long-time form of this functional dependence was established from the analysis of the initial behaviour of correlation functions, i.e., two asymptotic expansions with non-overlapping regions of validity were compared, which puts in question the reliability of the results.

One drawback of the mentioned papers comes from the fact that, with a few exceptions, the majority of them were focused on the calculation of FID in CaF_2 . As a consequence, it is hard to assess which part of the success of the methods is general and which one comes from overfitting the CaF_2 FID data (this problem is also called overtraining in the context of machine learning). Another drawback is that the theories are quite elaborated and it is hard to quantify the uncertainties introduced by the approximations employed.

1.4.2 Numerical approaches

Since the analytical treatment of the problem is complicated, it is important also to look at the works that developed numerical modelling approach to the problem.

Classical Spins

One important bit of knowledge is that the dynamics of classical spins can often very well approximate dynamics of quantum spins. It is an expected situation in the case when the size of a quantum spin goes to infinity: this limit is equivalent to the limit $\hbar \rightarrow +\infty$. However, it can still be true even when we consider spins $1/2$. In 1966 Gade and Lowe [29] noticed that the theoretical FIDs obtained in the manner similar to the one used in the paper of Lowe and Norberg [6] are rather similar for the quantum spins of different length. In 1973, Jensen and Platz [30] used molecular dynamics simulations of classical spins to calculate the classical FID and compared their results with the results of Gade and Lowe. Finally, in 1976 Lundin and Zobov [25] gave a detailed analysis of both quantum and classical FIDs and analytically proved that they should coincide in either of the two limits: (i) the size of the quantum spins goes to infinity (ii) the effective number of interacting neighbours of a spin goes to infinity. Oddly enough, the classical simulations were not used that much during the following years. However, I should point out a 2015 paper of Elsayed and Fine [31], where the practical limits for the approximation of quantum dynamics by classical one were established. Still, there is a drawback of this approach, that is, it is hard to quantify the uncertainty induced by the approximation. In order to generate predictions, we need to supplement the classical simulations with another approach to compare to. Moreover, there are cases where the classical simulations are outright inaccurate so that they should be replaced by some other method. The Hybrid method described in this thesis can fulfill both of these roles.

Formally speaking, a classical spin lattice is defined by the Hamiltonian of the form (1.52) where the spin operators S_i^α are replaced by the spin vectors s_m^α :

$$H = \sum_{\alpha, m < n} J_{m,n}^\alpha s_m^\alpha s_n^\alpha, \quad (1.68)$$

The extended Poisson brackets for classical spins have the structure similar to that of the extended quantum commutation relations (1.53), namely:

$$\{s_m^\alpha, s_n^\beta\}_P = \delta_{mn} \cdot \varepsilon_{\alpha\beta\gamma} \cdot s_m^\gamma. \quad (1.69)$$

With their help, one can generate the equations of motion:

$$\dot{\mathbf{s}}_m = \{\mathbf{s}_m, H\}_P = \mathbf{s}_m \times \mathbf{h}_m^{CC} \quad (1.70)$$

where

$$\mathbf{h}_m^{CC} = - \sum_{n \neq m} \begin{pmatrix} J_{m,n}^x S_n^x \\ J_{m,n}^y S_n^y \\ J_{m,n}^z S_n^z \end{pmatrix} \quad (1.71)$$

are the classical local fields. The classical analogues of quantum correlation functions (1.56) are defined as

$$c_\alpha(t) = [M_\alpha(t)M_\alpha(0)]_{i.c.}, \quad M_\alpha = \sum_m S_m^\alpha, \quad (1.72)$$

where $[\dots]_{i.c.}$ denotes the average over ensemble of initial conditions. In the infinite-temperature limit, such an ensemble is characterised by the isotropic and independent distribution of the initial directions of the classical spins.

As Lundin and Zobov showed [25], the agreement between the FIDs of the classical spins and the quantum S -spins is observed when the length of classical spins is set to be $\sqrt{S(S+1)}$. Such a choice of the length guarantees that the characteristic time τ_c is the same for classical and quantum lattices. It also guarantees the equality of the second moments $M_2 \equiv -C''_\alpha(0)/C_\alpha(0) = -c''_\alpha(0)/c_\alpha(0)$ for the two lattices.

The parameter of the effective number of interacting neighbours, which controls the applicability of the classical simulations, is defined as

$$n_{\text{eff}} \equiv \frac{[\sum_n (J_{mn}^x{}^2 + J_{mn}^y{}^2 + J_{mn}^z{}^2)]^2}{\sum_n (J_{mn}^x{}^2 + J_{mn}^y{}^2 + J_{mn}^z{}^2)^2} \quad (1.73)$$

In practice, for quantum spins-1/2, the classical simulations are observed to perform well for the cases where n_{eff} is greater than four, as it was established by Elsayed and Fine [31].

Quantum typicality

Another important approach I would like to mention is the one based on the notion of quantum typicality [32, 33, 34, 35, 36]. The following discussion of this approach is based on the paper of Elsayed and Fine [37]

The trace operation is equivalent to the average over infinite-temperature distribution of normalized pure quantum states in the Hilbert space of the system [32]:

$$[\langle \psi | \mathcal{M}(t) \mathcal{M}(0) | \psi \rangle]_\psi = \frac{1}{D} \text{Tr} [\mathcal{M}(t) \mathcal{M}(0)], \quad (1.74)$$

where $[\dots]_\psi$ denotes the average over the wave-functions sampled from the distribution. However, when the dimension D of the Hilbert space is large, even a single

typical state serves as a good representative of the whole ensemble, which constitutes the essence of the notion of quantum typicality. This fact can be quantified in the following manner. Let us pick a random pure state $|\psi_{eq}\rangle$. Then

$$\langle \psi_{eq} | \mathcal{M}(t) \mathcal{M}(0) | \psi_{eq} \rangle = \frac{1}{D} \text{Tr} [\mathcal{M}(t) \mathcal{M}(0)] + \Delta(t), \quad (1.75)$$

where $\Delta(t)$ is a small correction. The value of Δ can be estimated by considering the variance of the average with respect to the ensemble of pure states. A detailed calculation (see Section 2.3 and [37]) shows, that the typical value of Δ is

$$\Delta(t) \sim \frac{1}{\sqrt{D}} \cdot \frac{\text{Tr} [\mathcal{M}(0) \mathcal{M}(0)]}{D}. \quad (1.76)$$

Since D grows exponentially, even for a system of 20 spins, the accuracy attained by considering only one typical state is already about 0.1%. As Elsayed and Fine pointed out [37], the calculation of quantum average can be then reduced to the solution of the Schrödinger equation

$$\frac{d}{dt} |\psi(t)\rangle = -i\mathcal{H} |\psi(t)\rangle. \quad (1.77)$$

for two wave-functions:

$$\langle \psi_{eq} | \mathcal{M}(t) \mathcal{M}(0) | \psi_{eq} \rangle = \langle \psi_{eq} | e^{i\mathcal{H}t} \mathcal{M} e^{-i\mathcal{H}t} \mathcal{M} | \psi_{eq} \rangle = \langle \psi_{eq}(t) | \mathcal{M} | \psi_{aux}(t) \rangle, \quad (1.78)$$

$$|\psi_{aux}(0)\rangle = \mathcal{M} |\psi_{eq}\rangle. \quad (1.79)$$

without the complete diagonalization of the Hamiltonian. In comparison with the latter, the direct integration allows one to treat larger fully quantum lattices numerically exactly, because it does not require one to store in the computer memory either density matrices or unitary transformations, which are dense $N \times N$ matrices. Instead, only the wave function vector and the sparse Hamiltonian matrix are stored.

The Schrödinger equation can be numerically integrated by standard schemes such as Runge-Kutta methods. There are also more efficient specialized schemes, such as the method utilizing decomposition of exponent in Chebyshev polynomials [38] or the methods based on the Suzuki-Trotter decomposition [39].

Although the use of the direct integration method brings substantial improvement in terms of the treatable system sizes, it is still hard to apply this method to the spin systems consisting of more than 36 spins (reaching of the system size of 36 spins was reported in paper [40]). At the same time, if one wants to calculate

the quantities corresponding to the thermodynamic limit, one should consider the lattice with the linear size of the order of 10 lattice sites so that it is possible to neglect the finite-size effects. (For the purely classical lattices, the finite size effects were attested in [31].) In the case of a three-dimensional lattice, the linear size of 10 lattice sites corresponds to 1000 spins in total, which surpasses the limitations of the direct integration method by orders of magnitude.

In conclusion, we should add that these notions of the distribution of pure states and of replacing the dynamics of operators with the dynamics of the wavefunctions are equally important as building blocks of the method described in the thesis. We discuss them and the resulting formalism more thoroughly in Chapter 2.

1.5 Main ideas of the thesis

The dimension of the Hilbert space scales exponentially with the number of spins, which is in stark contrast to the linear scaling of the phase space dimension for the corresponding classical spin system. In order to make a quantum spin system amenable to simulations, we need to reduce the number of degrees freedom. That is, we need to find such an approximation of the exact quantum dynamics, which operates within the state space of much lesser dimension, yet captures the important dynamical aspects of the full Hilbert space dynamics.

In the course of the work on this thesis, we have tested several approaches with the above goal in mind. The first one was based on the original idea of augmenting the classical spin dynamics: besides the classical degrees of freedom, the resulting dynamical system had additional degrees of freedom corresponding to the two-spin quantum correlations. We compared the simulations of augmented classical dynamics with the simulations of fully quantum one and found them to be coinciding for the extended initial interval of time. However, we also revealed a drawback of the method: the equations of motion for an augmented system were unstable. These results were published in the paper [41].

Nevertheless, in the end, we found a more fruitful approach, which this thesis is based on. Its ideas can be summarised as follows.

The direct numerical simulations are only possible for a small cluster inside a macroscopically large quantum system. We can think about the rest of the system as about an environment. While it is not feasible to simulate both the cluster and the environment quantum-mechanically, a plausible suggestion would be to approximate the dynamics of the environment instead. In doing so, it is crucial to preserve the dynamical correlations across the cluster-environment boundary as closely as possible. An important aspect of these correlations is the retarded action of each of spin on itself and other spins via interacting neighbours. In order

to preserve this aspect, it is crucial to treat both the cluster and the environment as the interacting parts of a single dynamical system⁷.

We considered two ways to approximate the environment: either by a collection of quantum clusters similar to the one we are concentrating on, or by a collection of classical spins. In order to facilitate the interactions between the quantum clusters in the former case and the interaction between the quantum cluster and the classical environment in the latter one, we introduced the classical effective magnetic fields produced by different parts of the system on each other.

In this thesis, we focus on the latter approach, because we found it to be more flexible and convenient. The resulting dynamical system is a hybrid quantum-classical lattice consisting of a quantum cluster surrounded by classical spins. These ingredients are at the core of the proposed Hybrid Method.

We should note that the approach based on approximating the environment by a collection of quantum clusters is somewhat similar to the Cluster Truncated Wigner Approximation method proposed by Wurtz, Polkovnikov and Sels [42, 43]. Their method, however, was never applied to the problem of FID calculation.

In order to determine the efficiency of the Hybrid Method, it is tested on various model one- and two-dimensional spin lattices. It is also applied to the calculation of the FID in several materials. The computed FIDs agree well with experiments.

1.6 Organization of the thesis

In Chapter 2 we provide a brief overview of the method of the Hilbert Space Average. With its help, we discuss some important properties of the infinite-temperature state of a spin lattice.

Chapter 3 contains the formal description of the Hybrid Method.

After that, we proceed in Chapter 4 with application of this method to the calculation of the spin relaxation for model one- and two-dimensional systems, where we compare the results of the hybrid simulations and the results of the classical simulations with the reference simulations of large quantum lattices obtained with the direct quantum method of paper [37] (see also Appendix A.1.1).

Calculations of FID in the real materials with the use of the Hybrid Method are presented in Chapter 5. We consider the cases of CaF_2 , ^{29}Si -enriched silicon and calcium fluorapatite.

⁷An alternative procedure for approximation would be to introduce the dynamical mean-field describing the effect of environment. Then the equations are closed by expressing the stochastic properties of the mean-field in terms of the dynamical correlations of the cluster. Such an approach, however, doesn't preserve the structure of the correlations across the cluster-environment border.

In Chapter 6, we provide a theoretical analysis of the hybrid dynamics introduced in Chapter 3.

The conclusions and outlook are presented in Chapter 7.

Appendix A provides the details of the simulations.

Appendix B is the manual to the code library written in the course of the project as an implementation of the Hybrid Method and companion methods.

Chapter 2

Properties of the infinite temperature ensemble

2.1 Distribution of wave functions in the Hilbert space

For the classical systems, there are two equivalent ways of describing the statistical properties. On one hand, one can focus on individual trajectories of the system, where the sampling of initial conditions is determined by the statistical ensemble. On the other hand, it is possible to describe the dynamics of the ensemble as a whole by means of the probability distribution of states in the phase space. In the former case, the evolution of trajectories is described by the Hamilton equations of motion. In the latter case, the dynamics of the distribution of states are dictated by the Liouville equation.

The statistical description of quantum systems usually employs the notion of density matrix which generalizes the notion of the probability distribution of states in the phase space. Correspondingly, the evolution of the density matrix is determined by the quantum generalization of the classical Liouville equation. At the same time, it is also possible to consider the quantum analogue of the individual trajectories approach. The difference with the classical case is that the states of the system — wave functions — are the elements of the Hilbert space, and their dynamics is determined by the Schrödinger equation. The initial conditions are then sampled from the distribution of wave functions. In the context of this approach, the quantum statistical averages are rewritten in the form

$$\text{Tr} [\rho \mathcal{A}] = [\langle \psi_\rho | \mathcal{A} | \psi_\rho \rangle]_{\psi_\rho}, \quad (2.1)$$

where \mathcal{A} is an observable, and $[\cdots]_{\psi_\rho}$ denotes the average with respect to the wave

functions $|\psi_\rho\rangle$ sampled from the distribution corresponding to the density matrix ρ ¹.

In the limit of infinite temperature, all states of a quantum system become equally probable. As a consequence, this limit is characterized by a uniform distribution of initial wave functions over a unit hyper-sphere $\langle\psi|\psi\rangle = 1$. The defining property of this distribution is its invariance under the action of the group of arbitrary unitary transformations $U(D)$ of the Hilbert space. Indeed, unitary transformations preserve the norms of wave-functions and the distances in the Hilbert space. From the former, it follows that the points of the unit hyper-sphere are transformed into each other. The latter implies that infinitesimal surface elements of the hyper-sphere are transformed into infinitesimal surface elements of the same area, thus the uniformity of distribution is also preserved.

In practice, the infinite-temperature distribution can be sampled in the following manner. First, we generate the wave functions as

$$|\psi\rangle = \sum_{k=1}^D a_k |k\rangle, \quad (2.2)$$

where $|k\rangle$ is a full orthonormal basis, $a_k \equiv r_k e^{i\varphi_k}$ are complex quantum amplitudes, in which φ_k are phases randomly sampled from interval $[0, 2\pi)$, and r_k are non-negative real numbers, whose squares $p_k \equiv r_k^2$ are sampled according to the probability distribution [44, 37]

$$P(p_k) = D \exp(-Dp_k). \quad (2.3)$$

Then, the wave functions $|\psi\rangle$ are normalized. Before the last step, the generated wave-functions have an arbitrary norm, yet their distribution is invariant with respect to arbitrary unitary transformations. The normalization puts all the wave functions onto the unit hyper-sphere while preserving this property of invariance.

The notion of distribution of wave functions allows us to study various statistical properties of quantum expectation values described by the correlators of the form

$$G_{\mathcal{A}_1, \mathcal{A}_2, \dots, \mathcal{A}_n}^{(n)} = [\langle\psi|\mathcal{A}_1|\psi\rangle \cdot \langle\psi|\mathcal{A}_2|\psi\rangle \cdot \dots \cdot \langle\psi|\mathcal{A}_n|\psi\rangle]_\psi, \quad (2.4)$$

where $\{\mathcal{A}_1, \mathcal{A}_2, \dots, \mathcal{A}_n\}$ is a set of observables. In this notation, quantum statistical averages correspond to the first order correlators (see Eq. (2.1)). Using

¹ The choice of the corresponding distribution is not unique. Nevertheless, since ρ is a positive semi-definite operator by definition, it is always possible to sample the wave functions ψ_ρ as $|\psi_\rho\rangle = \sqrt{D\rho}|\psi\rangle$, where $|\psi\rangle$ is sampled from the infinite temperature distribution. Indeed, as $[\langle\psi|\mathcal{A}|\psi\rangle]_\psi = \text{Tr}[\mathcal{A}]/D$ (see Eqs. (2.4), (2.5) and (2.11)), $[\langle\psi_\rho|\mathcal{A}|\psi_\rho\rangle]_{\psi_\rho} = \text{Tr}[\sqrt{\rho}\mathcal{A}\sqrt{\rho}] = \text{Tr}[\rho\mathcal{A}]$.

representation (2.2), we can reformulate Eq. (2.4) as

$$\begin{aligned} G_{\mathcal{A}_1, \mathcal{A}_2, \dots, \mathcal{A}_n}^{(n)} &= \\ &= \sum_{i_1, j_1} \sum_{i_2, j_2} \dots \sum_{i_n, j_n} [a_{i_1}^* a_{j_1} a_{i_2}^* a_{j_2} \dots a_{i_n}^* a_{j_n}]_{\psi} (\mathcal{A}_1)_{i_1, j_1} (\mathcal{A}_2)_{i_2, j_2} \dots (\mathcal{A}_n)_{i_n, j_n}, \end{aligned} \quad (2.5)$$

where

$$(\mathcal{A}_p)_{i_p, j_p} = \langle i_p | \mathcal{A}_p | j_p \rangle. \quad (2.6)$$

Given a particular choice of orthonormal basis in representation (2.2), the correlators for arbitrary sets of observables are completely determined by the matrix elements of observables and by the tensors

$$F_{j_1, j_2, \dots, j_n}^{i_1, i_2, \dots, i_n} \equiv [a_{i_1}^* a_{j_1} a_{i_2}^* a_{j_2} \dots a_{i_n}^* a_{j_n}]_{\psi}. \quad (2.7)$$

Since the distribution of wave functions describing infinite temperature is invariant with respect to unitary transformations, the choice of the orthonormal basis $|k\rangle$ in representation (2.2) is arbitrary. As a consequence, the form of the tensors $F_{j_1, j_2, \dots, j_n}^{i_1, i_2, \dots, i_n}$ is identical irrespective of this choice.

The ideas presented in this Section were developed in the work of Hams and De Raedt [32], the works of Fine [24, 45] and the works of Gemmer, Mahler and Michel [46, 33]. Although the forms of the lowest order tensors F_m^k and $F_{m,l}^{k,n}$ were already established in the literature, we find it instructive to provide an alternative derivation based on the symmetry arguments (see Section 2.2). Additionally, in Section 2.5, we derive the forms of the tensors of arbitrary order in the closed form, which can be regarded as a new result.

2.2 Infinite-temperature correlators of the first and the second orders

The discussion of the quantum typicality often revolves around two lowest-order tensors F_m^k and $F_{m,l}^{k,n}$.

$$F_m^k \equiv [a_k^* a_m]_{\psi}, \quad (2.8)$$

$$F_{m,l}^{k,n} \equiv [a_k^* a_m a_n^* a_l]_{\psi}. \quad (2.9)$$

Their form can be completely deduced from the symmetry arguments. The same arguments can be used to deduce the form of the tensors of arbitrary order. However, in this general case, it is more convenient to use a different approach described in Section 2.5.

As we have mentioned in Section 2.1, tensors F_m^k and $F_{m,l}^{k,n}$ transform into themselves under the action of the group $U(D)$. This group contains, among other members, independent rotations of complex phases of the basis vectors and the permutations of the basis vectors.

The invariance of F_m^k with respect to the phase rotations implies that only diagonal elements F_k^k are non-zero. The invariance with respect to the permutations additionally implies that this diagonal elements should all be equal to each other. These considerations constrain the form of the tensor to

$$F_m^k = \alpha \cdot \delta_m^k, \quad (2.10)$$

where α is a constant that can be found by computing the trace of F_m^k in two ways: from the definition (2.8), $\sum_k F_k^k = \left[\sum_k |a_k|^2 \right]_\psi = 1$, and from Eq. (2.10), $\sum_k F_k^k = D\alpha$. Thus $\alpha = 1/D$. As a result, Eqs. (2.8) and (2.10) give

$$[a_k^* a_m]_\psi = \frac{\delta_m^k}{D}. \quad (2.11)$$

Note that F_n^k is identical to the infinite temperature density matrix which proves our argument about the first order correlators being equivalent to the quantum statistical averages.

For the tensor $F_{m,l}^{k,n}$, the invariance with respect to the phase rotations leaves us with non-zero elements only of the form $F_{k,n}^{k,n}$ or $F_{n,k}^{k,n}$. The symmetry of $F_{m,l}^{k,n}$ with respect to the permutations of lower indices (or upper indices), further implies that $F_{k,n}^{k,n} = F_{n,k}^{k,n}$. In terms of averaging in Eq. (2.9), one should distinguish the elements $F_{k,n}^{k,n} = [|a_k|^2 |a_n|^2]_\psi$ with $k \neq n$ from the elements with $k = n$, i.e. of the type $F_{k,k}^{k,k} = [|a_k|^4]_\psi$. Given the symmetry with respect to the permutations of the basis vectors, the first subset is necessarily a part of the tensor that has form

$$F_{m,l}^{k,n} = \beta \cdot (\delta_m^k \delta_l^n + \delta_l^k \delta_m^n), \quad (2.12)$$

where β is a constant. We note here that tensor (2.12) is invariant with respect to all transformations belonging to the group $U(N)$ as required. It also yields the value $F_{k,k}^{k,k} = 2\beta = 2[|a_k|^2 |a_n|^2]_\psi$ for the elements from the second subset. If, however, $[|a_k|^4]_\psi \neq 2[|a_k|^2 |a_n|^2]_\psi$, this correction must be accounted for by adding to the right-hand-side of Eq. (2.12) a tensor of the form $\beta' \delta_m^k \delta_l^n \delta^{kn}$, where β' is another constant. However, a tensor defined in one basis as $\delta_m^k \delta_l^n \delta^{kn}$ does not remain invariant under all $U(N)$ transformations. Therefore, such a correction is not possible, which means that expression (2.12) represents the only possible

form of tensor $F_{m,l}^{k,n}$. The constant β can now be found by taking the “double trace” $\sum_k \sum_n F_{kn}^{k,n}$ in the definition (2.9), which gives $\sum_k \sum_n |a_k|^2 |a_n|^2 = 1$, and in Eq. (2.12), where it becomes $\beta D(D+1)$. Thus $\beta = \frac{1}{D(D+1)}$, which, together with Eqs. (2.12) and (2.9), implies

$$[a_k^* a_m a_n^* a_l]_\psi = \frac{\delta_m^k \delta_l^n + \delta_l^k \delta_n^m}{D(D+1)}. \quad (2.13)$$

2.3 Quantum typicality

Here we illustrate the notion of quantum typicality by proving Eq. 1.76. The following discussion parallels the derivation outlined by Elsayed and Fine [37].

Let us consider an observable \mathcal{B} with infinite temperature average $\langle \mathcal{B} \rangle \neq 0$:

$$\langle \mathcal{B} \rangle = [\langle \psi | \mathcal{B} | \psi \rangle]_\psi = \frac{\text{Tr} [\mathcal{B}]}{D}. \quad (2.14)$$

Here we have used Eq. (2.11).

If $|\psi_{eq}\rangle$ is some typical wave-function randomly sampled from the infinite-temperature distribution, then

$$\langle \psi_{eq} | \mathcal{B} | \psi_{eq} \rangle = \frac{\text{Tr} [\mathcal{B}]}{D} + \Delta. \quad (2.15)$$

Typical values of the deviation Δ are determined by the variance of the distribution of quantum expectation values:

$$\Delta^2 \simeq \left([\langle \psi | \mathcal{B} | \psi \rangle^2]_\psi - [\langle \psi | \mathcal{B} | \psi \rangle]_\psi^2 \right). \quad (2.16)$$

Using the definitions (2.4) and (2.5) with substituted Eqs. (2.11) and (2.13), we obtain

$$\begin{aligned} \left([\langle \psi | \mathcal{B} | \psi \rangle^2]_\psi - [\langle \psi | \mathcal{B} | \psi \rangle]_\psi^2 \right) &= \left(\frac{\text{Tr} [\mathcal{B}^2]}{D(D+1)} + \frac{\text{Tr}^2 [\mathcal{B}]}{D(D+1)} \right) - \left(\frac{\text{Tr} [\mathcal{B}]}{D} \right)^2 = \\ &= \frac{\text{Tr} [\mathcal{B}^2]}{D(D+1)} - \frac{\text{Tr}^2 [\mathcal{B}]}{D^2(D+1)}. \end{aligned} \quad (2.17)$$

As a consequence, for the relative deviation, we get

$$\left(\frac{\Delta}{\text{Tr} [\mathcal{B}]/D} \right)^2 = \frac{D}{(D+1)} \frac{\text{Tr} [\mathcal{B}^2]}{\text{Tr}^2 [\mathcal{B}]} - \frac{1}{D+1}. \quad (2.18)$$

Now, let us substitute into this equations $\mathcal{B} = \mathcal{M}_\alpha(t)\mathcal{M}_\alpha$. To estimate the deviation $\Delta(t) = \langle \psi_{eq} | \mathcal{M}_\alpha(t)\mathcal{M}_\alpha | \psi_{eq} \rangle - \text{Tr} [\mathcal{M}_\alpha(t)\mathcal{M}_\alpha]/D$, we can look at the case $t = 0$, where $\text{Tr} [\mathcal{M}_\alpha^2] = N \cdot \text{Tr} [(S_i^\alpha)^2] \sim D \ln D$ and $\text{Tr} [\mathcal{M}_\alpha^4] = N \cdot \text{Tr} [(S_i^\alpha)^4] \sim D \ln D$. Here we approximated the number of spins N as $N \sim \ln D$. Neglecting the subleading factor $\ln D$, we get for large D :

$$\frac{\Delta}{\text{Tr} [\mathcal{M}^2]/D} \sim \frac{1}{\sqrt{D}}. \quad (2.19)$$

2.4 Suppression of the expectation values of quantum operators by factor $1/\sqrt{D+1}$

Let us consider a cluster of N_Q spins $1/2$ with the dimension of the Hilbert space $D = 2^{N_Q}$. Let us further consider quantum operator \mathcal{A} , which has infinite-temperature average $\langle \mathcal{A} \rangle \equiv \frac{1}{D} \text{Tr} \mathcal{A} = 0$ and the variance $\langle \mathcal{A}^2 \rangle \equiv \frac{1}{D} \text{Tr} \mathcal{A}^2 \equiv \mathcal{A}_{\text{rms}}^2$. This can be the operator of local field, or the projection of an individual spin, or the operator of the total spin polarization. Here we show that the root-mean-squared value of $\langle \psi | \mathcal{A} | \psi \rangle$ is suppressed with respect to the normal quantum root-mean-squared value:

$$\sqrt{[\langle \psi | \mathcal{A} | \psi \rangle^2]_\psi} = \mathcal{A}_{\text{rms}}/\sqrt{D+1}. \quad (2.20)$$

Equivalently, it implies that for a typical wave function $|\psi_{eq}\rangle$ randomly sampled in the Hilbert space of the cluster from the infinite-temperature distribution,

$$\langle \psi_{eq} | \mathcal{A} | \psi_{eq} \rangle \sim \mathcal{A}_{\text{rms}}/\sqrt{D+1}. \quad (2.21)$$

This result is very important for the understanding of the Hybrid Method we introduce in Chapter 3.

The intuitive explanation of this fact is based on the notion of quantum parallelism [47]. Namely, the expectation value $\langle \psi | \mathcal{A} | \psi \rangle$ can be thought of as the average over D independent superimposed realizations of the state of the system, and, as a result, a factor of the order $1/\sqrt{D}$ suppresses the statistical fluctuations of $\langle \psi | \mathcal{A} | \psi \rangle$ with respect to the zero average.

In order to prove this result formally, we need to consider the following Hilbert-space averages:

$$[\langle \psi | \mathcal{A} | \psi \rangle]_\psi = \sum_{m,n} [a_m^* a_n]_\psi \mathcal{A}_{mn}, \quad (2.22)$$

and

$$[\langle \psi | \mathcal{A} | \psi \rangle^2]_\psi = \sum_{k,l,m,n} [a_k^* a_l a_m^* a_n]_\psi \mathcal{A}_{kl} \mathcal{A}_{mn}, \quad (2.23)$$

where \mathcal{A}_{mn} are the matrix elements of \mathcal{A} . Substituting Eqs. (2.11) and (2.13) into Eqs. (2.22) and (2.23), we obtain

$$[\langle \psi | \mathcal{A} | \psi \rangle]_{\psi} = \frac{\text{Tr} [\mathcal{A}]}{D} = 0, \quad (2.24)$$

and

$$[\langle \psi | \mathcal{A} | \psi \rangle^2]_{\psi} = \frac{\text{Tr} [\mathcal{A}^2]}{D(D+1)} + \frac{\text{Tr}^2 [\mathcal{A}]}{D(D+1)} = \frac{\mathcal{A}_{\text{rms}}^2}{D+1}, \quad (2.25)$$

which gives Eq. (2.20).

Now we apply the above general result to the operator of the local magnetic field of a quantum spin lattice

$$\mathbf{h}_i^{\text{QO}} = - \sum_{j \neq i} \begin{pmatrix} J_{ij}^x S_j^x \\ J_{ij}^y S_j^y \\ J_{ij}^z S_j^z \end{pmatrix}, \quad (2.26)$$

given by Eq. (1.55). The root-mean-squared value of \mathbf{h}_i^{QO} is defined as

$$h_{\text{rms}} \equiv \sqrt{\frac{1}{D} \sum_{j \neq i, \alpha} (J_{ij}^{\alpha 2} \text{Tr} [S_j^{\alpha 2}])}. \quad (2.27)$$

(The characteristic time of lattice dynamics τ_c given by Eq. (1.73) is obtained as $1/h_{\text{rms}}$.)

If we consider quantum expectation value $\langle \psi | \mathbf{h}_i | \psi \rangle$ for a random quantum state, then its root-mean-squared value is

$$\| \langle \psi | \mathbf{h}_i | \psi \rangle \|_{\text{rms}} = \sqrt{[\langle \psi | \mathbf{h}_i | \psi \rangle^2]_{\psi}} = \sqrt{\sum_{j \neq i, l \neq i, \alpha} J_{ij}^{\alpha} J_{il}^{\alpha} [S_j^{\alpha} S_l^{\alpha}]_{\psi}}. \quad (2.28)$$

Using Eqs.(2.24) and the fact that $[S_j^{\alpha} S_l^{\alpha}]_{\psi} = 0$ for $j \neq l$, we obtain:

$$\| \langle \psi | \mathbf{h}_i^{\text{QO}} | \psi \rangle \|_{\text{rms}} = \sqrt{\sum_{j \neq i, \alpha} J_{ij}^{\alpha 2} \frac{\text{Tr} [S_j^{\alpha 2}]}{D(D+1)}} = \frac{h_{\text{rms}}}{\sqrt{D+1}}. \quad (2.29)$$

2.5 Infinite-temperature correlators of arbitrary order

In order to deduce the form of the tensors $F_{j_1, j_2, \dots, j_n}^{i_1, i_2, \dots, i_n}$ of arbitrary order (see Eq. (2.7)), it is convenient to recast the Hilbert space average $[\dots]_{\psi}$ as a multidimensional

integral over the expansion coefficients c_i in representation (2.2):

$$\begin{aligned}
 F_{j_1, j_2, \dots, j_n}^{i_1, i_2, \dots, i_n} &\equiv [a_{i_1}^* a_{j_1} a_{i_2}^* a_{j_2} \dots a_{i_n}^* a_{j_n}]_{\psi} = \\
 &= \frac{\int \prod_{k=1}^D da_k^* da_k \delta \left(\sqrt{\sum_{k=1}^D a_k^* a_k} - 1 \right) a_{i_1}^* a_{j_1} a_{i_2}^* a_{j_2} \dots a_{i_n}^* a_{j_n}}{\int \prod_{k=1}^D da_k^* da_k \delta \left(\sqrt{\sum_{k=1}^D a_k^* c_k} - 1 \right)}, \quad (2.30)
 \end{aligned}$$

where $\delta(\dots)$ is the Dirac delta-function. Here the measure of integration $d\mu$ is defined in terms of the decomplexification of the Hilbert space:

$$d\mu = \prod_{i=1}^D da_i^* da_i = \prod_{p=1}^D d \operatorname{Re} a_i^* d \operatorname{Im} a_i. \quad (2.31)$$

The denominator of Eq. (2.30) is the area A_{2D-1} of the $(2D-1)$ -dimensional unit hypersphere.

In order to evaluate the right-hand side of Eq. (2.30), let us introduce an auxiliary multidimensional integral:

$$I_{j_1, j_2, \dots, j_n}^{i_1, i_2, \dots, i_n} = \int \prod_{k=1}^D \frac{da_k^* da_k}{\pi} e^{-\sum_{k=1}^D a_k^* a_k} a_{i_1}^* a_{j_1} a_{i_2}^* a_{j_2} \dots a_{i_n}^* a_{j_n}. \quad (2.32)$$

On the one hand, it is a simple Gaussian integral and can be evaluated in the closed form with the use of the Wick's theorem (see, for example, [48, Chapter 1]) as

$$I_{j_1, j_2, \dots, j_n}^{i_1, i_2, \dots, i_n} = \sum_P \delta_{i_1, Pj_1} \cdot \delta_{i_2, Pj_2} \cdot \dots \cdot \delta_{i_n, Pj_n}, \quad (2.33)$$

where the summation is performed over all the permutations P of n indices $\{j_1, j_2, \dots, j_n\}$. On the other hand, we can split the integration into the integration over the surface of the $(2D-1)$ -dimensional hyper-sphere of radius r with the subsequent integration over the radius of that hypersphere:

$$\begin{aligned}
 &\int \prod_{k=1}^D \frac{da_k^* da_k}{\pi} e^{-\sum_{k=1}^D a_k^* a_k} a_{i_1}^* a_{j_1} a_{i_2}^* a_{j_2} \dots a_{i_n}^* a_{j_n} = \\
 &= \int_0^{+\infty} dr r^{2D-1} \int \prod_{k=1}^D \frac{da_k^* da_k}{\pi} \delta \left(\sqrt{\sum_{k=1}^D a_k^* a_k} - r \right) e^{-\sum_{k=1}^D a_k^* a_k} a_{i_1}^* a_{j_1} a_{i_2}^* a_{j_2} \dots a_{i_n}^* a_{j_n} = \\
 &= [a_{i_1}^* a_{j_1} a_{i_2}^* a_{j_2} \dots a_{i_n}^* a_{j_n}]_{\psi} \cdot \frac{A_{2D-1}}{\pi^D} \int_0^{+\infty} dr e^{-r^2} r^{2(D+n)-1}. \quad (2.34)
 \end{aligned}$$

Here we have used the fact that

$$\begin{aligned}
 & \int \prod_{k=1}^D \frac{dc_k^* dc_k}{\pi} \delta \left(\sqrt{\sum_{k=1}^D a_k^* c_k} - r \right) e^{-\sum_{k=1}^D a_k^* c_k} a_{i_1}^* a_{j_1} a_{i_2}^* a_{j_2} \dots a_{i_n}^* a_{j_n} = \\
 & = e^{-r^2} \int \prod_{k=1}^D \frac{dc_k^* dc_k}{\pi} \delta \left(\sqrt{\sum_{k=1}^D a_k^* c_k} - r \right) a_{i_1}^* a_{j_1} a_{i_2}^* a_{j_2} \dots a_{i_n}^* a_{j_n} = \\
 & = e^{-r^2} r^n \int \prod_{k=1}^D \frac{dc_k^* dc_k}{\pi} \delta \left(\sqrt{\sum_{k=1}^D a_k^* c_k} - 1 \right) a_{i_1}^* a_{j_1} a_{i_2}^* a_{j_2} \dots a_{i_n}^* a_{j_n} = \\
 & = e^{-r^2} r^n A_{2D-1} [a_{i_1}^* a_{j_1} a_{i_2}^* a_{j_2} \dots a_{i_n}^* a_{j_n}]_{\psi}. \quad (2.35)
 \end{aligned}$$

In Eq. (2.34),

$$\begin{aligned}
 & \frac{A_{2D-1}}{\pi^D} \int_0^{+\infty} dr e^{-r^2} r^{2(D+n)-1} = \\
 & = \frac{A_{2D-1}}{\pi^D} \int_0^{+\infty} d(r^2/2) e^{-r^2} r^{2(D+n)-1} = \frac{\Gamma(D+n) A_{2D-1}}{2\pi^D}, \quad (2.36)
 \end{aligned}$$

where $\Gamma(x)$ is the Euler's gamma function, and

$$A_n \equiv \frac{2\pi^{\frac{n+1}{2}}}{\Gamma(\frac{n+1}{2})} \quad (2.37)$$

for odd n . Thus,

$$\frac{\Gamma(D+n) A_{2D-1}}{2\pi^D} = \frac{\Gamma(D+n)}{\Gamma(D)}. \quad (2.38)$$

Substituting Eq. (2.38) into Eq. (2.34) and comparing the result with Eq. (2.33), we, finally, get

$$F_{j_1, j_2, \dots, j_n}^{i_1, i_2, \dots, i_n} = \frac{\Gamma(D)}{\Gamma(D+n)} I_{j_1, j_2, \dots, j_n}^{i_1, i_2, \dots, i_n} = \frac{\Gamma(D)}{\Gamma(D+n)} \sum_P \delta_{i_1, Pj_1} \cdot \delta_{i_2, Pj_2} \cdot \dots \cdot \delta_{i_n, Pj_n}. \quad (2.39)$$

If we take $n = 1$ or $n = 2$, we indeed obtain Eqs. (2.11) and (2.13) respectively.

2.6 Symmetry of infinite-temperature correlation functions

2.6.1 The quantum case

The correlation functions of interest can be represented as linear combinations of two-spin correlation functions of the form

$$C_{i,j}^{\alpha,\beta}(t) = \langle S_i^\alpha(t) S_j^\beta(0) \rangle = \frac{1}{D} \text{Tr} \left[S_i^\alpha(t) S_j^\beta(0) \right]. \quad (2.40)$$

For example, the autocorrelation function of the total polarization in Eq. (1.56) is

$$C_\alpha(t) = \sum_{i,j} \langle S_i^\alpha(t) S_j^\beta(0) \rangle. \quad (2.41)$$

In Section 1.3, we showed that $C_\alpha(t)$ are even functions of time. This result, however, is much more general, and it is characteristic of the infinite-temperature state of the system. Here we show, that arbitrary two-spin correlation functions $C_{i,j}^{\alpha,\beta}(t)$ exhibit this property. Although this fact is well-known, the provided proof illustrates the application of the individual trajectories approach.

With the use of the notion of the distribution of wave functions in the Hilbert space (see Section 2.1 of this Chapter), we rewrite Eq. (2.40) as

$$C_{i,j}^{\alpha,\beta}(t) = (D + 1) \cdot \left[\langle \psi | S_i^\alpha(t) | \psi \rangle \langle \psi | S_j^\beta(0) | \psi \rangle \right]_\psi, \quad (2.42)$$

where we have used Eq. (2.13) combined with the fact that $\text{Tr} [S_i^\alpha(t)] = \text{Tr} [S_i^\alpha(0)] = 0$. The analysis of the behaviour of different dynamical quantities under the time-reversal is convenient to facilitate with the use of the operator of time-reversal Θ (for more details, see [49, Chapter 26]). In this regard, it is important to note that the distribution of wave-functions corresponding to the infinite-temperature state of the system is invariant not only under the action of arbitrary unitary transformations but also under the action of arbitrary anti-unitary transformations \tilde{U} . First of all, the points of unit hypersphere are still transformed into each other in this case. Indeed, for $|\tilde{\psi}\rangle = \tilde{U}|\psi\rangle$, where $\langle \psi | \psi \rangle = 1$, we have

$$\langle \tilde{\psi} | \tilde{\psi} \rangle = \langle \psi | \psi \rangle^* = 1. \quad (2.43)$$

Secondly, similar to unitary operators, anti-unitary operators transform infinitesimal surface elements of the unit hyper-sphere into infinitesimal surface elements with the same area, which implies that the uniformity of distribution over the

hyper-sphere is also preserved. In order to show it, we need to use the fact that any anti-unitary operator can be presented as the product of some unitary operator and the operator of the complex conjugation K . The unitary operators preserve the area of infinitesimal surface elements. The area-preserving property of the operator of complex conjugation K can be proven with the help of the decomplexification of the Hilbert space: in this representation, the action of K is equivalent to the inversion of some of the coordinates.

Additionally, we need the identity describing the transformation of observables under the action of time-reversal:

$$\langle \alpha | \mathcal{A} | \beta \rangle = \langle \Theta \beta | \Theta \mathcal{A}^\dagger \Theta^{-1} | \Theta \alpha \rangle. \quad (2.44)$$

(This identity is, actually, true not only for Θ but also for any anti-unitary operator. For the proof, see [50, pp. 273–274].) With the help of this identity, we can write in Eq. (2.42)

$$\begin{aligned} \left[\langle \psi | S_i^\alpha(t) | \psi \rangle \langle \psi | S_j^\beta(0) | \psi \rangle \right]_\psi &= \\ &= \left[\langle \Theta \psi | \Theta S_i^\alpha(t) \Theta^{-1} | \Theta \psi \rangle \langle \Theta \psi | \Theta S_j^\beta(0) \Theta^{-1} | \Theta \psi \rangle \right]_\psi. \end{aligned} \quad (2.45)$$

Since the infinite-temperature distribution is invariant under the action of anti-unitary operator of time-reversal Θ , we can manipulate this expression further:

$$\begin{aligned} \left[\langle \Theta \psi | \Theta S_i^\alpha(t) \Theta^{-1} | \Theta \psi \rangle \langle \Theta \psi | \Theta S_j^\beta(0) \Theta^{-1} | \Theta \psi \rangle \right]_\psi &= \\ &= \left[\langle \psi | \Theta S_i^\alpha(t) \Theta^{-1} | \psi \rangle \langle \psi | \Theta S_j^\beta(0) \Theta^{-1} | \psi \rangle \right]_\psi, \end{aligned} \quad (2.46)$$

where

$$\Theta S_i^\alpha(t) \Theta^{-1} = \Theta e^{i\mathcal{H}t} S_i^\alpha e^{-i\mathcal{H}t} \Theta^{-1} = \Theta e^{i\mathcal{H}t} \Theta^{-1} \Theta S_i^\alpha \Theta^{-1} \Theta e^{-i\mathcal{H}t} \Theta^{-1}. \quad (2.47)$$

Time reversal changes the signs of spin operators: $\Theta S_i^\alpha \Theta^{-1} = -S_i^\alpha$. The Hamiltonian defined by Eq. (1.52) is invariant under the time-reversal because it consists only of two-spin terms, i.e. $\Theta \mathcal{H} \Theta^{-1} = \mathcal{H}$. At the same time, the application of time-reversal to the unitary operator of evolution changes the sign of imaginary unity i : $\Theta e^{-i\mathcal{H}t} \Theta^{-1} = e^{i\mathcal{H}t}$. Combining all these facts together, we, finally, get

$$\begin{aligned} C_{i,j}^{\alpha,\beta}(t) &= (D+1) \cdot \left[\langle \psi | S_i^\alpha(t) | \psi \rangle \langle \psi | S_j^\beta(0) | \psi \rangle \right]_\psi = \\ &= (D+1) \cdot \left[\langle \psi | S_i^\alpha(-t) | \psi \rangle \langle \psi | S_j^\beta(0) | \psi \rangle \right]_\psi = C_{i,j}^{\alpha,\beta}(-t). \end{aligned} \quad (2.48)$$

2.6.2 The classical case

As in the quantum case, the symmetry with respect to time-reversal is exhibited by the infinite temperature correlation functions in the classical case.

The classical analogues of the two-spin correlation functions (2.40) are defined similarly to the auto-correlation functions (1.72):

$$c_{m,n}^{\alpha,\beta}(t) = [s_m^\alpha(t)s_n^\beta(0)]_{i.c.}. \quad (2.49)$$

The time reversal of classical spin dynamics corresponds to the change in the signs of all the spin vectors. The classical Hamiltonian (1.68) is invariant under this operation. Therefore, if $\{s_m^\alpha(t)\}$ is a solution of the classical equations of motion (1.70), (1.71), then $\{-s_m^\alpha(-t)\}$ is also a solution. One can check this fact by the simple substitution into Eqs. (1.70) and (1.71). For the following derivation, it is convenient to write the average over initial conditions $s_m^\alpha(0) = x_m^\alpha$ explicitly as

$$[s_m^\alpha(t)s_n^\beta(0)]_{i.c.} = \left[(s_m^\alpha(t))|_{s_m^\alpha(0)=x_m^\alpha} (s_n^\beta(0))|_{s_m^\alpha(0)=x_m^\alpha} \right]_{x_m^\alpha}. \quad (2.50)$$

Time-reversal symmetry implies that

$$(s_m^\alpha(t))|_{s_m^\alpha(0)=x_m^\alpha} = (-s_m^\alpha(-t))|_{s_m^\alpha(0)=-x_m^\alpha}. \quad (2.51)$$

As a consequence,

$$\begin{aligned} & \left[(s_m^\alpha(t))|_{s_m^\alpha(0)=x_m^\alpha} (s_n^\beta(0))|_{s_m^\alpha(0)=x_m^\alpha} \right]_{x_m^\alpha} = \\ & = \left[(-s_m^\alpha(-t))|_{s_m^\alpha(0)=-x_m^\alpha} (-s_n^\beta(0))|_{s_m^\alpha(0)=-x_m^\alpha} \right]_{x_m^\alpha}. \end{aligned} \quad (2.52)$$

The infinite-temperature state is characterized by the isotropic and independent distribution of each of the initial spin vectors. Such a distribution is invariant with respect to the reversal of the directions of the spins, thus

$$\begin{aligned} & \left[(-s_m^\alpha(-t))|_{s_m^\alpha(0)=-x_m^\alpha} (-s_n^\beta(0))|_{s_m^\alpha(0)=-x_m^\alpha} \right]_{x_m^\alpha} = \\ & = \left[(s_m^\alpha(-t))|_{s_m^\alpha(0)=x_m^\alpha} (s_n^\beta(0))|_{s_m^\alpha(0)=x_m^\alpha} \right]_{x_m^\alpha} = [s_m^\alpha(-t)s_n^\beta(0)]_{i.c.}. \end{aligned} \quad (2.53)$$

Finally, we get

$$c_{m,n}^{\alpha,\beta}(t) = [s_m^\alpha(t)s_n^\beta(0)]_{i.c.} = [s_m^\alpha(-t)s_n^\beta(0)]_{i.c.} = c_{m,n}^{\alpha,\beta}(-t). \quad (2.54)$$

Chapter 3

The Hybrid Method

In this chapter, we introduce a method of approximating the dynamics of a quantum lattice by the dynamics of a hybrid quantum-classical lattice. We call it succinctly the Hybrid Method. The theoretical analysis of the hybrid dynamics itself is postponed until Chapter 6.

3.1 Hybrid lattice and its equations of motion

We approximate the fully quantum lattice (see Eq. 1.52) by a hybrid lattice that contains a set of lattice sites \mathcal{Q} occupied by a cluster of quantum spins $1/2$ and a much larger set of sites \mathcal{C} occupied by classical spins (see Fig. 3.1). The quantum cluster is described by a wave function $|\psi\rangle$, while the classical spins are described by a set of vectors $\{\mathbf{s}_m\}$.

The challenge in defining the dynamics of such a hybrid system is to reproduce the dynamical correlations of the original fully quantum lattice as closely as possible. An important aspect of these correlations is the retarded action of each spin on itself and remote spins via interacting neighbours. In order to induce such correlations across the quantum-classical border, we introduce effective local fields exerted by the quantum and the classical parts on each other. The local fields exerted by the classical environment on quantum spins are to have the standard form (1.71) used in purely classical simulations. In order to define the reverse action of the quantum spins on the classical neighbors, one can try to take the expression (1.55) for the operator of quantum local field and, in that expression, replace quantum spin operators with their expectation values $\langle\psi|S_m^\alpha|\psi\rangle$. However, the problem with such an approach is that, for a typical pure state describing a cluster of $N_{\mathcal{Q}}$ spins $1/2$, the expectation values $\langle\psi|S_m^\alpha|\psi\rangle$ are exponentially small [33, 47, 37] — they are suppressed by factor $1/\sqrt{D_{\mathcal{Q}}+1}$, where $D_{\mathcal{Q}} = 2^{N_{\mathcal{Q}}}$ is cluster's Hilbert space dimension (see Section 2.4 for the derivation). Therefore, for

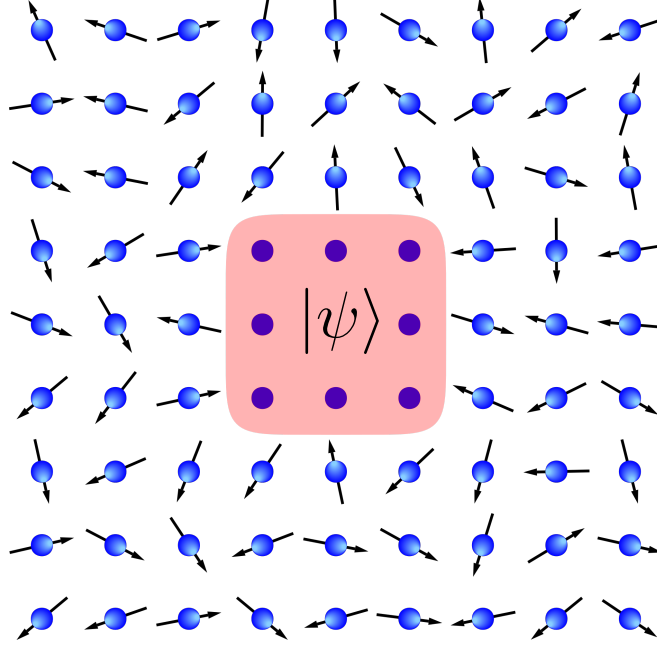


Figure 3.1: Sketch of a hybrid lattice: a cluster of spins 1/2 surrounded by an environment of classical spins. The quantum cluster is described by a wave function $|\psi\rangle$. Classical spins are represented by three-dimensional vectors.

$D_Q \gg 1$, such a naive approach would lead to a negligible action of quantum spins on the classical ones, thereby failing to induce qualitatively important correlations across the quantum-classical border. Instead, we propose to use the quantum expectation values scaled up by factor $\sqrt{D_Q + 1}$, whenever they are coupled to or combined with the classical variables.

We describe the dynamics of the quantum and the classical parts are by respective Hamiltonians

$$\mathcal{H}_Q = \sum_{\substack{i,j \in Q \\ i < j, \alpha}} J_{i,j}^\alpha S_i^\alpha S_j^\alpha - \sum_{i \in Q} \mathbf{h}_i^{CQ} \cdot \mathbf{S}_i, \quad (3.1)$$

$$H_C = \sum_{\substack{m,n \in C \\ m < n, \alpha}} J_{m,n}^\alpha s_m^\alpha s_n^\alpha - \sum_{m \in C} \mathbf{h}_m^{QC} \cdot \mathbf{s}_m, \quad (3.2)$$

where S_i^α are the operators of spins 1/2 as in Eq. (1.52), $\mathbf{s}_m \equiv (s_m^x, s_m^y, s_m^z)$ are vectors of length $\sqrt{S(S+1)} = \sqrt{3}/2$ representing classical spins, \mathbf{h}_i^{CQ} and \mathbf{h}_i^{QC}

are the local fields coupling the quantum and the classical parts:

$$\mathbf{h}_i^{CQ} = - \sum_{n \in \mathcal{C}} \begin{pmatrix} J_{i,n}^x s_n^x \\ J_{i,n}^y s_n^y \\ J_{i,n}^z s_n^z \end{pmatrix}, \quad (3.3)$$

$$\mathbf{h}_m^{QC} = -\sqrt{D_Q + 1} \cdot \sum_{j \in \mathcal{Q}} \begin{pmatrix} J_{m,j}^x \langle \psi | S_j^x | \psi \rangle \\ J_{m,j}^y \langle \psi | S_j^y | \psi \rangle \\ J_{m,j}^z \langle \psi | S_j^z | \psi \rangle \end{pmatrix}. \quad (3.4)$$

The entire hybrid lattice is assumed to have periodic boundary conditions.

If we choose the Heisenberg representation to describe the state of the quantum cluster, the equations of motion are generated with the help of the commutation relations (1.53) and poisson brackets (1.69) for the quantum and the classical parts of the system respectively:

$$\dot{\mathbf{S}}_i = -i [\mathbf{S}_i, \mathcal{H}_Q] = \mathbf{S}_i \times (\mathbf{h}_i^{QC} + \mathbf{h}_i^{CQ}), \quad (3.5)$$

$$\dot{\mathbf{s}}_m = \{\mathbf{s}_m, H_C\}_P = \mathbf{s}_m \times (\mathbf{h}_m^{CC} + \mathbf{h}_m^{QC}), \quad (3.6)$$

where

$$\mathbf{h}_m^{QC} = - \sum_{\substack{j \in \mathcal{Q} \\ j \neq i}} \begin{pmatrix} J_{i,j}^x S_j^x \\ J_{i,j}^y S_j^y \\ J_{i,j}^z S_j^z \end{pmatrix}, \quad (3.7)$$

and

$$\mathbf{h}_m^{CC} = - \sum_{\substack{n \in \mathcal{C} \\ n \neq m}} \begin{pmatrix} J_{m,n}^x s_n^x \\ J_{m,n}^y s_n^y \\ J_{m,n}^z s_n^z \end{pmatrix}. \quad (3.8)$$

Such form of the equations of motion is convenient for the analysis. For the calculations, however, it is better to work with the Schrödinger representation. In this case the evolution of the wave function of the quantum cluster is determined by the Schrödinger equation:

$$\frac{d|\psi(t)\rangle}{dt} = -i\mathcal{H}_Q|\psi\rangle. \quad (3.9)$$

The complete dynamics of the system is thus defined by the system of Eqs. (3.9) and (3.6), which should be integrated jointly.

The infinite-temperature distribution of the initial conditions for the hybrid lattice is naturally defined as the product of the infinite-temperature distributions for each of the subsystems. Thus, the initial conditions for the simulations include a fully random choice of normalized $|\psi(0)\rangle$ in the Hilbert space of the quantum

cluster and fully random orientations of classical spins.

The hybrid version of the total spin polarization $\mathfrak{M}_\alpha(t)$ is defined according to the earlier prescription for rescaling quantum expectation values:

$$\mathfrak{M}_\alpha(t) = \sqrt{D_{\mathcal{Q}} + 1} \cdot \langle \psi(t) | \sum_{i \in \mathcal{Q}} S_i^\alpha | \psi(t) \rangle + \sum_{m \in \mathcal{C}} s_m^\alpha(t). \quad (3.10)$$

The rescaling by factor $\sqrt{D_{\mathcal{Q}} + 1}$ is central to the Hybrid method. It will be further discussed and justified in Section 3.2 (see also Chapter 6).

3.2 Correlation functions

For purely classical systems, equilibrium auto-correlation functions $c_\alpha(t)$ are extracted from the equilibrium noise of the quantity of interest $M_\alpha(t) = \sum_m s_m^\alpha(t)$ using the definition (1.72) (we repeat it here for the convenience of the reader):

$$c_\alpha(t) = [M_\alpha(t)M_\alpha]_{i.c.}, \quad (3.11)$$

As we demonstrated in Section 2.6.1, for purely quantum system, it is possible to re-express the auto-correlation function (1.56) in the similar form:

$$C_\alpha(t) = (D + 1) \cdot [\langle \psi | \mathcal{M}_\alpha(t) | \psi \rangle \langle \psi | \mathcal{M}_\alpha(0) | \psi \rangle]_\psi. \quad (3.12)$$

Here, the amplitude of the quantum noise $\langle \psi | \mathcal{M}_\alpha(t) | \psi \rangle$ is smaller than its classical counterpart $M_\alpha(t)$ by $1/\sqrt{D + 1}$, which results in the appearance of compensating factor $(D + 1)$ in Eq. (3.12).

Since the hybrid lattice contains classical spins, it is possible to define the hybrid correlation functions $\mathfrak{C}_\alpha(t)$ by analogy with Eqs. (3.12) and (3.11) as

$$\mathfrak{C}_\alpha(t) = [\mathfrak{M}_\alpha(t)\mathfrak{M}_\alpha(0)]_\psi, \quad (3.13)$$

where $\mathfrak{M}_\alpha(t)$ is given by Eq. (3.10). At the level of a basic idea, the rescaling introduced in Eq. (3.10) compensates the amplitude mismatch between the quantum and the classical contributions to $\mathfrak{M}_\alpha(t)$.

Such a straightforward definition of $\mathfrak{C}_\alpha(t)$ is, however, plagued by the fact that the dominant contribution to $\mathfrak{C}_\alpha(t)$ comes from the correlations between the spins of the classical part of the system. A way to overcome this problem is to remember that the original quantum lattice is translationally invariant so that the correlation functions $C_\alpha(t)$ can be re-expressed in the form (1.60). Equivalently, we can write

Eq. (1.60) with the help of Eq. (2.42) as

$$C_\alpha(t) = (D+1) \frac{N}{N_{\mathcal{Q}'}} [\langle \psi | \mathcal{M}'_\alpha(t) | \psi \rangle \langle \psi | \mathcal{M}_\alpha(0) | \psi \rangle]_\psi, \quad \mathcal{M}'_\alpha = \sum_{i \in \mathcal{Q}'} S_i^\alpha, \quad (3.14)$$

where \mathcal{Q}' is the subset of the lattice sites (containing arbitrary spins in the case where all the spins equivalent or containing arbitrary basis cells otherwise; see the discussion preceding Eq. (2.42)). The separation of the system into a quantum cluster and a classical environment breaks the translational invariance of the hybrid lattice. As a consequence, it is natural to define the hybrid correlation functions by analogy to Eq. (3.14). The presence of the quantum-classical border in the hybrid simulations makes different choices of \mathcal{Q}' nonequivalent from the viewpoint of the approximation error. We minimize this error, by choosing the subset \mathcal{Q}' to consist of one or several equivalent spins inside the quantum cluster which are furthestmost from the quantum-classical border.

We can combine these arguments into the following definition of the hybrid correlation function:

$$\mathfrak{C}_\alpha(t) \equiv \frac{N}{N_{\mathcal{Q}'}} \cdot [\mathfrak{M}'_\alpha(t) \mathfrak{M}_\alpha(0)]_{i.c.}, \quad (3.15)$$

where $\mathfrak{M}_\alpha(t)$ is given by Eq. (3.10), and $\mathfrak{M}'_\alpha = \sqrt{D_{\mathcal{Q}}+1} \cdot \langle \psi(t) | \sum_{j \in \mathcal{Q}'} S_j^\alpha | \psi(t) \rangle$. Note, that this way $\mathfrak{C}_\alpha(t)$ is determined by the dynamics of the central spins of the cluster, which are the least influenced by the presence of the quantum-classical border.

Hybrid auto-correlation functions (3.15) are based on the definition (3.12) of the quantum correlation function. In comparison with the equivalent definition (1.74), the averaging procedure in the definition (3.12) is much less efficient (see Appendix A.2 for a more detailed discussion). It would be beneficial to define the hybrid correlation functions similarly to Eq. (3.12). However, we were unable to combine Eq. (3.12) with the classical dynamics. In the end, the hybrid method requires many samples of initial conditions for the calculation of correlation function as opposed to the single random wave-function in the case of the method based on quantum typicality. At the same time, this disadvantage is outweighed by the possibility to consider much larger lattice sizes.

3.3 Uncertainty estimate

In the limit where the quantum cluster occupies the whole lattice, the hybrid calculation must converge to the exact quantum result. On the other hand, the hybrid scheme for a one-spin quantum cluster behaves like a purely classical lattice.

In this case, we can use the expectation values of the spin projection operators to form a closed system of equations of motion. The factor $\sqrt{D_Q + 1}$ guarantees then that the length of the resulting classical vector of quantum expectation values is the same as the lengths of the classical spins. Thus, as the size of the quantum cluster increases, the hybrid dynamics “interpolates” between the purely classical dynamics and the exact quantum dynamics. It is plausible that such an interpolation occurs smoothly with the size of the quantum cluster.

We can utilize the fact that the hybrid calculations converge to the exact quantum result with increasing quantum cluster size to make an efficient estimate of the accuracy of Hybrid Method’s predictions. A discrepancy between the results for quantum clusters of significantly different sizes gives an estimate of the difference with the thermodynamic limit¹. The implementation of the hybrid method can realistically involve only relatively small quantum clusters of 10-20 spins 1/2. Yet, precisely for this reason, the relative differences between these sizes are large. Therefore, if these differences do not lead to large deviations of the computed correlation functions, then the result should be viewed as reliable. For the lattices with a not too small number of interacting neighbours, where purely classical calculations are expected to work well [31], the deviation between a purely classical calculation and a hybrid calculation with a small quantum cluster can already be sufficient for a reasonable estimate of the predictive accuracy.

Overall, we are unable to provide justifications for the method and the uncertainty estimate which are completely rigorous from the mathematical point of view. However, from the practical point of view, such a justification can be provided in the form of extensive testing on a broad variety of systems. It is precisely what is done in the following two Chapters.

¹This discrepancy gives an estimate of the difference with the exact quantum result. Given the full lattice size is sufficiently large, this exact quantum result closely reproduces the thermodynamic limit.

Chapter 4

Application of the Hybrid Method to the simulation of model one- and two-dimensional spin lattices

In the following two chapters we do not distinguish between $C_\alpha(t)$, $c_\alpha(t)$ and $\mathfrak{C}(t)$ defined by Eqs. (1.56), (1.72) and (3.15). Additionally, all the plots present normalized correlation functions $C_\alpha(t)/C_\alpha(0)$.

4.1 One- and two-dimensional model lattices

Our tests of the performance of the hybrid method for one-dimensional chains and two-dimensional square lattices of spins 1/2 are presented in Figs. 4.1, 4.3 and 4.4, 4.6, 4.7, respectively. The lattices had nearest-neighbour interactions with coupling constants indicated in the figure legends. In all the figures, the predictions of the hybrid method are compared with the results of numerically exact direct quantum simulations for sufficiently large clusters (see Appendix A.1.1). The cluster was considered “sufficiently large”, when, in the time range of interest, the change of $C_\alpha(t)$ with the increase of the cluster size was negligible. The sizes of the quantum clusters for hybrid simulations were, typically, smaller: in comparison with direct simulations, they were limited by the requirement to generate many more and much longer quantum evolutions in order to collect enough statistics (see Appendix A.3). Figures 4.1, 4.3, 4.4, 4.6 and 4.7 also include back-to-back comparison of hybrid simulations with purely classical simulations.

In Figs. 4.2 and 4.5, we present the dependence of the results of direct quantum simulations of large quantum clusters on the size of the clusters for the cases considered in Figs. 4.1 and 4.4. The corresponding data for the cases considered in Figs. 4.3, 4.6 and 4.7 is already included in these figures. With the exception

of Figs. 4.6(a,a') and 4.7(b,b'), these tests reveal that the correlation functions obtained for several cluster sizes coincide with good accuracy, which, in turn, indicates that the respective plots represent the correlation functions of interest in the thermodynamic (infinite-cluster) limit.

For one-dimensional chains, the performance of the hybrid simulations in Figs. 4.1(a,b) and 4.3(a,b) is excellent. These figures correspond to typical situations when correlation functions $C_\alpha(t)$ decay not too slowly, i.e on the timescale of the order of τ_c given by Eq. (1.57). On the contrary, Fig. 4.1(c) illustrates an atypical case, where the coupling constants and the axis α are chosen such that $C_\alpha(t)$ decays anomalously slowly. In this case, the hybrid method's prediction exhibits a clear discrepancy from the reference plot. Important, however, is the fact, also illustrated in Fig. 4.1(c), that the internal estimate of the predictive accuracy based on the use of different quantum clusters within the hybrid method would anticipate the above discrepancy. We note here that the same accuracy estimate in Figs. 4.1(a,b) and 4.3(a,b) is consistent with the observed excellent agreement with the reference plots. We further observe that, in all cases presented in Figs. 4.1 and 4.3, the performance of the hybrid simulations is significantly better than that of the classical ones.

Figures 4.4, 4.6 and 4.7 illustrate that, for two-dimensional lattices, hybrid simulations generally exhibit a very good performance, which is also noticeably better than that of the classical simulations. At the same time, there is a problematic case presented in Figs. 4.6(a,a'), where the classical simulations seem to perform better than the hybrid simulations. We should point out, however, that the reference curve corresponding to the direct quantum simulations of 5×5 quantum cluster is not reliable in this case, because the comparison of the direct quantum simulations of a large quantum cluster for different sizes of the cluster does not provide evidence that the results of these simulations converged to the thermodynamic limit.

4.2 Discussion

Overall, Figs. 4.1, 4.3, 4.4, 4.6 and 4.7 illustrate that the hybrid method produces mostly very accurate predictions. As we now explain, the rare situations where method's predictive accuracy is limited can be understood from the analysis of the asymptotic long-time behaviour of $C_\alpha(t)$.

There exists substantial experimental [52, 53, 54, 55] and numerical [56, 57, 37, 31] evidence, also supported by theoretical arguments [18, 45, 58], that, despite widely varying shapes of correlation functions $C_\alpha(t)$, their long-time behaviour in

non-integrable systems has universal form

$$C_\alpha(t) \cong e^{-\gamma t} \quad \text{or} \quad C_\alpha(t) \cong e^{-\gamma t} \cos(\omega t + \phi), \quad (4.1)$$

where γ and ω are constants of the order of $1/\tau_c$, where τ_c is given by Eq. 1.57. The asymptotic behaviour (4.1) represents the slowest-decaying relaxational mode of the system [45]. Typically, it becomes dominant after a time of the order of several τ_c . Therefore, if one manages to accurately compute $C_\alpha(t)$ over the above initial time interval, then a good overall accuracy is assured. This is what the hybrid method achieves in a typical setting. (When we mention the long-time limit, we refer to the times which are still much smaller than T_1 .)

On the basis of the above consideration, one can anticipate that the hybrid method would predict the asymptotic time constants γ and ω with *absolute* uncertainty ϵ/τ_c , where ϵ is a number significantly smaller than 1. Yet, such an uncertainty may lead to noticeable discrepancies in two problematic cases [45]: In the first of them, the slowest relaxational mode is characterized by $\gamma \ll 1/\tau_c$, and hence the *relative* uncertainty of predicting γ may be large [cf. Fig. 4.1(c)]. In the second problematic case, the asymptotic behaviour is characterized by an accidental competition between two slowest relaxation modes with exponential decay constants γ_1 and γ_2 such that $|\gamma_2 - \gamma_1| \ll 1/\tau_c$. As a result, the long-time behaviour can be significantly distorted in an approximate calculation. This latter case is illustrated in Figs. 4.6(a) and 4.7(b,d), where we find that the competition between different kinds of asymptotic behaviour is accompanied by larger finite-size effects for the reference plots, which, in turn, makes the tests of the hybrid method not fully conclusive.

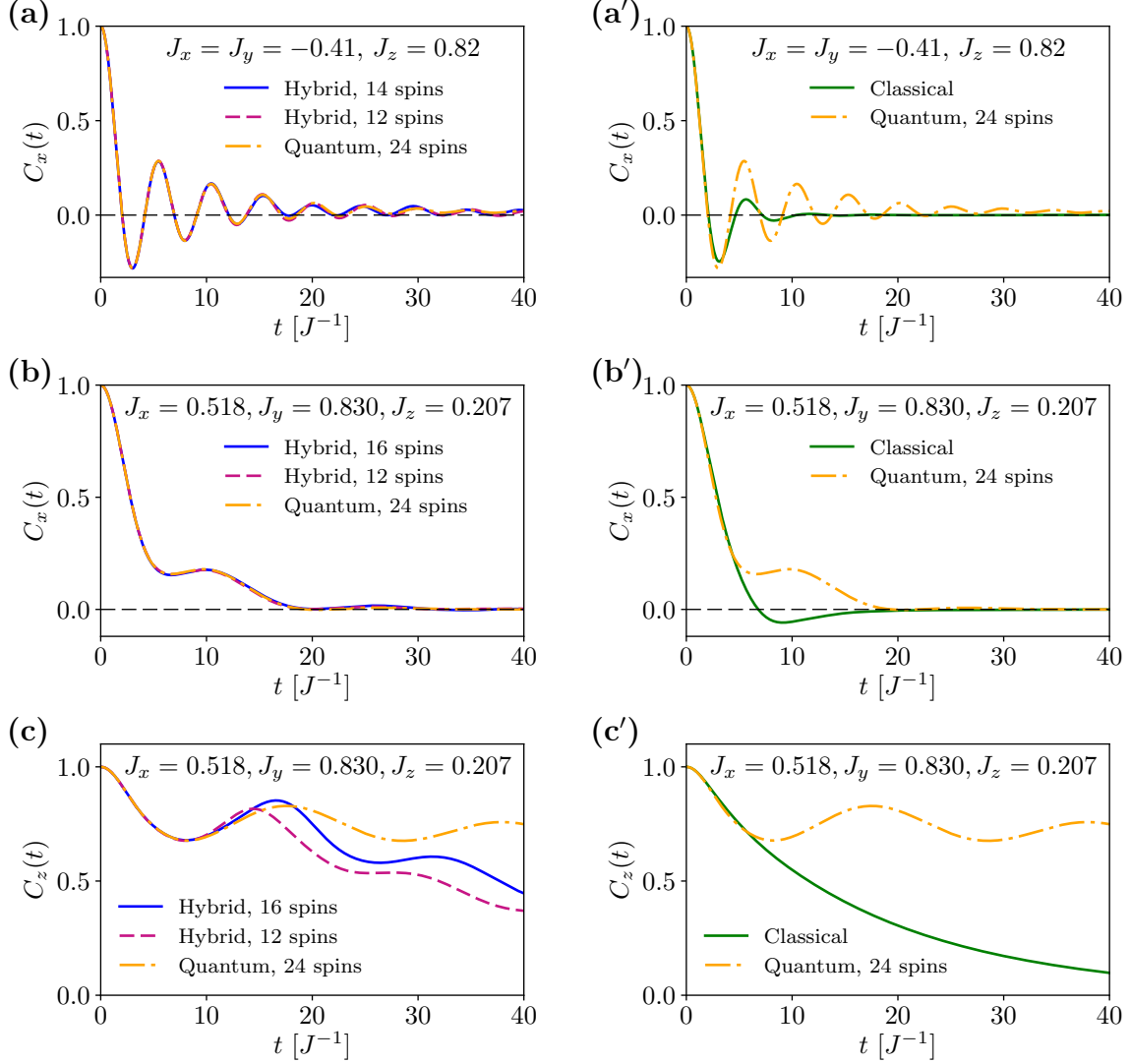


Figure 4.1: Correlation functions $C_\alpha(t)$ for one-dimensional periodic chains with nearest neighbours interactions. The interaction constants are indicated above each plot. The left column of plots compares the results of hybrid simulations with the reference plots obtained by direct quantum calculations. The right column does the same for purely classical simulations. For both hybrid and classical simulations, the full lattice size is 92. The sizes of quantum clusters in hybrid simulations and in reference quantum calculations are indicated in the plot legends.

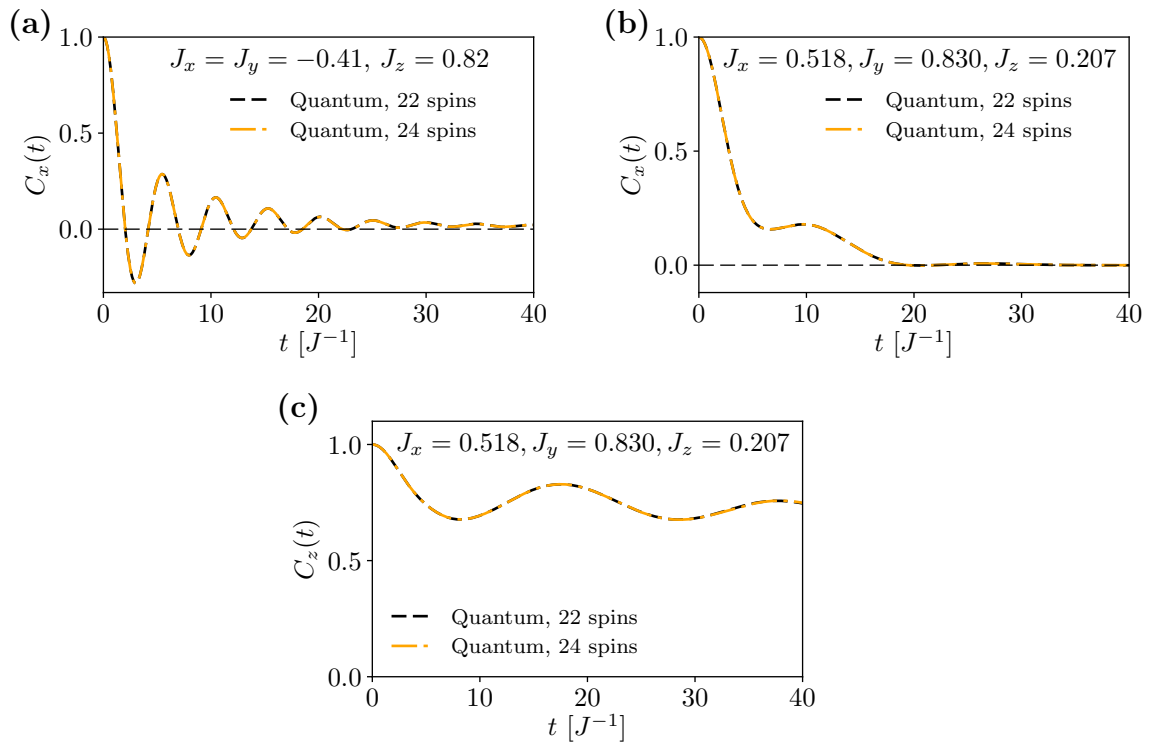


Figure 4.2: Size dependence of correlation functions $C_\alpha(t)$ for one-dimensional periodic chains with nearest-neighbour interactions obtained from direct quantum calculations. The interaction constants are the same as in Fig. 4.1. The present figure illustrates that quantum reference plots used in Fig. 4.1 represent the thermodynamic limit.

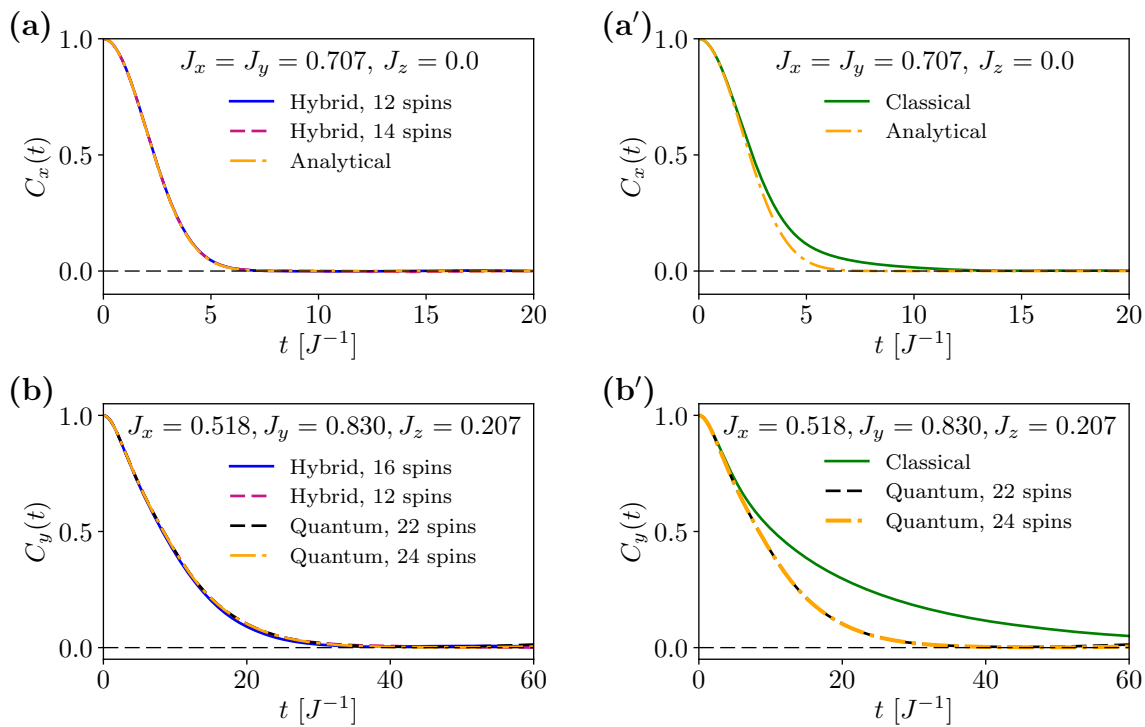


Figure 4.3: Correlation functions $C_\alpha(t)$ for one-dimensional periodic chains with nearest-neighbour interactions. The notations here are the same as in Fig. 4.1. For both hybrid and classical simulations, the full lattice size is 92. Lines in (a,a') labeled as “Analytical” are Gaussians that represent the analytical result for the spin-1/2 XX chain in the thermodynamic limit [51].

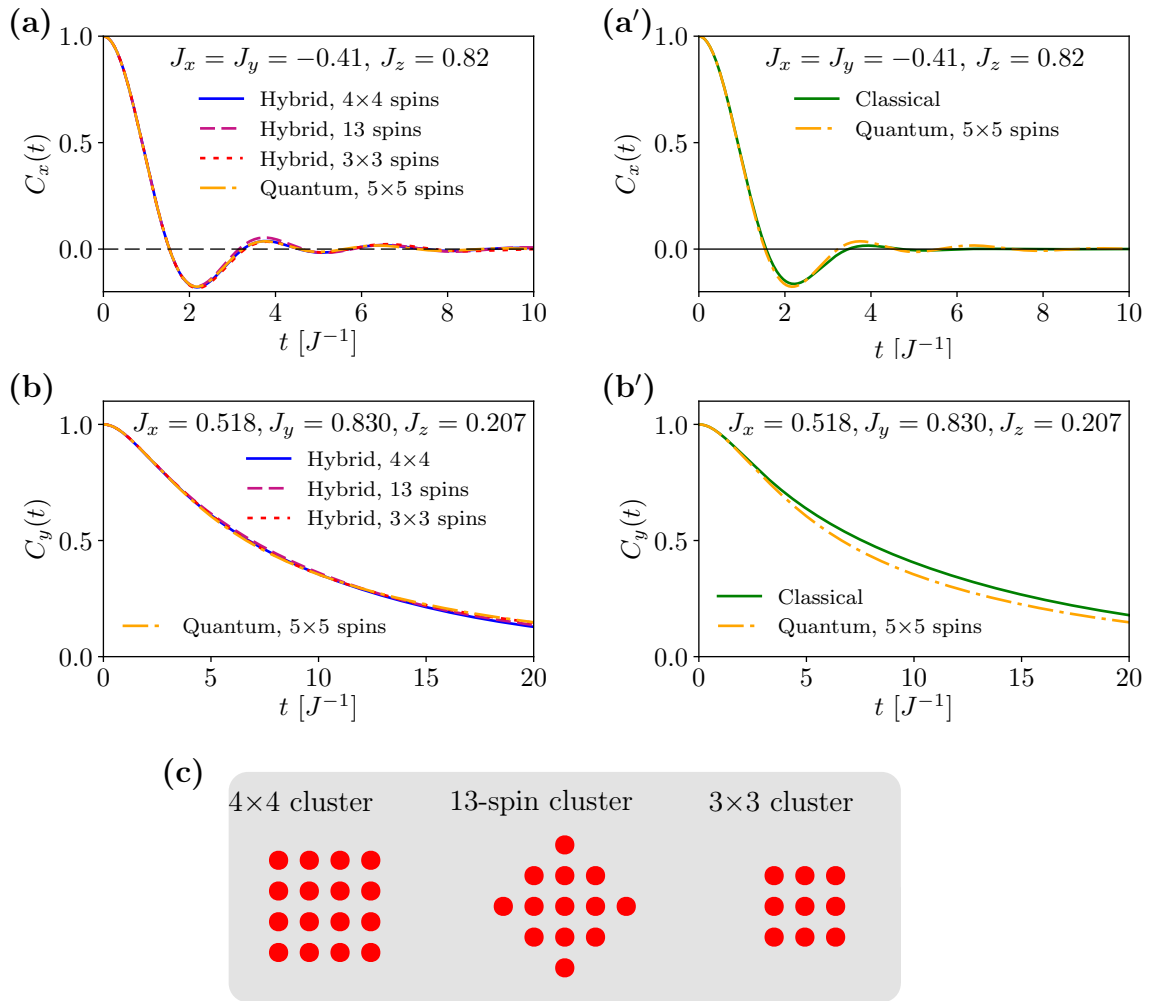


Figure 4.4: Correlation functions $C_\alpha(t)$ for two-dimensional periodic lattices with nearest-neighbour interaction. The notations in (a,a',b,b') are the same as in Fig. 4.1. For both hybrid and classical simulations, the full lattice size is 9×9 . The shapes of quantum clusters for hybrid simulations are shown in (c).

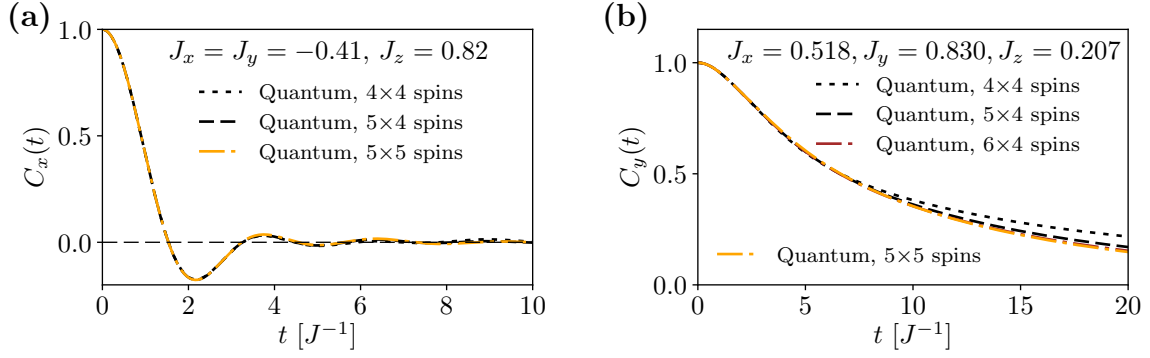


Figure 4.5: Size dependence of correlation functions $C_\alpha(t)$ for two-dimensional periodic chains with nearest-neighbour interactions obtained from purely quantum simulations. The interaction constants are the same as in Fig. 4.4. These plots illustrates that quantum results used in Fig. 4.4 as references represent the thermodynamic limit.

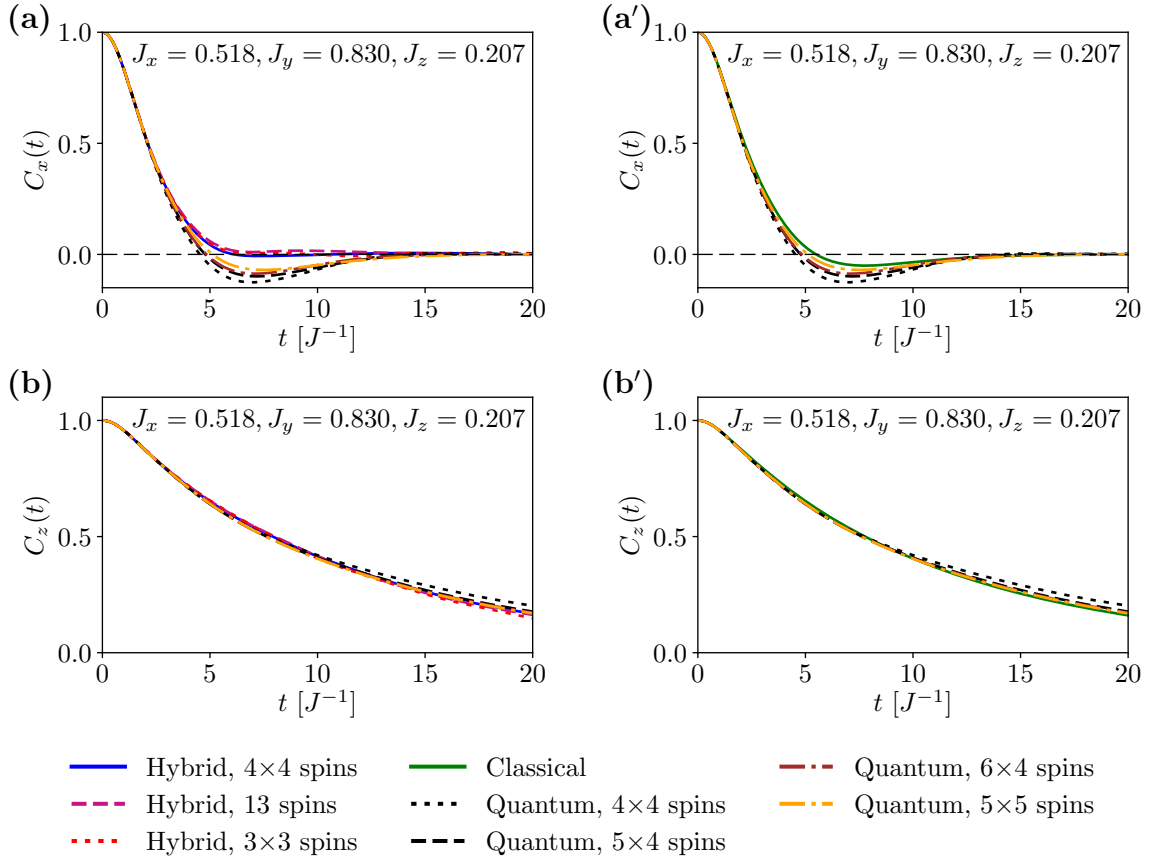


Figure 4.6: Correlation functions $C_\alpha(t)$ for two-dimensional periodic lattices with nearest-neighbour interactions. The notations are the same as in Fig. 4.1. For both hybrid and classical simulations, the full lattice size is 9×9 . The shapes of quantum clusters for hybrid simulations are shown in Fig. 4.1(c).

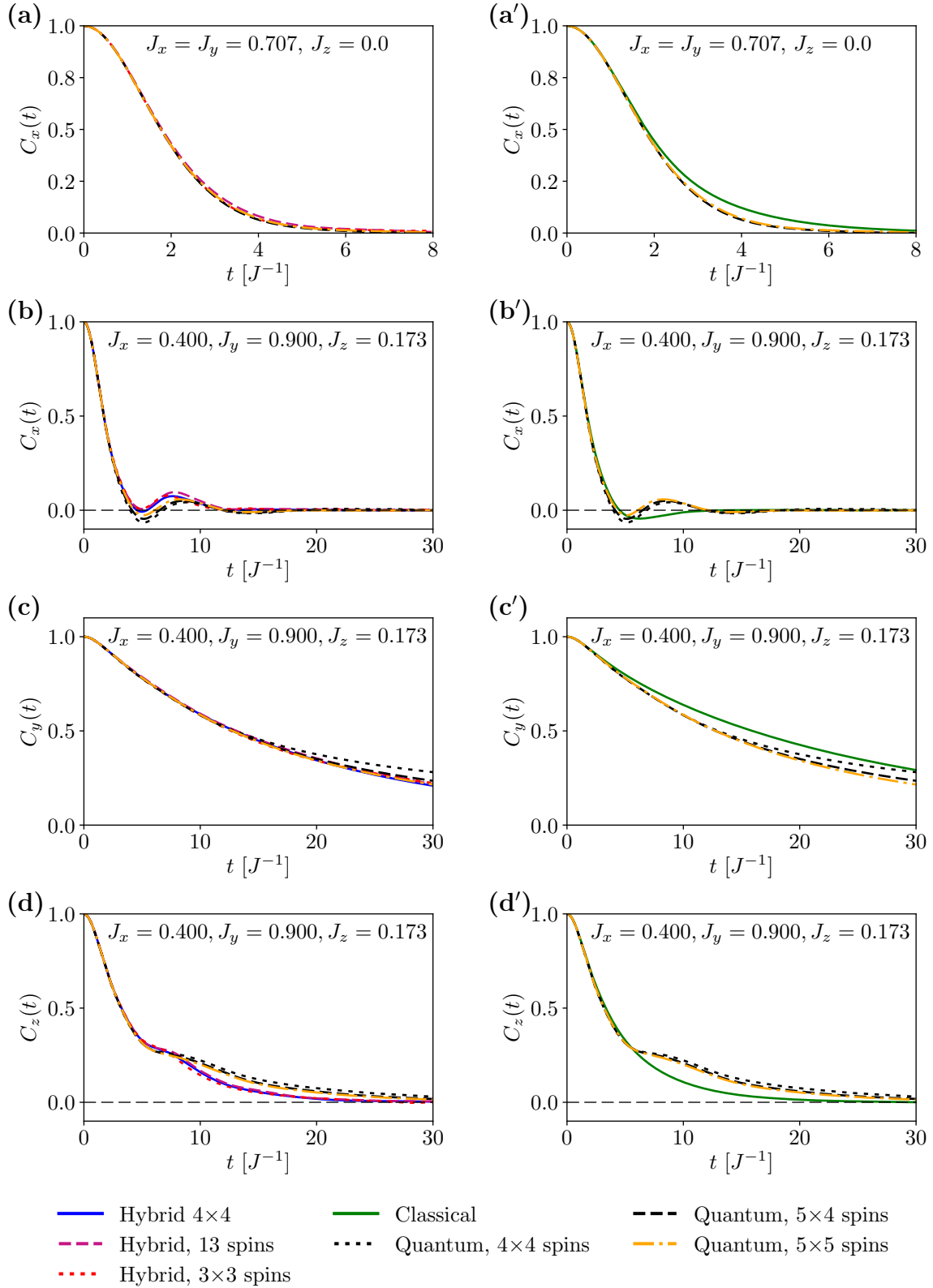


Figure 4.7: Correlation functions $C_\alpha(t)$ for two-dimensional periodic lattices with nearest-neighbour interaction. The notations are the same as in Fig. 4.1. For both hybrid and classical simulations, the full lattice size is 9×9 . The shapes of quantum clusters for hybrid simulations are shown in Fig. 4.1(c).

Chapter 5

Application of the Hybrid Method to the calculations of FIDs in real materials

5.1 FIDs in CaF₂

For three-dimensional lattices, direct numerical calculations of references representing the thermodynamic limit are not feasible, because the required size of the quantum lattice is too large. Therefore, in this case, we test the Hybrid Method by comparing its predictions with the results of NMR FID experiments. Let us consider the case of the benchmark material CaF₂. Magnetically active stable isotope ¹⁹F has natural abundance 100%. As for the stable isotopes of calcium, the only magnetically active one has the natural abundance 0.14%, thus, its presence can be safely neglected. The ¹⁹F nuclei of calcium fluoride have spin 1/2, form a cubic lattice with the lattice parameter $a = 2.72 \text{ \AA}$, and interact *via* truncated magnetic-dipolar interaction given by Eq. (1.25), which, in terms of Hamiltonian (1.52), means that:

$$J_{i,j}^z = -2J_{i,j}^x = -2J_{i,j}^y = \frac{\gamma^2 \hbar (1 - 3 \cos^2 \theta_{ij})}{|\mathbf{r}_{ij}|^3}. \quad (5.1)$$

Here the z -axis is chosen along the direction of external magnetic field \mathbf{B}_0 , \mathbf{r}_{ij} is the vector connecting lattice sites i and j , θ_{ij} is the angle between \mathbf{r}_{ij} and \mathbf{B}_0 . The gyromagnetic ratio of ¹⁹F nuclei is $\gamma = 25166.2 \text{ rad s}^{-1} \text{ Oe}^{-1}$. (As in Eq. (1.10), γ is the fundamental gyromagnetic ratio. See the footnote in the discussion corresponding to Eq. (1.10).)

The FID in calcium fluoride was measured very accurately by Engelsberg and Lowe [52]. In Fig. 5.1, we present the comparison between the experiment and

the results of the hybrid and the classical simulations for magnetic field \mathbf{B}_0 oriented along the [001], [011] and [111] crystal directions. In addition to Fig. 5.1, in Fig. 5.2, we illustrate the statistical uncertainty of the plots of Fig. 5.1 by including the hybrid and the classical plots obtained not only from the full generated statistics but also from the half of it. (The numbers of computational runs for the generated statistics are provided in Section A.4). Comparison of the plots with different statistics indicates that the hybrid plots of Figs. 5.1(b) and 5.1(c) are subject to statistical errors for times $t \gtrsim 125 \mu s$ and for $t \gtrsim 160 \mu s$ respectively.

In this case, classical simulations are known to lead to a good agreement with experiment — consequence of the relatively large effective number of interacting neighbours n_{eff} [31, 59] defined by Eq. (1.73) [31]. According to Ref. [31], the values of n_{eff} for [001], [011] and [111] crystal directions are, respectively, 4.9, 9.1, and 22.2. Given large n_{eff} , the hybrid method was also not expected to generate predictions very different from the classical ones irrespective of the choice of the quantum cluster within the method. Specifically, we chose these clusters as follows: For each orientation of \mathbf{B}_0 , the quantum cluster is chosen in the form of a chain extending along the crystal direction of the strongest nearest-neighbour coupling. We believe this is a reasonable approach to preserve the remaining quantum correlations. Specifically, for \mathbf{B}_0 along the [001] and [111] crystal directions, the cluster chains extend along the direction of \mathbf{B}_0 ; for \mathbf{B}_0 along the [011] direction, the chain extends along the [100] direction. The size of the simulated hybrid lattice is $9 \times 9 \times 9$ spins, which is assumed to accurately represent the hybrid lattice with an infinitely large classical part. This assumption is based on the results of [31], where no significant difference between $9 \times 9 \times 9$ and $11 \times 11 \times 11$ lattices was observed for classical simulations.

All three examples in Fig. 5.1 illustrate the predictive uncertainty criterion formulated earlier, namely, that, for the lattices with a large number of interacting neighbours, the deviation between the predictions of the hybrid and the classical methods quantify the uncertainty of either of them. Indeed, the hybrid and the classical results diverge approximately at the point where they start noticeably deviating from the experimental result.

More detailed comparison of the tests for [001], [011] and [111] directions provides further support for the role of large n_{eff} : Since n_{eff} is significantly larger for [011] and [111] than for [001], the initial agreement between the experiment and both hybrid and classical simulations extends for [011] and [111] over longer initial time, reaching the regime of the exponential-oscillatory asymptotic behavior given by Eq. (4.1), which, in turn, leads to the excellent overall agreement even on semi-logarithmic plots. We note, however, that the statistical uncertainty of the classical and the hybrid plots grows towards the end of the plotting range and, in

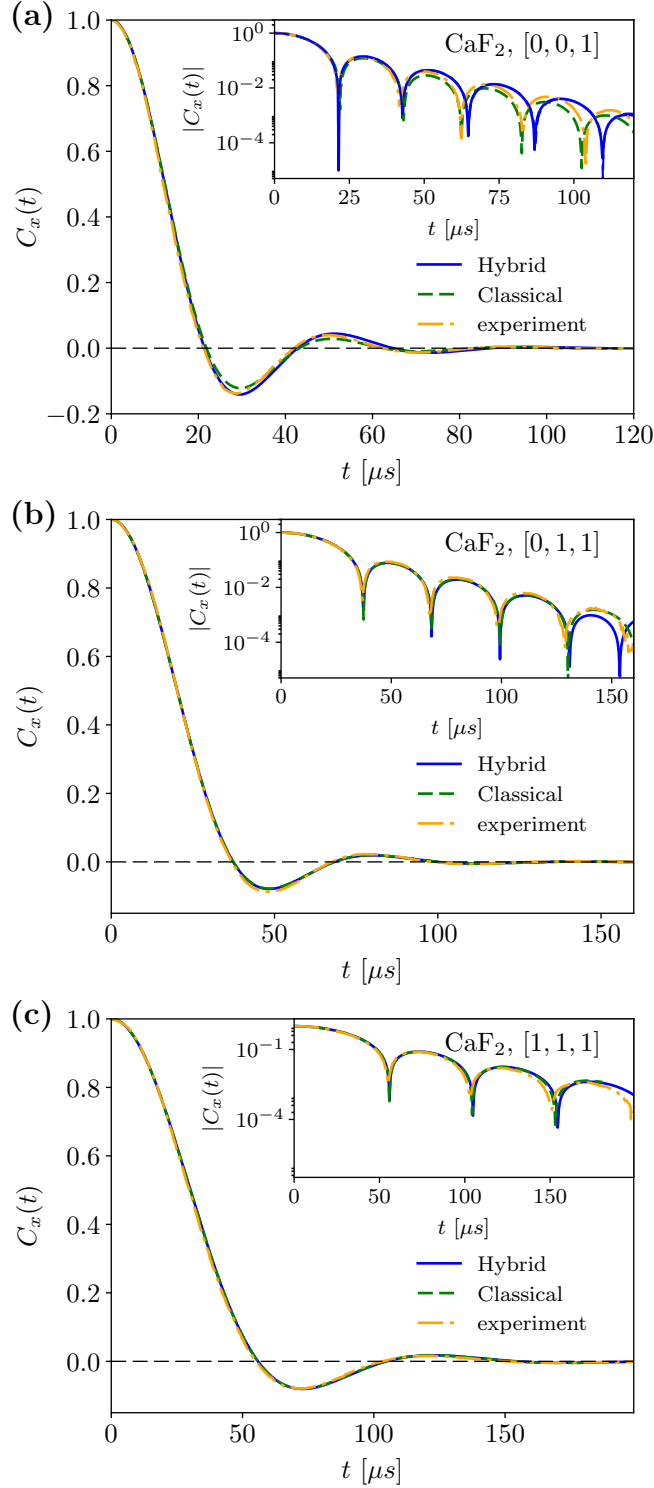


Figure 5.1: FIDs in CaF_2 for external magnetic field \mathbf{B}_0 along the following crystal directions: (a) $[001]$; (b) $[011]$; (c) $[111]$. Hybrid and classical simulations are compared with the experimental results of Ref.[52]. For both hybrid and classical simulations, the full lattice size is $9 \times 9 \times 9$. The quantum cluster in hybrid simulations was a chain extending along $[001]$ crystal direction in (a); a chain passing through the entire lattice and oriented along the $[100]$ crystal direction in (b) and a chain along $[111]$ crystal direction in (c). The insets contain semi-logarithmic plots of the respective FIDs.

| | ω , rad/ms | γ , 1/ms | c | t_0 , μs |
|------------|-------------------|-----------------|------|-----------------|
| Experiment | 152 | 52 | 0.57 | 82.95 |
| Hybrid | 142 | 55 | 0.80 | 87.05 |
| Classical | 158 | 56 | 0.55 | 82.61 |

Table 5.1: The values of the parameters γ , ω , c and t_0 obtained from fitting the functional dependence (4.1) to the FIDs presented on the Fig. 5.1(a). The fitting plots themselves are presented in Fig. 5.3.

some cases, becomes larger than the thickness of the plotted lines, as illustrated in Fig. 5.2. This, likely, explains the discrepancies between the experiment and the simulations for the [011] and [111] directions. However, for the [001] direction, the small discrepancy between the hybrid and the classical simulations seen on the semi-logarithmic plot is statistically significant. It leads to small differences between the parameters characterizing the long-time regime, namely, the constants of exponential decay and the oscillations frequencies. The small differences of these parameters then lead to the growing differences between the classical and the hybrid FIDs at longer times in Fig. 5.1(a). These differences, while barely visible on the linear plot in Fig. 5.1(a), become amplified on the semi-logarithmic plot (inset of Fig. 5.1(a)), where the classical simulations exhibit somewhat better agreement with experiment than the hybrid ones. We believe, however, that this better agreement is accidental. Firstly, the classical simulations in this case do not have the required predictive accuracy. Secondly, the classical simulations appear to perform better, because the phase of the long-time oscillations of the classical FID matches that of the experimental FID. At the same time, the periods of the long-time oscillations of classical, hybrid and experimental FIDs appear to be close to each other. In order to substantiate these views, we extracted the parameters of the long-time fits (4.1) for classical, hybrid and experimental FIDs. The precise functional form of the fits is $C_{\text{fit}}(t) = c \cdot e^{-\gamma t} \cdot \sin[\omega(t - t_0)]$. The fitting curves are displayed in Fig. 5.3. The fitting parameters are presented in Table 5.1 There one can observe that both classical and hybrid calculations predict the long-time exponential decay constants and frequencies with accuracy 5-7 percent, and the experimental values fall just into this range.

Beyond CaF_2 , the hybrid method is supposed to be of the most value in those cases, where the direct quantum simulations cannot access the thermodynamic limit for the correlation functions of interest, while, at the same time, the effective number of interacting neighbours n_{eff} is not large enough to justify purely classical calculations — for example, three-dimensional lattices that can be divided into one-dimensional chains with stronger coupling within each chain and weaker coupling between the chains, such as fluorapatite [60]; or when spins can be di-

vided into strongly coupled pairs as in ^{13}C diamond or ^{29}Si silicon with external magnetic field along the $[111]$ direction [61, 62]. The performance of the hybrid method in the above settings is considered in Sections 5.2 and 5.3 of this Chapter.

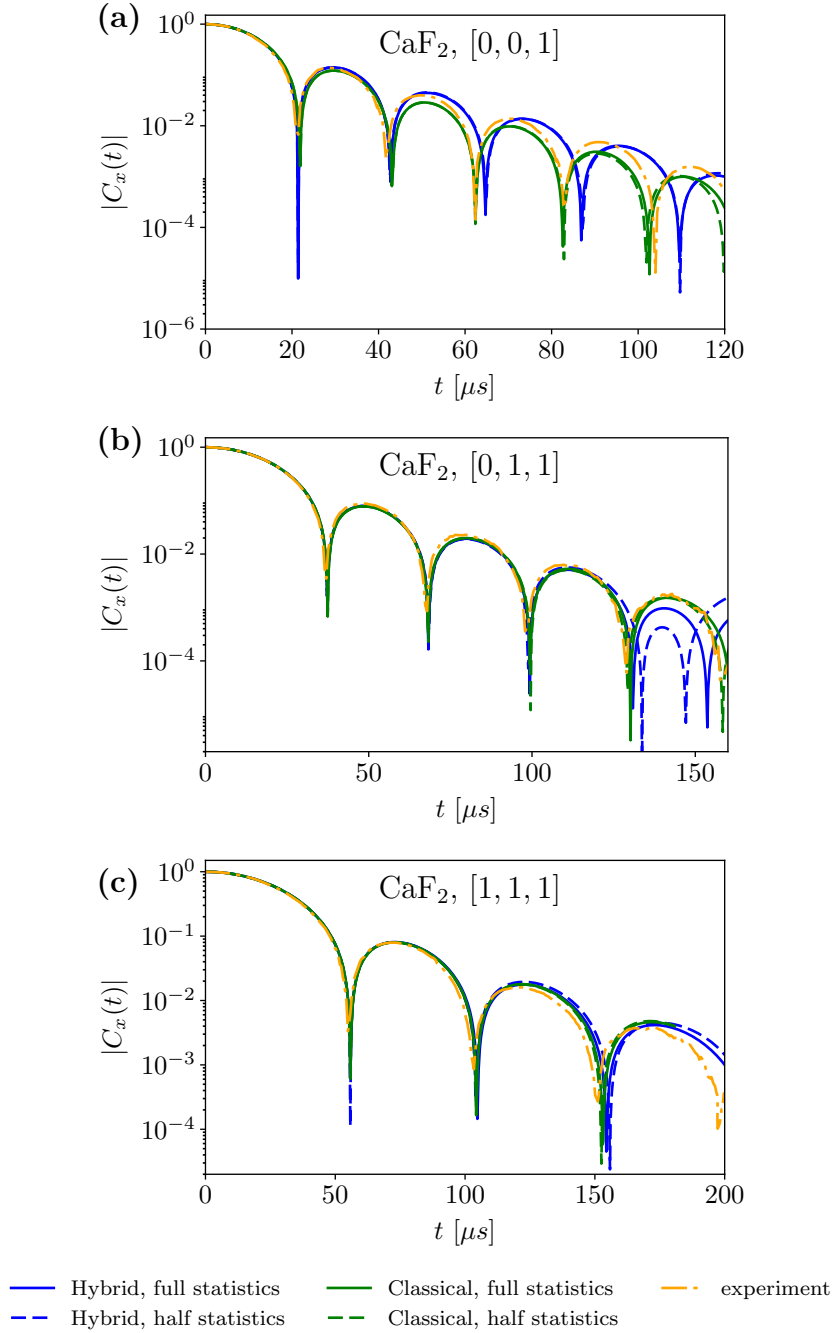


Figure 5.2: Illustration of the statistical uncertainty of the hybrid and the classical plots of CaF_2 FIDs appearing in Fig.5.1. Here, panels (a), (b) and (c) include hybrid and classical plots obtained not only from the full generated statistics but also from the half of it — see the plot legend. The total number of computational runs corresponding to the full generated statistics is listed in Table A.1.

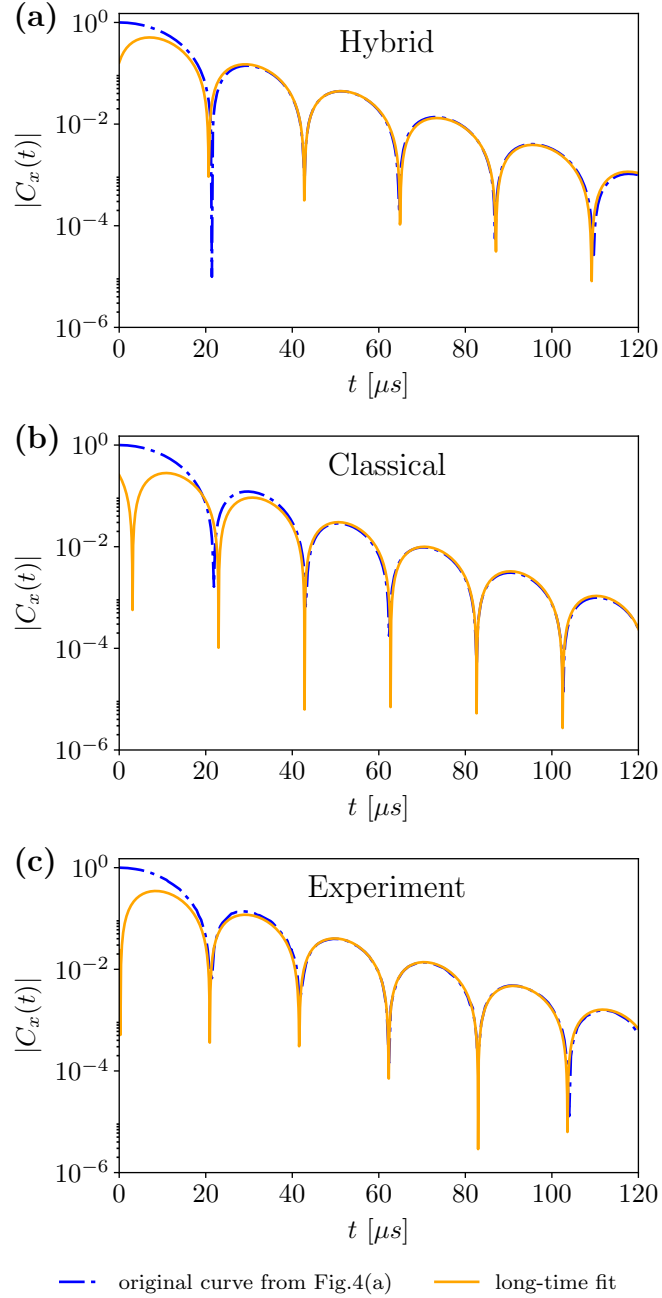


Figure 5.3: Long-time fits to the experimental and computed FIDs in CaF_2 for external magnetic field \mathbf{B}_0 along the [001] crystal direction. The three original plots are from the semilogarithmic inset of Fig.5.1(a): (a) hybrid calculation, (b) classical calculation, (c) experiment. The functional form of the fits is $C_{\text{fit}}(t) = c \cdot e^{-\gamma t} \cdot \sin[\omega(t - t_0)]$. Parameters γ , ω , c and t_0 are listed in Table 5.1.

5.2 FID in isotopically enriched ^{29}Si silicon

The majority of the methods proposed in the past seldom went beyond the case of FID in calcium fluoride to test their predictions. In order to establish the validity of the Hybrid Method as a reliable tool for calculations, it is important to apply the method to the calculation of FID in a material with the magnetic nuclei arranged in a crystal structure completely different to the one of calcium fluoride. A good candidate structure to consider is that of a diamond. It is important not only as another testing ground for FID theories. The study of materials with such structure gains the significance in light of the development of quantum computers and quantum sensors based on the impurities introduced into the diamond.

The diamond crystal structure is exhibited, for example, by the materials consisting of the atoms of the 4-th group of the periodic table of elements: C, Si and Ge. Among them, only carbon and silicon have stable isotopes with nuclear spin $1/2$. These are ^{13}C and ^{29}Si respectively. The natural abundance of these isotopes is quite low: 1.1% for ^{13}C and 4.7% for ^{29}Si . However, crystals enriched to almost 100% abundance of these particular isotopes can be grown artificially.

The FIDs of almost 100% ^{13}C -enriched diamond were measured in the past by Lefmann et al. [61], while the FIDs of almost 100% ^{29}Si -enriched silicon were measured by Verhulst et al. [62]. The FID shapes obtained in both cases are supposed to coincide provided one of the curves is stretched along the time axis so that the time-scales are matched. However, the comparison of the results from experiments of Lefmann et al. and Verhulst et al. indicates the two FIDs do not quite coincide. Both experiments are not ideal: there is a noticeable discrepancy between the experimental and the theoretical values of second moments¹, which is most prominent for the case of the external magnetic field along the [100] crystal direction. However, in the case of the ^{29}Si experiment [62] this discrepancy was smaller than in the case of the ^{13}C experiment [61]. Additionally, Lefmann et al. used a relatively high repetition rate and their absorption curves exhibit noticeable asymmetry. Thus, the results of Verhulst et al. appear to be more accurate, so we use them to test the hybrid method.

On the theoretical side, the FIDs for the diamond lattice were calculated by Jensen [16] and by Lundin and Zobov [63]. The former paper used an approach based on the truncation of the continued fraction representation of the Laplace transform of the FID. The calculation in the latter paper used the scheme introduced in the 1996 paper of Lundin [28], which was based on the hypothesis of the asymptotic similarity of correlations functions of various orders (see the review of literature in Section 1.4).

¹The value of the second moment can be computed from the first principles exactly.

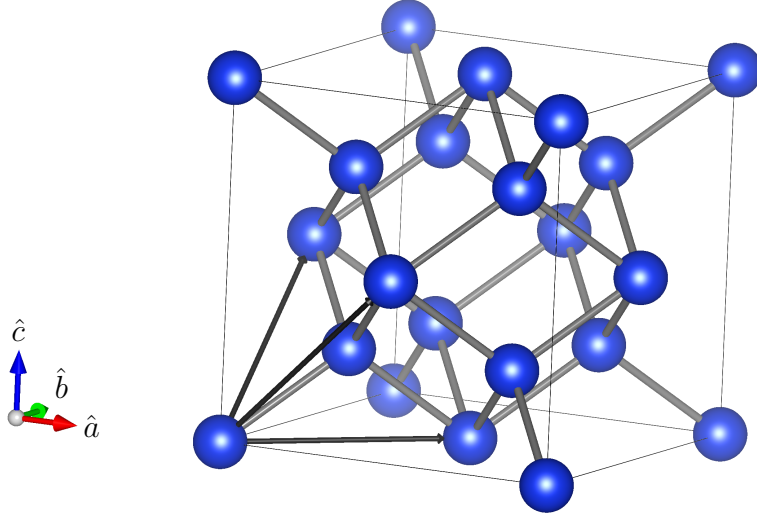


Figure 5.4: Diamond crystal structure. The black arrows represent the primitive vectors of the lattice.

The diamond crystal structure is presented in Fig. 5.4. It is a face-centered cubic lattice with a two-site basis. The center of the unit cell is an inversion center of the lattice. As a consequence, two lattice sites of the unit cell are, in fact, equivalent.

The primitive vectors of the lattice are

$$\mathbf{l}_1 = \frac{a_0}{2}(\hat{a} + \hat{b}), \quad \mathbf{l}_2 = \frac{a_0}{2}(\hat{b} + \hat{c}), \quad \mathbf{l}_3 = \frac{a_0}{2}(\hat{a} + \hat{c}), \quad (5.2)$$

and two vectors of the basis are:

$$\mathbf{v}_0 = \mathbf{0}, \quad \mathbf{v}_1 = \frac{a_0}{4}(\hat{a} + \hat{b} + \hat{c}), \quad (5.3)$$

where a_0 is the period of the fcc lattice (see also [7, Chapter 4]). For silicon diamond $a_0 = 5.431 \text{ \AA}$. Additionally, we need the value of the gyromagnetic ratio for ^{29}Si isotope, which is $\gamma = -5319 \text{ rad s}^{-1} \text{ Oe}^{-1}$.

As in the case of CaF_2 , we consider three different cases corresponding to the external magnetic field \mathbf{B}_0 parallel to $[001]$, $[011]$, and $[111]$ crystal directions. These directions are determined with respect to the axes of a cubic unit cell of the fcc lattice. The effective numbers of interacting neighbours in these three cases are 27.4, 5.9 and 2.4 respectively. According to the investigations of Elsayed and Fine [31], the classical simulations are expected to perform well when $n_{\text{eff}} > 4$. In the cases where \mathbf{B}_0 is along $[001]$ and $[011]$ crystal directions, n_{eff} is quite large. As a consequence, in order to estimate the uncertainty of our simulations, we chose to compare the results of hybrid simulations with the results of the classical

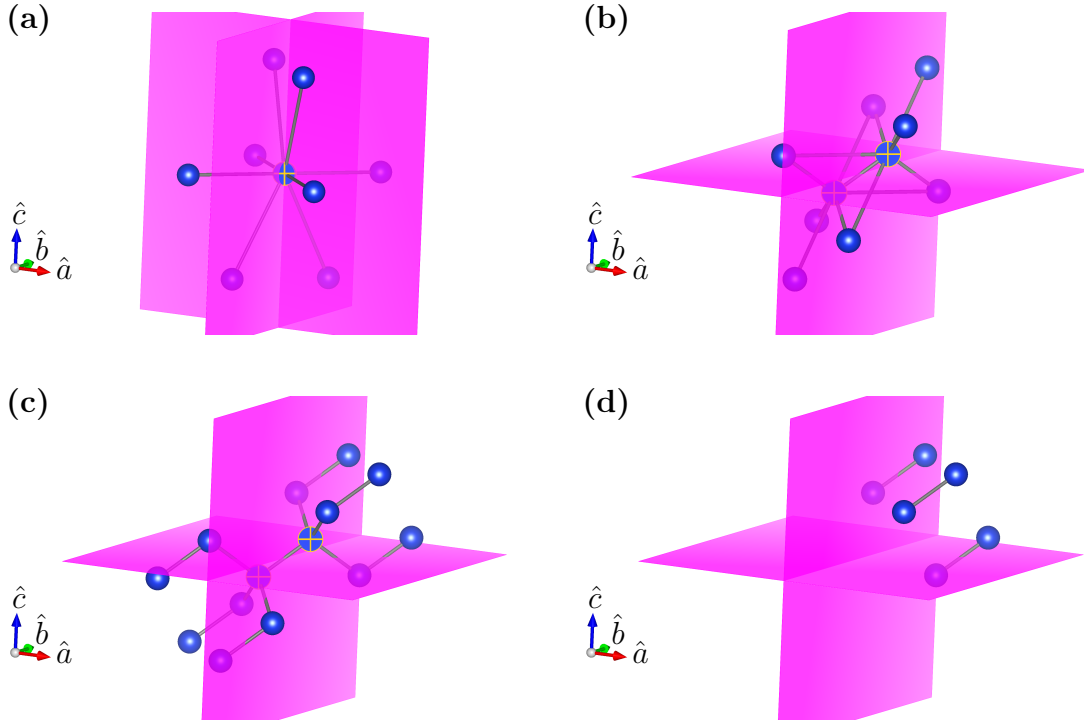


Figure 5.5: Schemes of the quantum clusters used for the hybrid simulations: **(a)** cluster used for the case when $\mathbf{B}_0 \parallel [001]$; **(b)** cluster used for the case when $\mathbf{B}_0 \parallel [011]$; **(c)**, **(d)** cluster 1 and cluster 2 respectively, used for the case when $\mathbf{B}_0 \parallel [111]$. Marked sites correspond to the central spins of the clusters.

simulations in these two cases. In the case where \mathbf{B}_0 is along $[111]$ crystal direction, n_{eff} is small, so that the classical simulations are expected to be inaccurate. Thus, in order to estimate the uncertainty of our simulations, we chose to compare the results of two hybrid simulations with the different choices of quantum clusters in this case. The schemes of the quantum clusters used in the simulations are shown in Fig. 5.5.

The results of our simulations are presented in Figs. 5.6, 5.7, and 5.8 for external magnetic field \mathbf{B}_0 along $[001]$, $[011]$ and $[111]$ crystal directions respectively. All three figures have identical structure. The upper row (frames **(a)** and **(a')**) presents the absorption peak line-shape $f(\nu)$ defined by Eq. (1.29) ($\nu \equiv u/(2\pi)$). Each of the absorption curves is normalized in such a way that the area under the curve is equal to one if described in terms of units of the figure axes. The lower row (frames **(b)** and **(b')**) presents the FID. The left column frames compare the results of our simulations with the experimental data of Verhulst et al. [62]. The right column frames compare the theoretical predictions of Jensen [16] and Lundin and Zobov [63] with the same experimental data. For each of the three specified crystal directions, Verhulst et al. performed several measurements

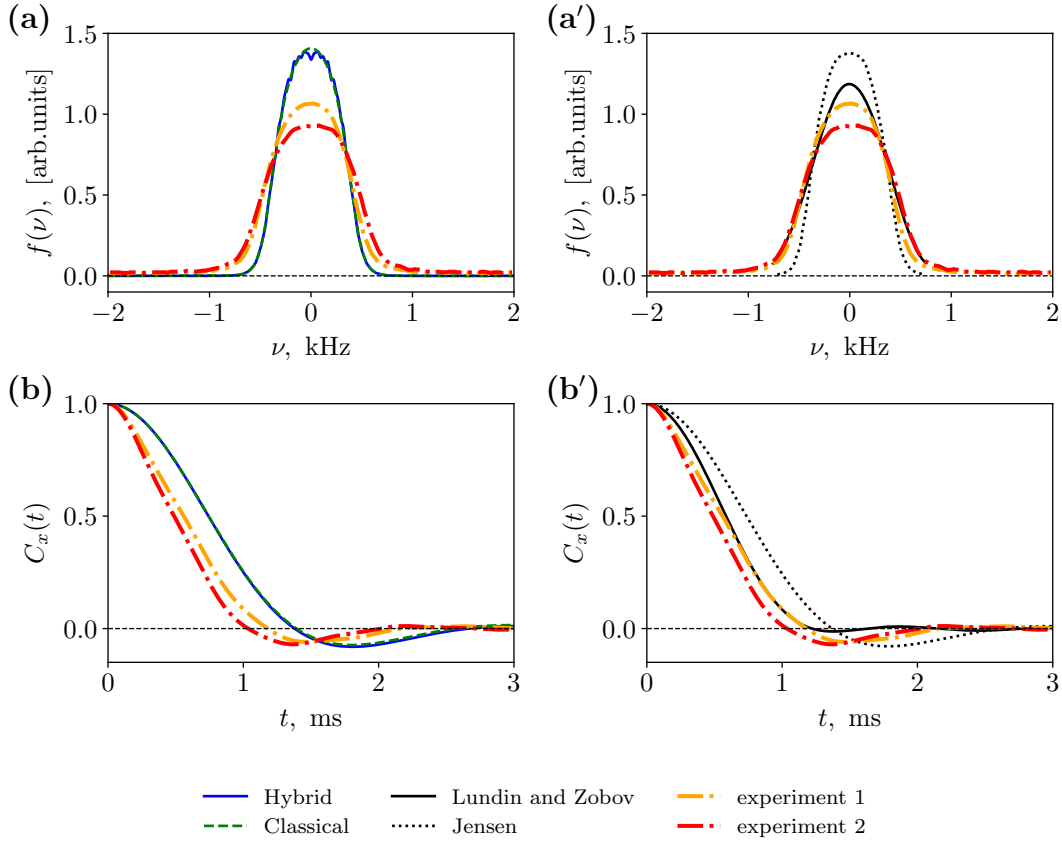


Figure 5.6: Absorption peak lineshape (a),(a') and FID (b),(b') in ^{29}Si diamond for \mathbf{B}_0 along [001] crystal direction. In the left column, we present the comparison of the hybrid and the classical simulations with two experimental curves of Verhulst et al. for the same orientation of the magnetic field. In the right column, we present the comparison of the theoretical predictions of Jensen and Lundin and Zobov with the same experimental data. The scheme of the quantum cluster used in the hybrid simulation is displayed in Fig. 5.5(a).

for external magnetic field oriented nearly along the indicated crystal direction and its symmetrical equivalents. In each of the cases, these several measurements produced slightly different results. These deviations can be attributed to the inaccuracies in the positioning of the sample. In order to quantify the experimental uncertainty, for each of the crystal directions we chose two experimental curves for magnetic fields along this direction or its equivalents (labelled as “experiment1” and “experiment2” in the plot legends).

Let us also specify the details of our simulations. For \mathbf{B}_0 along [001] and [011] crystal directions, we used the freedom in the choice of the basis and the primitive vectors to specify the full lattice. Instead of the two-site basis cell (see Eq. 5.3) we used an eight-site basis cell containing original two-node basis cell and its three

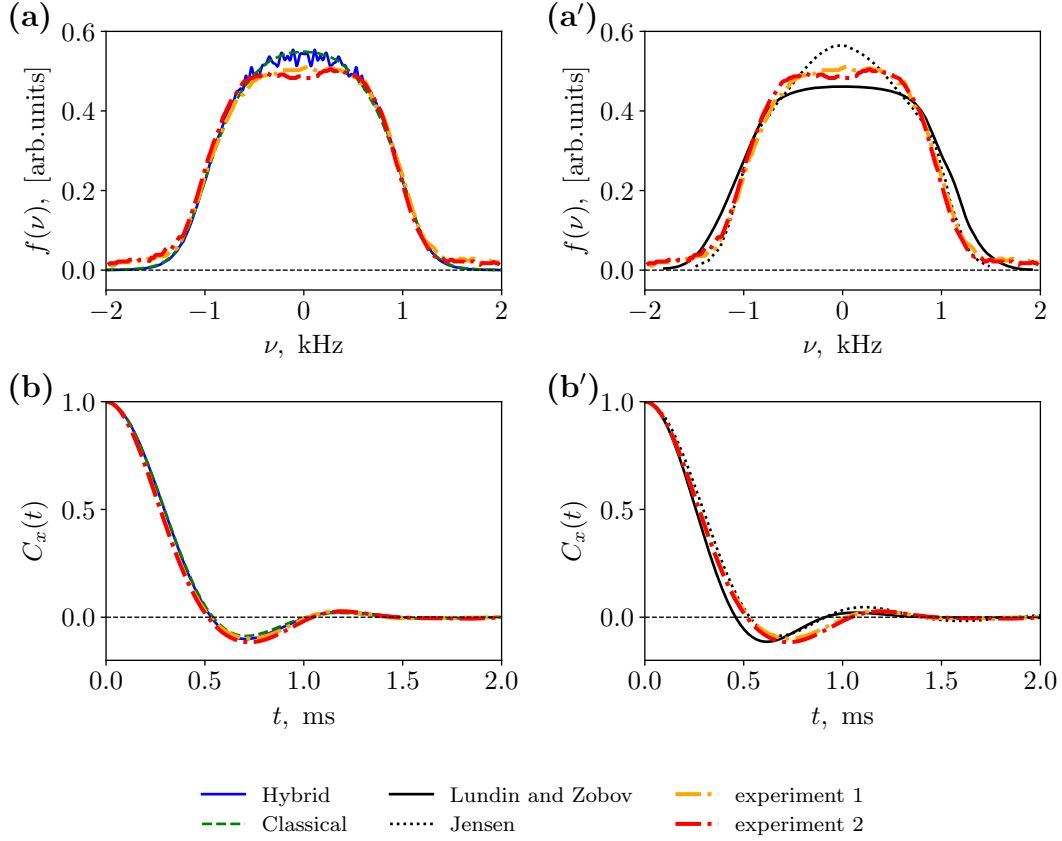


Figure 5.7: Absorption peak line-shape (a),(a') and FID (b),(b') in ^{29}Si diamond for \mathbf{B}_0 along [011] crystal direction. In the left column, we present the comparison of the hybrid and the classical simulations with two experimental curves of Verhulst et al. for the same orientation of the magnetic field. In the right column, we present the comparison of the theoretical predictions of Jensen and Lundin and Zobov with the same experimental data. The scheme of the quantum cluster used in the hybrid simulation is displayed in Fig. 5.5(b).

translations by the original primitive vectors (Eq. 5.2):

$$\begin{aligned}
 \mathbf{v}'_0 &= \mathbf{v}_0, & \mathbf{v}'_2 &= \mathbf{v}_0 + \mathbf{l}_1, & \mathbf{v}'_4 &= \mathbf{v}_0 + \mathbf{l}_2, & \mathbf{v}'_6 &= \mathbf{v}_0 + \mathbf{l}_3, \\
 \mathbf{v}'_1 &= \mathbf{v}_1, & \mathbf{v}'_3 &= \mathbf{v}_1 + \mathbf{l}_1, & \mathbf{v}'_5 &= \mathbf{v}_1 + \mathbf{l}_2, & \mathbf{v}'_7 &= \mathbf{v}_1 + \mathbf{l}_3.
 \end{aligned} \tag{5.4}$$

The corresponding set of primitive vectors was

$$\mathbf{l}'_1 = a\hat{a}, \quad \mathbf{l}'_2 = a\hat{b}, \quad \mathbf{l}'_3 = a\hat{c}. \tag{5.5}$$

The full lattice size for the hybrid and the classical simulations was $7 \times 7 \times 7$ eight-site basis cells including 2744 lattice sites in total. Periodic boundary conditions were used with respect to the new set of primitive vectors.

For the orientation of external magnetic field \mathbf{B}_0 along the [001] crystal direc-

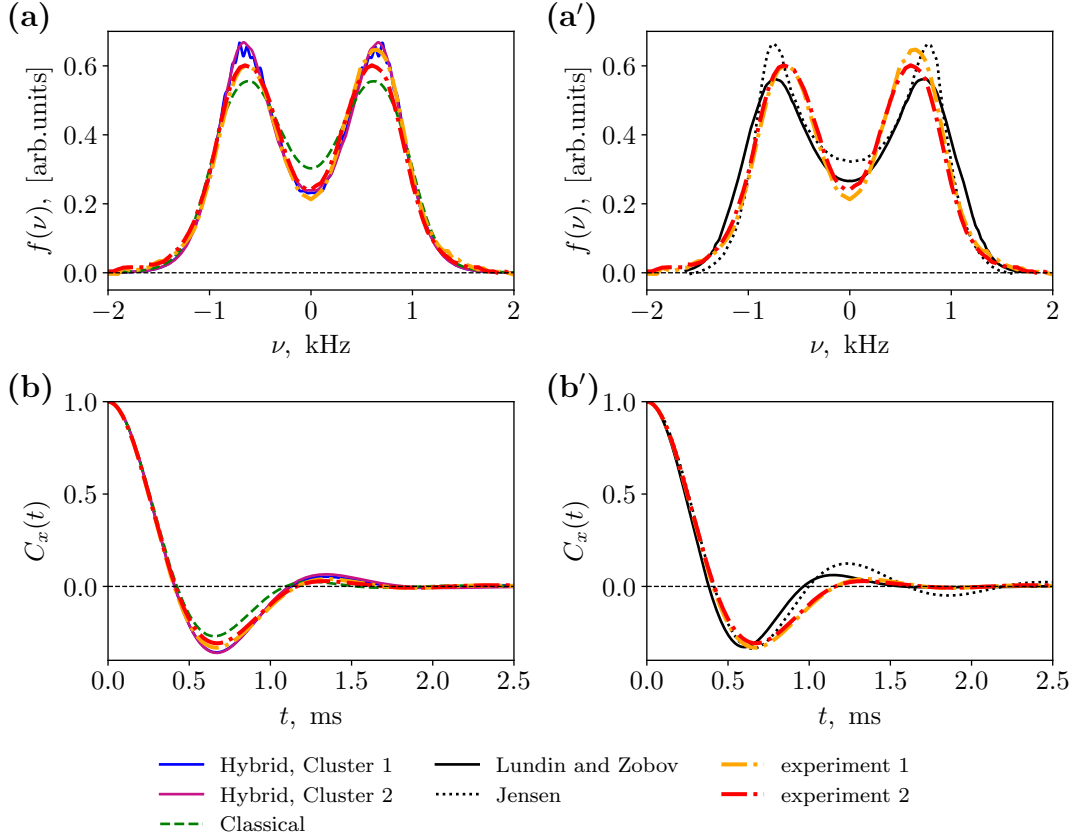


Figure 5.8: Absorption peak line-shape (a),(a') and FID (b),(b') in ^{29}Si diamond for \mathbf{B}_0 along [111] crystal direction. In the left column, we present the comparison of the hybrid simulations for two choices of the quantum cluster and of the classical simulations with two experimental curves of Verhulst et al. for the same orientation of the magnetic field. In the right column, we present the comparison of the theoretical predictions of Jensen and Lundin and Zobov with the same experimental data. The schemes of the quantum clusters used in the hybrid simulations are displayed in Figs. 5.5(c,d).

tion, we chose the zero site of the basis cell (specified by \mathbf{v}'_0) as a central spin in Eq. (3.15) to correlate with the rest of the lattice. In order to construct the quantum cluster, we took the central spin and added 8 spins with which its interaction was the strongest. If we identify the origin of the coordinate system with the position of the central spin, the coordinates of the spins of the cluster in units of a_0 are:

$$\begin{aligned}
 & [0.0, 0.0, 0.0], & [-0.5, -0.5, 0.0], & [0.5, -0.5, 0.0], \\
 & [-0.5, 0.5, 0.0], & [0.5, 0.5, 0.0], & [-0.25, -0.25, -0.75], \\
 & [0.25, -0.25, 0.75], & [-0.25, 0.25, 0.75], & [0.25, 0.25, -0.75].
 \end{aligned} \tag{5.6}$$

The scheme of the cluster is presented in Fig. 5.5 (a).

For the orientation of external magnetic field \mathbf{B}_0 along the [011] crystal direction, we chose two sites of the basis cell, specified by \mathbf{v}'_0 and \mathbf{v}'_1 , as the central spins in Eq. (3.15) to correlate with the rest of the lattice. The quantum cluster was comprised of these two central spins and 8 spins with which their interaction was the strongest. If we identify the origin with the node specified by \mathbf{v}'_0 , the coordinates of the spins of the quantum cluster in units of a_0 are:

$$\begin{aligned}
 & [0.0, 0.0, 0.0], & [0.25, 0.25, 0.25], & [0.5, 0.0, 0.5], \\
 & [0.0, 0.5, 0.5], & [0.5, 0.5, 0.0], & [0.25, 0.75, 0.75], \\
 & [-0.25, 0.25, -0.25], & [-0.25, -0.25, 0.25], & [0.25, -0.25, -0.25], \\
 & [0.0, -0.5, -0.5].
 \end{aligned} \tag{5.7}$$

The scheme of the cluster is presented in Fig. 5.5 (b).

For the orientation of external magnetic field \mathbf{B}_0 along the [111] crystal direction, we specified the lattice with the help of the original two-site basis cell and the original set of primitive vectors (see Eqs. 5.2 and 5.3). The full lattice size for the hybrid and the classical simulations was $9 \times 9 \times 9$ two-site cells including 1458 lattice sites in total. In this particular case, the strongest interaction is between the spins of the same two-site cell. The next in strength interactions are between the nearest spins of the different two-site cells. The schemes of cluster 1 and cluster 2 are presented in Fig. 5.5 (c) and (d) respectively. We chose the quantum cluster 1 to contain a two-site cell and its translations by primitive vectors and their inverses, 7 pairs in total. In the FID calculation, the central spin pair of the cluster was correlated with the rest of the lattice (see Eq. (3.15)). Cluster 2 was obtained from cluster 1 by leaving only three two-node cells obtained by primitive vectors translations; all three pairs were correlated with the rest of the lattice in the FID calculation (see Eq. (3.15)).

Conclusive analysis of the results of our simulations is hindered by the inaccuracies of the experimental data. There are large discrepancies between the experimental second moments M_2^e and the theoretical second moments M_2^t . For \mathbf{B}_0 along the [111], [011] and [001] crystal directions, the relative difference $\frac{M_2^e - M_2^t}{M_2^t}$ takes the values 0.35, 0.4 and 1.73 respectively. Additionally, the experimental results exhibit noticeable uncertainties.

For \mathbf{B}_0 along the [111], [011] crystal directions, the discrepancy in the second moments is small relative to its value for \mathbf{B}_0 along the [001] crystal direction. Therefore, we believe it is reasonable to compare the theoretical predictions with experiment at least for the cases where \mathbf{B}_0 is along the [111], [011] crystal directions. In both cases, the agreement between the results of our simulations and the experimental data is very good. The deviations are of the order of experimental

uncertainty. At the same time, the theoretical predictions of Jensen and of Lundin and Zobov exhibit noticeably larger deviations from the experimental data.

Overall, the case of \mathbf{B}_0 along the [111] crystal direction is the most interesting to discriminate between theoretical predictions, because n_{eff} is the smallest in this case. Although the conclusive discrimination between the theoretical methods can be made only once more accurate experiments are conducted, the results of our simulations look very promising at this stage.

5.3 Calculation of FID in the presence of disorder and unlike spins: the case of calcium fluorapatite.

Calcium Fluorapatite $\text{Ca}_{10}(\text{PO}_4)_6\text{F}_2$ is a material naturally used to study spin dynamics in low-dimensional systems [64, 65, 66, 67, 68, 69, 70]: The fluorine nuclei are arranged in parallel chains. For the orientation of the external magnetic field parallel to the chains, the interactions between them are much smaller than the interaction within the chain. As a result, calcium fluorapatite serves as an example of a quasi one-dimensional system.

Application of the Hybrid Method to the simulation of fluorine FID in fluorapatite pursues several goals. First of all, the effective number of interacting neighbours $n_{\text{eff}} \approx 2$, so this is a natural case when we expect the Hybrid Method to be particularly useful. Secondly, our approach allows us to fully consider the three-dimensional geometry of the crystal, which also enables us to quantify the uncertainty introduced when we neglect the interaction between different fluorine chains. Finally, accurate calculation of the FID requires taking into account the presence of phosphorus spins and of the lattice disorder.

The FID in fluorapatite for the direction of the magnetic field parallel to the fluorine chains has been measured by Engelsberg, Lowe and Carolan [60]. We compare the experimental data of this paper with the results of our simulations.

5.3.1 Structure of calcium fluorapatite

The magnetically active isotopes of calcium and oxygen have natural abundances less than 1%, hence, we can neglect them. At the same time, the naturally abundant stable isotopes ^{19}F and ^{31}P have spins 1/2 and abundances close to 100%. Their gyromagnetic ratios are $\gamma_F = 25166.2 \text{ rad s}^{-1} \text{ Oe}^{-1}$ and $\gamma_P = 10829.1 \text{ rad s}^{-1} \text{ Oe}^{-1}$ respectively. Thus, we consider only the subsystems of fluorine and phosphorus nuclei.

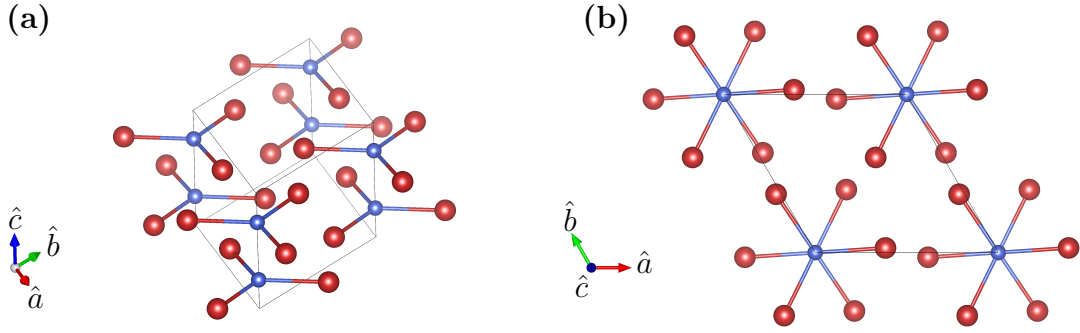


Figure 5.9: Scheme of a unit cell of fluorapatite in two different projections ((a) and (b)). Only F (blue) and P (red) atoms are shown.

Fluorapatite has the hexagonal crystal structure with the space group $P6_3/m$ [71]. The lattice parameters are $a = b = 9.462 \text{ \AA}$ and $c = 6.849 \text{ \AA}$. The \mathbf{c} -axis is orthogonal to the (\mathbf{a}, \mathbf{b}) plane and the angle between two primitive vectors \mathbf{a} and \mathbf{b} is 120° . The basis cell of the sublattice of magnetically active nuclei contains two F nuclei at positions

$$[0.0, 0.0, 0.25], \quad [0.0, 0.0, 0.75] \quad (5.8)$$

and six P nuclei at positions

$$\begin{aligned} [x, y, 0.25], & \quad [1 - y, x - y, 0.25], \quad [y - x, 1 - x, 0.25], \\ [1 - x, 1 - y, 0.75], & \quad [y, y - x, 0.75], \quad [x - y, x, 0.75], \end{aligned} \quad (5.9)$$

where $x = 0.369$ and $y = 0.3985$. The coordinates are given in terms of the basis of primitive vectors \mathbf{a} , \mathbf{b} and \mathbf{c} . An illustration of the unit cell of fluorapatite is presented in Fig. 5.9. The positions of the ^{19}F nuclei inside the basis cell are, in fact, equivalent, since they are transformed into each other by the action of the discrete symmetries of the lattice. Similarly, the positions of the ^{31}P nuclei inside the basis cell are equivalent too.

The ^{19}F atoms are arranged in parallel chains with the inter-chain distance between atoms being approximately 2.8 times larger than the intra-chain one. Since the magnetic dipolar-dipolar interaction scales as r^{-3} , in the case when the external magnetic field is parallel to the chains, the largest value of intra-chain coupling is at least 21 times smaller than the nearest-neighbour coupling inside a chain. Thus, fluorapatite serves as a natural realisation of a quasi-one-dimensional system.

5.3.2 Defects and disorder

The main type of defects in fluorapatite is the substitutions of F^- ions by other X^- ions. Usually F^- ions are substituted by Cl^- ions or by hydroxyl groups $(OH)^-$ [71]. The presence of defects disrupts the fluorine chains and, in principle, leads to the adjustment of the positions of the neighbouring atoms. The picture is further complicated by the fact that both protons of the $(OH)^-$ group and stable isotopes of chlorine are magnetically active. If we assume the concentration of the defects to be small, we can neglect the interaction between spatially separated defect spins. These unlike spins then lead to the inhomogeneous broadening of the z -components of the local magnetic fields sensed by the neighbouring ^{19}F and ^{31}P nuclei. An accurate calculation of FID should account for all of the mentioned effects. To the best of our knowledge, there is no detailed data about the concentrations of different types of defects in the sample used in the experiment [60], or about the adjustment of the positions of atoms due to the presence of defects. In principle, the concentration of defects can be estimated from the comparison of the experimental second moment with the theoretical one, however, in order to do that, the knowledge about the relative concentrations of different types of defects is required. Nevertheless, we can still hope that it is possible to obtain qualitatively accurate results if we neglect these two effects.

The disorder in fluorapatite is often approximated by the so-called random-cluster model [72]. In the context of this model, the defects are assumed to be independent and their only effect is assumed to be the introduction of fluorine vacancies. These vacancies separate fluorine chains into clusters and the interaction between different clusters is neglected. Our simulations are based on this model. However, we do not neglect the interaction between clusters since the Hybrid Method allows to take it into account.

Let us consider some particular realization of disorder in the system. It can be specified by introducing a set of independent random binary variables $\{p_i\}$, which take value 0 with probability ρ and value 1 with probability $(1 - \rho)$. Here i is the index of the fluorine lattice site and ρ is the concentration of defects. The values $p_i = 1$ or $p_i = 0$ correspond to the spin being either present or absent on site i respectively. As a result, the terms \mathcal{H}'_{SS} and \mathcal{H}'_{SI} of the full truncated dipolar-dipolar Hamiltonian given by Eq. (1.44) become renormalized (see Section 1.2.4):

$$\mathcal{H}'_{SS} = \sum_{i < j} p_i p_j \frac{\gamma_F^2 (1 - 3 \cos^2 \theta_{ij})}{r_{ij}^3} \left[S_i^z S_j^z - \frac{1}{2} (S_i^x S_j^x + S_i^y S_j^y) \right], \quad (5.10)$$

$$\mathcal{H}'_{SI} = \sum_{i,k} p_i \frac{\gamma_P^2 (1 - 3 \cos^2 \theta_{ik})}{r_{ik}^3} S_i^z I_k^z, \quad (5.11)$$

where S_i^α are operators of ^{19}F spins and I_k^α are operators of ^{31}P spins. The definition of the auto-correlation function measured in experiment is also changed accordingly:

$$C_x(t) = \text{Tr} \left[e^{i\mathcal{H}'_{\text{dip}}t} \left(\sum_i p_i S_i^x \right) e^{-i\mathcal{H}'_{\text{dip}}t} \left(\sum_j p_j S_j^x \right) \right]. \quad (5.12)$$

Here we took into account that the operator of the total spin polarization acquires the form

$$\mathcal{M}_\alpha = \sum_i p_i S_i^\alpha. \quad (5.13)$$

Let us imagine dividing the sample into many pieces, which are macroscopic but still small in comparison to the sample size. In such a case, the contributions from the different pieces in Eq. (5.12) will be uncorrelated due to their macroscopic sizes, so that the full auto-correlation function reduces to the sum over auto-correlation functions of each of the pieces, which is, essentially, equivalent to disorder averaging. Henceforth, we replace Eq. (5.12) with its disorder average.

The disorder averaging restores the translational invariance of the system. It means, that, as in the case of no disorder, we can define $C_x(t)$ by correlating the contribution of some subset \mathcal{Q}' of lattice sites with the rest of the lattice (see Eq. (1.60) and the discussion preceding to it):

$$C_x(t) \equiv \frac{N}{N_{\mathcal{Q}'}} \cdot \left\langle \text{Tr} \left[e^{i\mathcal{H}'_{\text{dip}}t} \left(\sum_{i \in \mathcal{Q}'} p_i S_i^x \right) e^{-i\mathcal{H}'_{\text{dip}}t} \left(\sum_j p_j S_j^x \right) \right] \right\rangle_{\{p\}}, \quad (5.14)$$

where $\langle \dots \rangle_{\{p\}}$ denotes the disorder averaging.

The scheme of the hybrid simulations can be generalised to treat the disorder in the following manner. Assuming that there is no disorder at first, one needs to specify the full size of the lattice with periodic boundary conditions. Let us denote by \mathcal{L} the set of all lattice sites. Then one needs to choose the subset $\mathcal{Q} \in \mathcal{L}$ of lattice sites which serve as the quantum cluster. Correspondingly, the lattice sites of the subset $\mathcal{C} = \mathcal{L} \setminus \mathcal{Q}$ contain the spins of the classical environment. Additionally, one needs to specify the subset $\mathcal{Q}' \in \mathcal{Q}$ of central spins of the cluster, which we correlate with the rest of the lattice (see Eq. (3.15)). A realization of the disorder is generated by removing each of the spins from the system with probability ρ determined by the specified concentration of defects. Let $\mathcal{L}' \in \mathcal{L}$ denote the subset of the lattice sites with spins present. The resulting hybrid lattice is determined by the subsets $\mathcal{Q} \cap \mathcal{L}'$, $\mathcal{C} \cap \mathcal{L}'$ and $\mathcal{Q}' \cap \mathcal{L}'$. For each of the simulation runs, one generates a realization of disorder, samples the infinite temperature initial state of the resulting hybrid lattice, runs the simulation and calculates the unnormalized

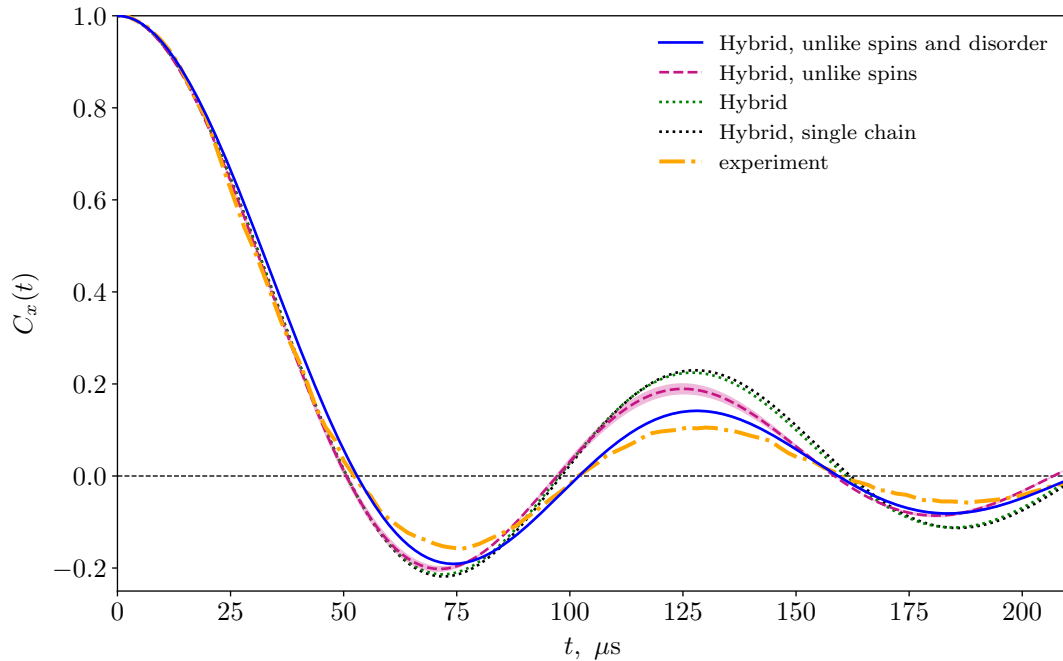


Figure 5.10: ^{19}F FID in fluorapatite. See the text for the explanation of the plot legend.

correlation function. The correlation function is then averaged over all the runs.

5.3.3 Results

The comparison of the results of our simulations with the experimental data of the paper [60] is presented in Fig. 5.10. We considered the simulations for a series of models, which are gradually getting more and more realistic:

- (I) single fluorine chain without any disorder or unlike spins;
- (II) three-dimensional fluorine sublattice without disorder and unlike spins;
- (III) full three-dimensional lattice with unlike spins, but no disorder
- (IV) full three-dimensional lattice with unlike spins and disorder

The details of the hybrid lattices used are the following. The fluorine sublattice can be defined as a lattice with single-site basis cell and the set of primitive vectors \mathbf{a} , \mathbf{b} and $\mathbf{c}/2$. The hybrid simulation for a single fluorine chain used a chain of length 201 with periodic boundary conditions; the size of the quantum cluster was 12. For the second model, the lattice with the size $7 \times 7 \times 13$ was used and the quantum cluster was chosen in the form of a single fluorine chain. For the last two models, which also contained unlike spins of phosphorus, we used the lattice characterized

by the original basis cell and set of primitive vectors described in Section 5.3.1. The size of the lattice was $9 \times 9 \times 7$ basis cells in both cases. The quantum cluster was again chosen as a single chain of fluorine spins. The concentration of defects ρ was estimated from the comparison of experimental and theoretical values of the second moment. This estimate gave $\rho = 0.077$.

The results of simulations of a single fluorine chain and multiple interacting fluorine chains nearly coincide with each other. This fact proves, that the usual approximation of the non-interacting chains is valid at least on the time-scales considered in the simulations.

Overall, the agreement between the most sophisticated model (IV) and the experimental data is satisfactory. However, there is still a noticeable discrepancy. This discrepancy is of the same order as the deviations between the results obtained for different models, which allows us to conclude that the results obtained for the model (IV) are within the experimental uncertainty associated with the insufficient information about the structure of the sample. Therefore, we believe that this discrepancy may be not due to some deficiency of the hybrid method, but rather it is an indicator of the fact that the model we simulated was not realistic enough.

In conclusion, we should note, that the results of our simulations should be considered as the predictions for future experiments with better control of the sample structure.

Chapter 6

Analysis of the Hybrid Method

6.1 Symmetry of the hybrid correlation functions

Similarly to the purely quantum and purely classical cases (see Section 2.6), it is convenient to study the two-spin correlation functions since other correlation functions of interest are constructed as the linear combinations of the former ones. For a hybrid lattice, we can define them as

$$\mathfrak{C}_{i,j}^{\alpha,\beta}(t) = \left[\mathfrak{M}_i^\alpha(t) \mathfrak{M}_j^\beta(0) \right]_{i.c.}, \quad (6.1)$$

where either

$$\mathfrak{M}_i^\alpha(t) = \sqrt{D_{\mathcal{Q}} + 1} \cdot \langle \psi(t) | S_i^\alpha | \psi(t) \rangle = \sqrt{D_{\mathcal{Q}} + 1} \cdot \langle \psi | S_i^\alpha(t) | \psi \rangle, \quad \text{if } i \in \mathcal{Q}, \quad (6.2)$$

or

$$\mathfrak{M}_i^\alpha(t) = s_m^\alpha(t), \quad \text{if } i \in \mathcal{C}. \quad (6.3)$$

Here we prove that these functions are even functions of time.

In this section, it is convenient to describe the state of the quantum cluster in Schrödinger representation and use the system of Eqs. (3.9), (3.6) to define the dynamics. The hybrid lattice is still time-reversal invariant: if $\{|\psi(t)\rangle, s_m^\alpha(t)\}$ is the solution of the system (3.9), (3.6), then its time-reversal partner $\{\Theta|\psi(-t)\rangle, -s_m^\alpha(-t)\}$ is also a solution. In order to show it, let us write explicitly

$$\begin{aligned} |\psi(t)\rangle &= \mathcal{U}_t \{s_m^\alpha(\tau)\} |\psi\rangle = \mathcal{T} \exp \left[-i \int_0^t dt' \mathcal{H}_{\mathcal{Q}}(t') \right] |\psi\rangle = \\ &= \mathcal{T} \exp \left[-i \int_0^t dt' \left(\sum_{i < j, \alpha}^{i,j \in \mathcal{Q}} J_{i,j}^\alpha S_i^\alpha S_j^\alpha - \sum_{i \in \mathcal{Q}} \mathbf{h}_i^{\mathcal{C}\mathcal{Q}}(t') \cdot \mathbf{S}_i \right) \right] |\psi\rangle, \quad (6.4) \end{aligned}$$

and

$$|\psi(-t)\rangle = \mathcal{U}_{-t} \{s_m^\alpha(\tau)\} |\psi\rangle = \mathcal{T} \exp \left[i \int_0^t dt' \mathcal{H}_Q(-t') \right] |\psi\rangle, \quad (6.5)$$

where \mathcal{T} is the time-ordering operator applied to the values of t' . Now, we can do the following exact manipulations:

$$\begin{aligned} |\tilde{\psi}(t)\rangle &\equiv \Theta |\psi(-t)\rangle = \\ &= \Theta \mathcal{U}_{-t} \{s_m^\alpha(\tau)\} \Theta^{-1} \Theta |\psi\rangle = \mathcal{T} \exp \left[-i \int_0^t dt' \Theta \mathcal{H}_Q(-t') \Theta^{-1} \right] |\psi\rangle = \\ &= \mathcal{T} \exp \left[-i \int_0^t dt' \left(\sum_{i < j, \alpha}^{i, j \in \mathcal{Q}} J_{i, j}^\alpha S_i^\alpha S_j^\alpha - \sum_{i \in \mathcal{Q}} (-\mathbf{h}_i^{\mathcal{C}\mathcal{Q}}(-t')) \cdot \mathbf{S}_i \right) \right] \Theta |\psi\rangle = \\ &= \mathcal{U}_t \{-s_m^\alpha(-\tau)\} \Theta |\psi\rangle. \end{aligned} \quad (6.6)$$

At the same time, since $\Theta S_i^\alpha \Theta^{-1} = -S_i^\alpha$, we get with the use of identity (2.44):

$$\langle \tilde{\psi}(t) | S_i^\alpha | \tilde{\psi}(t) \rangle = -\langle \tilde{\psi}(-t) | \Theta S_i^\alpha \Theta^{-1} | \tilde{\psi}(-t) \rangle = -\langle \psi(-t) | S_i^\alpha | \psi(-t) \rangle. \quad (6.7)$$

If we substitute Eq.(6.7) together with $\{-s_m^\alpha(-t)\}$ into Eq. (3.6) for classical spins, we will find that Eq. (3.6) is satisfied too.

As we see, if the solution $\{|\psi(t)\rangle, s_m^\alpha(t)\}$ corresponds to initial conditions $\{|\psi\rangle, x_m^\alpha\}$, then its time-reversal partner corresponds to initial conditions $\{\Theta|\psi\rangle, -x_m^\alpha\}$. For the former trajectory, we can track the projections of different spins:

$$\sqrt{D_Q + 1} \langle \psi | S_i^\alpha(t) | \psi \rangle \quad \text{and} \quad s_m^\alpha(t). \quad (6.8)$$

The strategy of our proof is the same as for the purely quantum and purely classical cases (see Section 2.6). First, we show, that if we traverse the partner trajectory backwards in time, we observe the same projections of spins but with a negative sign. Then we use the invariance of the distribution of the initial conditions with respect to the time-reversal.

For the classical part of the system we can immediately write

$$-s_m^\alpha(-t) \Big|_{s_m^\alpha(0)=-x_m^\alpha}^{|\psi(0)\rangle=\Theta|\psi\rangle} = s_m^\alpha(t) \Big|_{s_m^\alpha(0)=x_m^\alpha}^{|\psi(0)\rangle=|\psi\rangle} \quad (6.9)$$

The analogous identity for the projections of quantum spins follows from Eq. (6.7):

$$\begin{aligned} \langle \Theta\psi | S_i^\alpha(t) | \Theta\psi \rangle |_{s_m^\alpha(0)=-x_m^\alpha} &\equiv \langle \tilde{\psi}(t) | S_i^\alpha | \tilde{\psi}(t) \rangle = \\ &= -\langle \psi(-t) | S_i^\alpha | \psi(-t) \rangle \equiv -\langle \psi | S_i^\alpha(-t) | \psi \rangle |_{s_m^\alpha(0)=x_m^\alpha}, \end{aligned} \quad (6.10)$$

or, equivalently,

$$\langle \Theta\psi | -S_i^\alpha(-t) | \Theta\psi \rangle |_{s_m^\alpha(0)=-x_m^\alpha} = \langle \psi | S_i^\alpha(t) | \psi \rangle |_{s_m^\alpha(0)=x_m^\alpha}. \quad (6.11)$$

Now we can substitute Eqs. (6.9) and (6.11) into Eqs. (6.1), (6.2) and (6.3):

$$\begin{aligned} \left[\mathfrak{M}_i^\alpha(t) \mathfrak{M}_j^\beta(0) \right]_{i.c.} &\equiv \left[\mathfrak{M}_i^\alpha(t) |_{s_m^\alpha(0)=x_m^\alpha}^{|\psi(0)\rangle=|\psi\rangle} \mathfrak{M}_j^\beta(0) |_{s_m^\alpha(0)=x_m^\alpha}^{|\psi(0)\rangle=|\psi\rangle} \right]_{x_m^\alpha}^{|\psi\rangle} = \\ &= \left[(-\mathfrak{M}_i^\alpha(-t)) |_{s_m^\alpha(0)=-x_m^\alpha}^{|\psi(0)\rangle=\Theta|\psi\rangle} (-\mathfrak{M}_j^\beta(0)) |_{s_m^\alpha(0)=-x_m^\alpha}^{|\psi(0)\rangle=\Theta|\psi\rangle} \right]_{x_m^\alpha}^{|\psi\rangle} = \\ &= \left[\mathfrak{M}_i^\alpha(-t) |_{s_m^\alpha(0)=-x_m^\alpha}^{|\psi(0)\rangle=\Theta|\psi\rangle} \mathfrak{M}_j^\beta(0) |_{s_m^\alpha(0)=-x_m^\alpha}^{|\psi(0)\rangle=\Theta|\psi\rangle} \right]_{x_m^\alpha}^{|\psi\rangle}. \end{aligned} \quad (6.12)$$

The transformation $\{|\psi\rangle, x_i^\alpha\} \rightarrow \{\Theta|\psi\rangle, -x_m^\alpha\}$ and its inverse leave the distribution of initial conditions invariant. As a consequence, in Eq. (6.12),

$$\begin{aligned} \left[\mathfrak{M}_i^\alpha(-t) |_{s_m^\alpha(0)=-x_m^\alpha}^{|\psi(0)\rangle=\Theta|\psi\rangle} \mathfrak{M}_j^\beta(0) |_{s_m^\alpha(0)=-x_m^\alpha}^{|\psi(0)\rangle=\Theta|\psi\rangle} \right]_{x_m^\alpha}^{|\psi\rangle} &= \\ = \left[\mathfrak{M}_i^\alpha(-t) |_{s_m^\alpha(0)=x_m^\alpha}^{|\psi(0)\rangle=|\psi\rangle} \mathfrak{M}_j^\beta(0) |_{s_m^\alpha(0)=x_m^\alpha}^{|\psi(0)\rangle=|\psi\rangle} \right]_{x_m^\alpha}^{|\psi\rangle} &\equiv \left[\mathfrak{M}_i^\alpha(-t) \mathfrak{M}_j^\beta(0) \right]_{i.c.}. \end{aligned} \quad (6.13)$$

Combining Eqs. (6.12) and (6.13) together, we, finally, prove that

$$\mathfrak{C}_{i,j}^{\alpha,\beta}(t) = \mathfrak{C}_{i,j}^{\alpha,\beta}(-t). \quad (6.14)$$

6.2 Moment expansion

In this section, we extend the treatment of the Taylor expansions of the classical and quantum correlation functions by Lundin and Zobov [59] to the case of the hybrid lattice.

Let us consider a quantum, a classical and a hybrid lattices which correspond to each other. By correspondence I mean the following: The equations (3.1), (3.2) uniquely define the hybrid lattice corresponding to the original quantum lattice provided we fix the choice of the quantum cluster. Analogously, if we choose the quantum cluster to consist of no spins at all, then the same equations uniquely define the corresponding classical lattice. These corresponding to each other lattices have the same full size.

We can analyze the agreement between the two-spin correlation functions $C_{i,j}^{\alpha,\beta}(t)$, $c_{i,j}^{\alpha,\beta}(t)$ and $\mathfrak{C}_{i,j}^{\alpha,\beta}(t)$ given by Eqs. (2.40), (2.49) and (6.1) respectively in all three cases by comparing their Taylor expansions at $t = 0$. In this regard, we should note that since these are even functions of time (see Sections 2.6 and 6.1), the odd terms vanish, and we need to compare only the even terms in the expansions. Additionally, we should restrict ourselves only to the correlation functions with $\alpha = \beta$. It follows from the special form of the original quantum Hamiltonian (1.52) where only the spin projections on the same axis have non-zero correlations. If $\alpha \neq \beta$, then we can rotate all the spins by π around α -axis. This procedure leaves the distribution of initial states unchanged in all three cases so that we expect that such a transformation leaves the correlation functions unchanged too. At the same time, the Hamiltonians stay invariant, but β spin projections change the sign, which allows us to conclude that the correlation functions should also change sign. The only possibility the two arguments can coexist is for this correlation functions with $\alpha \neq \beta$ to be equal to zero.

In the following discussion, it is also convenient to fix the index i in Eqs. (2.40), (2.49) and (6.1) in such a way that it corresponds to one of the central spins of the quantum cluster in the hybrid case. Only such two-spin correlation functions contribute to the hybrid correlation function (3.15). With this choice of the index i we can explicitly express the hybrid two-spin correlation function as

$$\mathfrak{C}_{i,j}^{\alpha,\alpha}(t) = \left\{ \sqrt{D_{\mathcal{Q}} + 1} \langle \psi | S_i^{\alpha}(t) | \psi \rangle \cdot \mathfrak{M}_j^{\alpha}(0) \right\}. \quad (6.15)$$

6.2.1 Taylor expansion in the quantum and the classical cases

The coefficient C_{2n} of the Taylor series of $C_{i,j}^{\alpha,\alpha}(t)$ is defined as:

$$C_{2n} = \left. \frac{d^{2n} C_{i,j}^{\alpha,\alpha}(t)}{dt^{2n}} \right|_{t=0} = \underbrace{\langle [i\mathcal{H}, [i\mathcal{H}, \dots, [i\mathcal{H}, S_i^{\alpha}] \dots]]}_{2n \text{ times}} S_j^{\alpha} \rangle. \quad (6.16)$$

At each level of the nested commutators, the Hamiltonian is commuted with an expression containing a linear combination of products of spin operators. The commutation of Hamiltonian with the product of spin operators produces a number of terms where the Hamiltonian is commuted with each of the spin operators in the product (it works like Leibniz rule for differentiation):

$$\begin{aligned} [i\mathcal{H}, S_{i_1}^{\alpha_1} S_{i_2}^{\alpha_2} \dots S_{i_l}^{\alpha_l}] &= \\ &= [i\mathcal{H}, S_{i_1}^{\alpha_1}] S_{i_2}^{\alpha_2} \dots S_{i_l}^{\alpha_l} + S_{i_1}^{\alpha_1} [i\mathcal{H}, S_{i_2}^{\alpha_2}] \dots S_{i_l}^{\alpha_l} + \dots + S_{i_1}^{\alpha_1} S_{i_2}^{\alpha_2} \dots [i\mathcal{H}, S_{i_l}^{\alpha_l}]. \end{aligned} \quad (6.17)$$

Overall, we can formulate the process of taking $2n$ commutators as an iterative procedure with the help of Eq. (1.54):

$$[i\mathcal{H}, S_k^\alpha] = - \sum_{l \neq k, \beta, \gamma} J_{k,l}^\gamma \varepsilon^{\alpha, \beta, \gamma} S_k^\beta S_l^\gamma. \quad (6.18)$$

At each step of the procedure we pick a spin operator S_k^α to “differentiate” and particular component of the local magnetic field produced by the spin operator S_l^γ as the source of “differentiation”. After we walk through all of the $2n$ steps, we can perform the summation over the different choices of the spin projection to differentiate and different choices of the source of the differentiation. The expression we obtain this way is

$$C_{2n} = \sum_{i_1, \alpha_1} \sum_{i_2, \alpha_2} \dots \sum_{i_{2n+1}, \alpha_{2n+1}} K(i_1, \alpha_1; i_2, \alpha_2; \dots; i_{2n+1}, \alpha_{2n+1}) \langle S_{i_1}^{\alpha_1} S_{i_2}^{\alpha_2} \dots S_{i_{2n+1}}^{\alpha_{2n+1}} S_j^\alpha \rangle, \quad (6.19)$$

where the factors $K(i_1, \alpha_1; i_2, \alpha_2; \dots; i_{2n}, \alpha_{2n})$ are made of the coupling constants, Levi-Civita symbols and factors -1 .

We can repeat the same steps for the corresponding purely classical lattice. Since the Eq. (1.70) governing the differentiation in this case is algebraically identical to Eq. (1.54) governing differentiation in the quantum case, for the coefficient c_{2n} of the Taylor series of $c_{i,j}^{\alpha,\alpha}(t)$, we get

$$\begin{aligned} c_{2n} &= \left. \frac{d^{2n} c_{i,j}^{\alpha,\alpha}(t)}{dt^{2n}} \right|_{t=0} = \\ &= \sum_{i_1, \alpha_1} \sum_{i_2, \alpha_2} \dots \sum_{i_{2n+1}, \alpha_{2n+1}} K(i_1, \alpha_1; i_2, \alpha_2; \dots; i_{2n+1}, \alpha_{2n+1}) \left[S_{i_1}^{\alpha_1} S_{i_2}^{\alpha_2} \dots S_{i_{2n+1}}^{\alpha_{2n+1}} S_j^\alpha \right]_{i.c.}, \end{aligned} \quad (6.20)$$

Note that due to the mentioned algebraic similarity, the factors $K(i_1, \alpha_1; i_2, \alpha_2; \dots; i_{2n}, \alpha_{2n})$ are the same as in the corresponding quantum expression.

Both the quantum average $\langle \dots \rangle$ and the classical average over initial conditions $[\dots]_{i.c.}$ in Eqs. (6.19) and (6.20) respectively decouple into product of averages over each of the lattice sites. In order to clarify this point, let us first consider a quantum average $\langle \mathcal{O}_{i_1} \mathcal{O}_{i_2} \dots \mathcal{O}_{i_n} \rangle$, where \mathcal{O}_{i_r} is a product of spin operators on lattice site i_r . The Hilbert space of the lattice is the tensor product of the Hilbert spaces of each of the lattice sites. As a consequence, we can reexpress the trace $\text{Tr}[\dots]$ over the Hilbert space of the lattice in terms of the traces $\text{Tr}_i[\dots]$ over

the Hilbert spaces of each of the lattice sites:

$$\begin{aligned}
 \langle \mathcal{O}_{i_1} \mathcal{O}_{i_2} \dots \mathcal{O}_{i_n} \rangle &= \frac{\text{Tr} [\mathcal{O}_{i_1} \mathcal{O}_{i_2} \dots \mathcal{O}_{i_n}]}{(2S+1)^N} = \\
 &= \frac{\text{Tr}_{i_1} [\mathcal{O}_{i_1}] \cdot \text{Tr}_{i_2} [\mathcal{O}_{i_2}] \cdot \dots \cdot \text{Tr}_{i_n} [\mathcal{O}_{i_n}] \cdot \text{Tr}_{\mathcal{L}/i_1, i_2, \dots, i_n} [\mathbb{1}]}{(2S+1)^N} = \\
 &= \frac{\text{Tr}_{i_1} [\mathcal{O}_1]}{2S+1} \cdot \frac{\text{Tr}_{i_2} [\mathcal{O}_2]}{2S+1} \cdot \dots \cdot \frac{\text{Tr}_{i_n} [\mathcal{O}_n]}{2S+1} \equiv \langle \mathcal{O}_1 \rangle_{i_1} \cdot \langle \mathcal{O}_2 \rangle_{i_2} \cdot \dots \cdot \langle \mathcal{O}_n \rangle_{i_n}. \quad (6.21)
 \end{aligned}$$

Here $\text{Tr}_{\mathcal{L}/i_1, i_2, \dots, i_n} [\dots]$ is the trace over the lattice sites with no spin operators, and we took into account that $\text{Tr}_{\mathcal{L}/i_1, i_2, \dots, i_n} [\mathbb{1}] = (2S+1)^{N-n}$. By analogy, we can consider the corresponding classical average $[O_{i_1} O_{i_2} \dots O_{i_n}]_{i.c.}$, where O_{i_r} is a product of classical spin projections on lattice site i_r . Since the distributions of initial conditions for each of the classical spins are uncorrelated, the averages over each of the spins can be performed independently:

$$[O_{i_1} O_{i_2} \dots O_{i_n}]_{i.c.} = [O_{i_1}]_{i.c.}^{i_1} \cdot [O_{i_2}]_{i.c.}^{i_2} \cdot \dots \cdot [O_{i_n}]_{i.c.}^{i_n}. \quad (6.22)$$

In the classical case, the average over the lattice site can be non-zero only if each of the spin projections is encountered an even number of times in expression (6.20). In the quantum case, certain combinations of odd powers of spin projection operators can average to a non-zero value. Still, we need at least two operators on the same lattice site for the average to be possibly non-zero. So the number of independent summations in Eqs. (6.19) and (6.20) is at most n .

Lundin and Zobov [59] noticed that there is an important class of non-zero terms in Eqs. (6.19) and (6.20) which coincide in the quantum and the classical case. This class is comprised of the terms which have precisely two identical spin projections on each of the lattice sites encountered in the product of spin variables at the right-hand sides of Eqs. (6.19) and (6.20) (it corresponds to the maximal possible number of independent summations in a non-zero term). When we re-express the average of the combination of spin projections as the product of averages over each of the lattice sites, for the lattice site i encountered in the combination the corresponding average over the Hilbert space of this site $\langle \dots \rangle_i$ in the quantum case takes the form

$$\langle S_i^\alpha S_i^\alpha \rangle_i = \frac{\text{Tr} [S_i^\alpha S_i^\alpha]}{(2S+1)} = \frac{\text{Tr} \left[\sum_{\alpha'} S_i^{\alpha'} S_i^{\alpha'} \right]}{3(2S+1)} = \frac{\text{Tr} [S(S+1)]}{3(2S+1)} = \frac{S(S+1)}{3}. \quad (6.23)$$

Analogously, in the classical case, the same average over the lattice site i takes

the form:

$$[s_i^\alpha s_i^\alpha]_{i.c.}^i = \frac{1}{3} \left[\sum_{\alpha'} s_i^{\alpha'} s_i^{\alpha'} \right]_{i.c.}^i = \frac{S(S+1)}{3}. \quad (6.24)$$

As we see, the result is the same as in the quantum case (6.23). As a consequence, the terms of (6.19) and (6.20) which are decoupled into averages of this form have the same value both in the classical and the quantum case.

When the effective number of interacting neighbours n_{eff} (see Eq. (1.73)) is very large, the probability to have more than two spin projections on the same lattice sites becomes low, so that the sums in Eqs. (6.19) and (6.20) are dominated by the terms which coincide in the quantum and the classical cases.

6.2.2 Taylor expansion in the hybrid case

These considerations can be extended to the case of the hybrid lattice in a similar manner. Similarly to the quantum and the classical cases, we define the coefficient \mathfrak{C}_{2n} of the Taylor expansion of the hybrid correlation function $\mathfrak{C}_{i,j}^t$:

$$\mathfrak{C}_{2n} = \left. \frac{d^{2n} \mathfrak{C}_{i,j}^{\alpha,\alpha}(t)}{dt^{2n}} \right|_{t=0}. \quad (6.25)$$

Again, Eqs. (3.5) and (3.6) governing the differentiation in this case have the same algebraical structure as Eqs. (1.54) and (1.70) in the quantum and the classical cases respectively. As a result, for the coefficient \mathfrak{C}_{2n} , we get an expression similar in structure to Eqs. (6.19) and (6.20) and with the same factors $K(\dots)$. The main difference is in the structure of the average of the spin projections combination. For the hybrid lattice, it contains both classical spin projections and quantum spin projection operators grouped into several quantum expectation values.

To illustrate the point, let us look at an example of a term appearing in \mathfrak{C}_4 . Suppose we consider the calculation of expansion of

$$\mathfrak{C}_{i,j}^{x,x}(t) = \left[\sqrt{D_{\mathcal{Q}} + 1} \langle \psi | S_i^x(t) | \psi \rangle \sqrt{D_{\mathcal{Q}} + 1} \langle \psi | S_j^x | \psi \rangle \right]_{i.c.}, \quad \text{for } j \in \mathcal{Q} \quad (6.26)$$

We can consider the following sequence of four “differentiations” of $\sqrt{D_{\mathcal{Q}} + 1} \cdot \langle \psi | S_i^x(t) | \psi \rangle$:

- “differentiate” by $-J_{i,j}^z S_j^z(t)$ for $j \in \mathcal{Q}$:

$$\sqrt{D_{\mathcal{Q}} + 1} \langle \psi | S_i^x(t) | \psi \rangle \longrightarrow -J_{i,j}^z \varepsilon^{x,y,z} \sqrt{D_{\mathcal{Q}} + 1} \langle \psi | S_i^y(t) S_j^z(t) | \psi \rangle. \quad (6.27)$$

- “differentiate” $S_j^z(t)$ by $-J_{j,k}^x s_k^x(t)$ for $k \in \mathcal{C}$:

$$\begin{aligned} & -J_{i,j}^z \varepsilon^{x,y,z} \sqrt{D_{\mathcal{Q}} + 1} \langle \psi | S_i^y(t) S_j^z(t) | \psi \rangle \longrightarrow \\ & \longrightarrow (-1)^2 J_{i,j}^z \varepsilon^{x,y,z} J_{j,k}^x \varepsilon^{z,y,x} \sqrt{D_{\mathcal{Q}} + 1} \langle \psi | S_i^y(t) S_j^y(t) | \psi \rangle s_k^x(t). \end{aligned} \quad (6.28)$$

- “differentiate” $s_k^x(t)$ by $-J_{k,i}^y S_i^y(t)$:

$$\begin{aligned} & (-1)^2 J_{i,j}^z \varepsilon^{x,y,z} J_{j,k}^x \varepsilon^{z,y,x} \sqrt{D_{\mathcal{Q}} + 1} \langle \psi | S_i^y(t) S_j^y(t) | \psi \rangle s_k^x(t) \longrightarrow \\ & \longrightarrow (-1)^3 J_{i,j}^z \varepsilon^{x,y,z} J_{j,k}^x \varepsilon^{z,y,x} J_{k,i}^y \varepsilon^{x,z,y} \cdot \\ & \cdot \sqrt{D_{\mathcal{Q}} + 1} \langle \psi | S_i^y(t) S_j^y(t) | \psi \rangle s_k^z(t) \sqrt{D_{\mathcal{Q}} + 1} \langle \psi | S_i^y(t) | \psi \rangle. \end{aligned} \quad (6.29)$$

- “differentiate” $S_j^y(t)$ by $-J_{j,k}^z s_k^z(t)$:

$$\begin{aligned} & (-1)^3 J_{i,j}^z \varepsilon^{x,y,z} J_{j,k}^x \varepsilon^{z,y,x} J_{k,i}^y \varepsilon^{x,z,y} \cdot \\ & \cdot \sqrt{D_{\mathcal{Q}} + 1} \langle \psi | S_i^y(t) S_j^y(t) | \psi \rangle s_k^z(t) \sqrt{D_{\mathcal{Q}} + 1} \langle \psi | S_i^y(t) | \psi \rangle \longrightarrow \\ & \longrightarrow (-1)^4 J_{i,j}^z \varepsilon^{x,y,z} J_{j,k}^x \varepsilon^{z,y,x} J_{k,i}^y \varepsilon^{x,z,y} J_{j,k}^z \varepsilon^{y,x,z} \cdot \\ & \cdot \sqrt{D_{\mathcal{Q}} + 1} \langle \psi | S_i^y(t) S_j^x(t) | \psi \rangle s_k^z(t) s_k^z(t) \sqrt{D_{\mathcal{Q}} + 1} \langle \psi | S_i^y(t) | \psi \rangle. \end{aligned} \quad (6.30)$$

The corresponding term in \mathfrak{C}_4 has the form

$$\begin{aligned} & (-1)^4 J_{i,j}^z \varepsilon^{x,y,z} J_{j,k}^x \varepsilon^{z,y,x} J_{k,i}^y \varepsilon^{x,z,y} J_{j,k}^z \cdot \\ & \cdot \left[\sqrt{D_{\mathcal{Q}} + 1} \langle \psi | S_i^y S_j^x | \psi \rangle \sqrt{D_{\mathcal{Q}} + 1} \langle \psi | S_i^y | \psi \rangle \sqrt{D_{\mathcal{Q}} + 1} \langle \psi | S_j^x | \psi \rangle \right]_{\psi} [s_k^z s_k^z]_{i.c.} \end{aligned} \quad (6.31)$$

Notice that when we “differentiate” a quantum spin operator by another quantum spin operator, the latter one is multiplied inside the same quantum expectation value. When we “differentiate” a classical spin by a quantum spin operator, we get another quantum expectation value with its accompanying factor $\sqrt{D_{\mathcal{Q}} + 1}$.

Finally, the cluster part $[\dots]_{\psi}$ of the average over initial conditions can be evaluated with the help of Eqs. (2.4), (2.5), (2.7) and (2.39).

6.2.3 Analysis of the expansion in the hybrid case

The detailed analysis of the terms arising in the hybrid case is complicated by the nontrivial structure of the averages of several quantum expectation values.

If we compare analogous terms in the hybrid expansion and in the classical expansion, the averages over the lattice sites of the classical environment are identical in both cases. Yet, we can expect an improvement in the hybrid case if the averages over the lattice sites inside the quantum cluster are the same as in the

purely quantum case.

In this regard, we can expect an improvement in the two following cases:

(I) The average of the cluster part takes the form

$$\left[\sqrt{D_{\mathcal{Q}} + 1} \langle \psi | \mathcal{A} | \psi \rangle \sqrt{D_{\mathcal{Q}} + 1} \langle \psi | \mathcal{B} | \psi \rangle \right]_{\psi}, \quad (6.32)$$

where $\text{Tr} [\mathcal{A}] = \text{Tr} [\mathcal{B}] = 0$. Then,

$$\left[\sqrt{D_{\mathcal{Q}} + 1} \langle \psi | \mathcal{A} | \psi \rangle \sqrt{D_{\mathcal{Q}} + 1} \langle \psi | \mathcal{B} | \psi \rangle \right]_{\psi} = \frac{(D_{\mathcal{Q}} + 1) \text{Tr} [\mathcal{A}\mathcal{B}]}{D_{\mathcal{Q}}(D_{\mathcal{Q}} + 1)} = \langle \mathcal{A}\mathcal{B} \rangle. \quad (6.33)$$

(II) The average of the cluster part takes the form

$$(D_{\mathcal{Q}} + 1)^p [\langle \psi | \mathcal{A}_1 | \psi \rangle \langle \psi | \mathcal{B}_1 | \psi \rangle \langle \psi | \mathcal{A}_2 | \psi \rangle \langle \psi | \mathcal{B}_2 | \psi \rangle \dots \langle \psi | \mathcal{A}_p | \psi \rangle \langle \psi | \mathcal{B}_p | \psi \rangle]_{\psi}, \quad (6.34)$$

where $\text{Tr} [\mathcal{A}_1] = \text{Tr} [\mathcal{B}_1] = \dots = \text{Tr} [\mathcal{A}_p] = \text{Tr} [\mathcal{B}_p] = 0$, but $\text{Tr} [\mathcal{A}_r \mathcal{B}_r] \neq 0$ for $1 \leq r \leq p$. Additionally, we assume that $2p \ll D$ and there is no other way to pair up operators so that we get non-zero traces. Notice that the former condition is not really a strong constraint because the Hilbert space dimensionality grows exponentially with the size of the cluster.

When we take the average in Eq. (6.34), we need to sum over all the splittings of the operators \mathcal{A}_r and \mathcal{B}_r between different traces. The largest contribution comes from the term with the maximal number of traces, because each of the traces acts as an additional factor of $D_{\mathcal{Q}}$ (all the other terms are smaller by the factor of at least $1/D_{\mathcal{Q}}$)¹. Due to the restrictions we imposed, such a term would have each \mathcal{A}_r paired with \mathcal{B}_r inside the trace. As a result, we can write Eq. (6.34) approximately as²

$$\begin{aligned} & \frac{(D_{\mathcal{Q}} + 1)^p \Gamma(D_{\mathcal{Q}})}{\Gamma(D_{\mathcal{Q}} + 2p)} \text{Tr} [\mathcal{A}_1 \mathcal{B}_1] \text{Tr} [\mathcal{A}_2 \mathcal{B}_2] \dots \text{Tr} [\mathcal{A}_p \mathcal{B}_p] = \\ & = \frac{(D_{\mathcal{Q}} + 1)^p \Gamma(D_{\mathcal{Q}})}{\Gamma(D_{\mathcal{Q}} + 2p)} D_{\mathcal{Q}}^{p-1} \text{Tr} [\mathcal{A}_1 \mathcal{B}_1 \mathcal{A}_2 \mathcal{B}_2 \dots \mathcal{A}_p \mathcal{B}_p] \simeq \\ & \simeq \frac{D_{\mathcal{Q}}^{2p-1}}{D_{\mathcal{Q}}^{2p}} \text{Tr} [\mathcal{A}_1 \mathcal{B}_1 \mathcal{A}_2 \mathcal{B}_2 \dots \mathcal{A}_p \mathcal{B}_p] = \langle \mathcal{A}_1 \mathcal{B}_1 \mathcal{A}_2 \mathcal{B}_2 \dots \mathcal{A}_p \mathcal{B}_p \rangle. \end{aligned} \quad (6.35)$$

¹For spins $1/2$, if we decompose the trace into traces over the Hilbert spaces of each of the lattice sites, the only way we can get a non-zero value is if the product of spin operators on each of the sites is proportional to the unit operator. Now, if we have a non-zero product of traces, we can reexpress it as one single trace, but each additional trace would give us a factor of $D_{\mathcal{Q}}$

²In some sense, the case (I) seems to coincide with the case (II). However, the equivalency to the quantum average is exact in the former case, but approximate in the latter one.

The first type of the cluster average can be encountered, for example, in the expansion of $\mathfrak{C}_{i,j}^{\alpha,\alpha}(t)$ for $j \in \mathcal{Q}$ (see Eq. (6.26)). If in the course of the differentiation of $\sqrt{D_{\mathcal{Q}} + 1} \langle \psi | S_i^x(t) | \psi \rangle$ we never leave the quantum cluster or never go back to the cluster after we left it, then the obtained term has the cluster average precisely of the form (6.32). In the case where n_{eff} is small, a central spin in the quantum cluster will be largely correlated with its closest neighbours. At the same time, it is plausible that in the expansions of the corresponding two-spin correlation functions the terms with the cluster average of the form (6.32) would play an important role. Overall, we expect, that the hybrid auto-correlation function (3.15) is a good approximation to the quantum one in the case of n_{eff} being small.

The cluster averages of the form (6.34) naturally arise for the lattices with very large n_{eff} . As we discussed, in this case, the expansions of the correlation functions are dominated by the terms where we have only two spin variables on the same lattice site. Let us consider an iterative procedure for one such a term. Since n_{eff} is very large, we also expect that when we differentiate a quantum spin operator, there would be a high probability that the source of the differentiation is a classical spin. As a result, there would be a low probability to have more than one operator in the same quantum expectation value, i.e. a cluster average part for a typical term would have single spin operators in each of the quantum expectation values. Combined with the fact that there are only two operators per lattice site, we get that a probable cluster average would be of the form (6.34). Since the classical part of the average is also correct in this case, we expect that the hybrid correlation functions should converge to the quantum ones in the limit when $n_{\text{eff}} \rightarrow +\infty$.

Since the Hybrid Method performs well in the two limiting cases n_{eff} is small and n_{eff} is very large, it is plausible to expect that it also performs well for the intermediate values of n_{eff} .

We should also note that although the Taylor expansions for the hybrid and the quantum two-spin correlation functions are not exactly the same, their zero- and second-order coefficients do coincide.

Chapter 7

Conclusions and outlook

7.1 Conclusions

In this thesis, we developed a method for simulating high-temperature spin dynamics, which we applied to the problem of first-principles calculation of FID in solids. It is a long-standing problem, whose conclusive solution is hindered by the absence of the clear separation of time scales on the analytical side, and by the exponential growth of the computing resources with the size of the system on the numerical side.

The method we proposed is based on approximating the dynamics of a fully quantum spin lattice by the dynamics of a hybrid spin lattice, consisting of a cluster of the quantum spins surrounded by an environment of the classical spins.

In order to test its validity, we performed tests for spin lattices of various dimensions and with various interaction constants. In total, we computed FIDs for 20 different cases. In almost all considered cases, an excellent performance of the hybrid method has been observed. To the best of our knowledge, our method is the most extensively tested one in comparison with other methods developed for the same problem.

As a part of the tests, we computed the FIDs for real materials. Moreover, we went beyond the case of CaF_2 and gave FID predictions for isotopically enriched ^{29}Si silicon and for calcium fluorapatite $\text{Ca}_{10}(\text{PO}_4)_6\text{F}_2$. Also, on the example of fluorapatite, we demonstrated how to treat unlike spins and disorder in the context of our method.

The important feature of the method is that it allows to estimate the uncertainty of its predictions: the comparison of the results of simulations for different sizes of quantum clusters allows us to determine the time range where the simulation results are reliable. Additionally, in the case where the effective number of interacting neighbours is large, the same feature can be facilitated by comparing

the results of classical simulations with the results of hybrid ones.

7.2 Outlook

7.2.1 Possible extensions

The scheme of the hybrid simulations can be applied to the spin lattices with more general two-spin interactions than in Eq. (1.52). An example here is the full magnetic dipolar-dipolar interaction which controls the spin relaxation in the laboratory frame in the absence of external static field. Similarly, the method can be applied to a spin lattice in the presence of external inhomogeneous magnetic field. The effects of inhomogeneous chemical and Knight shifts can be taken into account this way.

Although we considered only spins-1/2 in the thesis, without any modifications, the Hybrid Method can be applied to the simulation of lattices consisting of large quantum spins. However, for nuclear spins larger than 1/2, one needs to take into account the coupling of the quadrupole moments of the nuclei to the local gradients of the electric field. It is conceptually not difficult to adapt the Hybrid Method to this case, but the presence of the quadrupole coupling complicate the description of the system. Yet, we should note that, for materials with a highly symmetric lattice structure, the positions of the nuclei coincide with the local extrema of the electrostatic potential, so that there are no electric gradients to couple to the quadrupole moments of nuclei. Therefore, for such materials, we can apply the Hybrid Method to large quantum spins without the need to account for the quadrupole coupling.

The Hybrid Method can be used to describe spin echoes [73],[2, Chapter 8]. The experimental setup in the case of spin echo is analogous to the experimental setup for FID measurements, however, it involves additional resonant pulse, which produces π rotation of spins around the transversal direction. This additional pulse is applied at time τ after the initial $\pi/2$ pulse, and the signal is detected at time τ after the second pulse. The spin echo envelope corresponds to the detected signal measured as a function of τ . In the context of the hybrid simulations, the π pulse corresponds to the flipping of both quantum and classical spins at time τ . In the similar manner, it is possible to treat other types of echoes.

The considerations of the thesis can be applied to the systems of localized electron spins in dielectrics or the mixed systems of interacting nuclear spins and electron spins. An example of the latter is a nitrogen-vacancy (NV) center in diamond. NV-centers came into the focus of very active research in recent two decades due to their record quantum coherence times at room temperature [74].

The Hybrid Method can be applied to describe the decoherence of the collective electron spin of the NV-center caused by the spins of ^{13}C nuclei and, possibly, by the electron spins localized on other defects.

Another possible extension is to modify the Hybrid Method to treat finite temperatures. Experimentally, the dynamics of electron spin lattices at finite temperatures is accessible by inelastic neutron scattering [75]. On the theoretical side, the interest in this regard is the following. Low-temperature dynamics is dominated by the ground state and the low-energy excitations. Essentially, at low temperatures, the system can be viewed as a gas of excitations. At the same time, the intermediate temperatures would correspond to a liquid-like dynamics, which is challenging to describe. Alternatively, we can consider a strongly disordered spin system. At intermediate temperatures, such a system would exhibit glassy dynamics. The extension of the Hybrid Method to finite temperatures would enable one to simulate the above dynamical regimes. Such an extension requires one to adjust two elements of hybrid simulations: the generation of initial conditions and the way the hybrid correlation functions are defined.

7.2.2 Applications

The shape of NMR FID contains information about the coupling constants $J_{i,j}^\alpha$ describing the interactions between the spins. The same is true for spin echoes. Thus, the calculations afforded by the Hybrid Method can be used in order to accurately determine $J_{i,j}^\alpha$. The accurate knowledge of $J_{i,j}^\alpha$ can, in turn, be exploited as follows.

If we can neglect the transferred hyperfine coupling, then $J_{i,j}^\alpha$ corresponds to the magnetic dipolar-dipolar interaction. In this case, $J_{i,j}^\alpha$ provide information about the relative positions of nuclei. Thus, the FID and spin echo measurements can help one to determine the chemical structure of materials. An example of such an application can be found in paper [76]. There, NMR spin echo was used to determine the distance between two carbon nuclei in acetylene C_2H_2 adsorbed on the platinum catalyst.

In metals, there is a significant contribution to $J_{i,j}^\alpha$ due to the transferred hyperfine coupling. This coupling is sensitive to the spin susceptibility of the conduction electrons, which is the property important for the characterization of various magnetic and superconducting materials. Thus, NMR FID and echoes can be used to probe electronic spin susceptibility, which, for example, has been done for high-temperature cuprate superconductors [77, 78].

Appendix A

Details of simulations

A.1 The setup of the simulation schemes

A.1.1 Quantum simulations

The reference simulations of Chapter 4, performed for fully quantum lattices, used the method of two wave functions propagation introduced by Elsayed and Fine [37], which we described in Section 1.4.2 (see Eqs. (1.77), (1.78) and (1.79)).

The typical initial wave function was sampled from the infinite-temperature distribution by the scheme described in Section 2.1 (see Eqs. (2.2), (2.3) and the corresponding discussion).

A.1.2 Classical simulations

For the simulations of purely classical lattices in Chapters 4 and 5, we integrated the equations of motion (1.70), (1.71). The initial spin vectors $\{\mathbf{s}_m(0)\}$ were generated as radius-vectors of points randomly sampled on a sphere of radius $\sqrt{S(S+1)} = \sqrt{3}/2$ with uniform probability distribution.

To obtain the correlations functions, we used not the definition (1.72), but its modified form. Both in the quantum and the classical cases, a spin lattice is a conservative system, which implies that it is invariant with respect to time translations and that the correlation functions depend only on the difference between the time arguments of two observables. For a classical spin lattice it means that

$$c_\alpha(\tau) = [M_\alpha(\tau)M_\alpha(0)]_{i.c.} = [M_\alpha(t+\tau)M_\alpha(t)]_{i.c.}, \quad \forall t. \quad (\text{A.1})$$

We can also express this property in the form

$$c_\alpha(\tau) = \frac{1}{T} \int_{t=0}^T dt [M_\alpha(t+\tau)M_\alpha(t)]_{i.c.} = \left[\frac{1}{T} \int_{t=0}^T dt M_\alpha(t+\tau)M_\alpha(t) \right]_{i.c.}. \quad (\text{A.2})$$

In principle, if the system is ergodic and the limit $T \rightarrow \infty$ is taken, then the averaging over the initial conditions is not necessary and the averaging over time is enough. In practice, however, not all the systems of interest are ergodic, and even if we are dealing with an ergodic system, the ergodization timescales are unclear. Nevertheless, it is convenient to perform the additional averaging over time as a way to improve the efficiency of the averaging procedure. Therefore, we perform the averaging over both the initial conditions and time.

Let us suppose that we stop our simulations at time T_{\max} . If we want to calculate the value of correlation function at time τ , we can use all the generated timeseries $M_\alpha(t)$:

$$c_\alpha(\tau) = \left[\frac{1}{T_{\max} - \tau} \int_{t=0}^{T_{\max}-\tau} dt M_\alpha(t+\tau)M_\alpha(t) \right]_{i.c.}. \quad (\text{A.3})$$

The drawback of this approach is that the time averaging of $c_\alpha(\tau)$ is almost absent for the values of τ close to T_{\max} . In practice, we can overcome this problem in the following way: if we want to calculate $c_\alpha(\tau)$ in the time window $0 \leq \tau \leq T_0$, we just need to choose $T_{\max} \gg T_0$, then we can neglect the change in the quality of the statistical averaging across the time window $0 \leq \tau \leq T_0$.

The equation (A.3) is the form we actually used to calculate the correlation functions.

A.1.3 Hybrid simulations

For the hybrid simulations, we integrated jointly the system of Eqs. (3.9) and (3.6), which corresponds to the Schrödinger representation for the states of the quantum cluster.

The initial conditions for the quantum cluster were sampled by the scheme described in Section 2.1 (see Eqs. (2.2), (2.3) and the corresponding discussion). The initial conditions for the classical part were generated similarly to how they were generated in the simulations of purely classical lattices (see the previous subsection A.1.2).

The equations of motion do not contain the time explicitly¹, which implies that

¹Of course, the Eqs. (3.9) and (3.6), describing the dynamics of the quantum and the classical parts respectively, include explicitly time-dependent terms induced by the other part of

the dynamics of the individual trajectories of the system are invariant with respect to the time translations. Also, the dynamics of the quantum part is unitary, and the dynamics of the classical part is Hamiltonian so that the Liouville theorem is true, thus, the “uniform” infinite-temperature distribution of initial states is also invariant under the time translation. As a result, the hybrid correlation function depends only on the difference in the time arguments of the observables, as in the purely quantum or the purely classical case. Hence, we can augment the averaging over initial conditions by the averaging over time, as done in Section A.1.2 for purely classical simulations.

Additionally, we should note that the definition 3.15 can be symmetrized with respect to $\mathfrak{M}_\alpha(t)$ and $\mathfrak{M}'_\alpha(t)$. Indeed, from the time-reversal symmetry and time-translational invariance, it follows that

$$[\mathfrak{M}'_\alpha(t)\mathfrak{M}_\alpha(0)]_{i.c.} = [\mathfrak{M}'_\alpha(-t)\mathfrak{M}_\alpha(0)]_{i.c.} = [\mathfrak{M}'_\alpha(0)\mathfrak{M}_\alpha(t)]_{i.c.}. \quad (\text{A.4})$$

As a consequence, we can rewrite Eq. (3.15) as

$$\mathfrak{C}_\alpha(t) = \frac{N}{2N_{Q'}} \cdot [\mathfrak{M}'_\alpha(t)\mathfrak{M}_\alpha(0) + \mathfrak{M}'_\alpha(0)\mathfrak{M}_\alpha(t)]_{i.c.} \quad (\text{A.5})$$

If we combine the time symmetrization with the time averaging, we obtain the final form of the hybrid correlation functions that we actually used to compute them:

$$\begin{aligned} \mathfrak{C}_\alpha(\tau) &= \\ &= \frac{N}{N_{Q'}} \cdot \left[\frac{1}{2(T_{\max} - \tau)} \int_{t=0}^{T_{\max}-\tau} dt (\mathfrak{M}'_\alpha(t + \tau)\mathfrak{M}_\alpha(t) + \mathfrak{M}'_\alpha(t)\mathfrak{M}_\alpha(t + \tau)) \right]_{i.c.} \end{aligned} \quad (\text{A.6})$$

A.2 Scaling of statistical errors

In Eq. (3.15), we defined the hybrid correlation functions in analogy with the form (3.12) of the quantum correlation functions. As we point out at the end of Section 3.2, the averaging over initial conditions would be more efficient had it been possible to define the hybrid auto-correlation functions on basis of the form (1.74) of the quantum correlation functions. Let us discuss in details the difference in the speed of convergence of the averaging procedures in Eqs. (3.12) and (1.74).

For the form (1.74), statistical error scales with the number of computational the lattice. The system of equations as a whole is, however, autonomous.

runs R as² $1/\sqrt{(D+1)R}$. As a consequence, it is enough to perform only one computational run even for moderately large quantum systems.

For the form (3.12), the statistical error scales only as $1/\sqrt{R}$. The same is true for the classical and the hybrid correlation functions (see Eqs. (3.11) and (3.15)). As we see, there is no additional factor $1/\sqrt{D+1}$. As a result, one needs to perform a lot of computational runs in order to reach a reasonable accuracy.

The averaging over initial conditions in Eq. (3.12) can be combined with the averaging over time:

$$C_\alpha(\tau) = \left[\frac{1}{T_{\max} - \tau} \int_{t=0}^{T_{\max} - \tau} dt \langle \psi(t + \tau) | \mathcal{M}_\alpha | \psi(t + \tau) \rangle \langle \psi(t) | \mathcal{M}_\alpha | \psi(t) \rangle \right]_{i.c.} . \quad (\text{A.7})$$

If $\tau \ll T_{\max}$, statistical error scales with the number of runs R and the upper limit of time integration T_{\max} as $1/\sqrt{R} \cdot \sqrt{\tau_c/T_{\max}}$, where τ_c is the correlation time.

As Elsayed and Fine showed in [37], one can calculate $C_\alpha(\tau)$ by using a single computational run in Eq. (A.7), but the upper limit of integration T_{\max} should be sufficiently large. In practice, however, the averaging over initial conditions is more efficient than the averaging over time, given it is unclear what is the value of τ_c .

A.3 Numerical integration of equations of motion

In purely quantum, purely classical and hybrid simulations, the equations of motion were integrated using explicit Runge-Kutta scheme of 4-th order with the fixed time step of $2^{-7} J^{-1}$, or, in some cases, $2^{-6} J^{-1}$ (to speed up the calculations). For one-dimensional and two-dimensional lattices, the time unit J^{-1} was defined as $J = \sqrt{J_x^2 + J_y^2 + J_z^2}$, where J_x, J_y, J_z are the nearest-neighbor coupling constants. In the cases of FID calculations for real materials, the time unit J^{-1} was defined as $J = \gamma^2 \hbar^2 / a_0^3$, where γ is the gyromagnetic ratio of corresponding nuclei and a_0 specified the lattice period. For CaF_2 and ^{29}Si -enriched silicon a_0 was the period of the cubic lattice, for calcium fluorapatite it was the distance between the neighbouring fluorine nuclei in the chain.

The choice of the time step is discussed in Refs. [37, 31].

In the case of purely classical and hybrid simulations, for each set of initial conditions, we integrated the dynamical equations up to the time $T_{\max} \sim 10T_0$, where T_0 was the maximum time for which the correlation function $C_\alpha(t)$ was to be computed. The number of initial conditions was then chosen sufficiently large

²We discussed the scaling of statistical error in the case of a single computational run in Section 2.3.

| Dim. | Coupling constants | Figure | Plot type | N ^o of runs |
|------|-----------------------|---------------------|-------------------|------------------------|
| 1 | (-0.41, -0.41, 0.82) | 4.1(a) | Hybrid, 14 spins | 30000 |
| | | 4.1(a') | Hybrid, 12 spins | 13127 |
| | | | Classical | 10000 |
| | (0.707, 0.707, 0.000) | 4.3(a) | Hybrid, 14 spins | 30030 |
| | | 4.3(a') | Hybrid, 12 spins | 43078 |
| | | | Classical | 10000 |
| | (0.518, 0.830, 0.207) | 4.1(b,c), 4.3(b) | Hybrid, 16 spins | 10860 |
| | | | Hybrid, 12 spins | 43078 |
| | | 4.1(b',c'), 4.3(b') | Classical | 10000 |
| 2 | (-0.41, -0.41, 0.82) | 4.4(a) | Hybrid, 4×4 spins | 41261 |
| | | | Hybrid, 13 spins | 188000 |
| | | | Hybrid, 3×3 spins | 76203 |
| | | 4.4(a') | Classical | 16006 |
| | (0.707, 0.707, 0.00) | 4.7(a) | Hybrid, 13 spins | 64000 |
| | | | Hybrid, 3×3 spins | 8006 |
| | | 4.7(a') | Classical | 16000 |
| | (0.518, 0.830, 0.207) | 4.4(b), 4.6(a,b) | Hybrid, 4×4 spins | 5339 |
| | | | Hybrid, 13 spins | 60000 |
| | | | Hybrid, 3×3 spins | 8006 |
| | | 4.4(b'), 4.6(a',b') | Classical | 16006 |
| | (0.400, 0.900, 0.173) | 4.7(b,c,d) | Hybrid, 4×4 spins | 15699 |
| | | | Hybrid, 13 spins | 90000 |
| | | | Hybrid, 3×3 spins | 16000 |
| | | 4.7(b',c',d') | Classical | 16000 |

Table A.1: The number of computational runs behind the plotted correlation functions of Chapter 4. The time length of each run is $10 T_0$ or larger, where T_0 is the time range where the correlation function is plotted in the respective figure.

to achieve the target accuracy of $C_\alpha(t)$.

A.4 Statistics behind the plots

In Tables A.1 and A.2, we list the number of computational runs behind the plots presented in Chapters 4 and 5 respectively.

| Material | $\mathbf{B}_0 \parallel$ | Figure | Plot type | N ^o of runs |
|---|--------------------------|---------------------|-----------------------------------|------------------------|
| CaF ₂ | [001] | 5.1(a), 5.2(a), 5.3 | Hybrid | $4.3 \cdot 10^6$ |
| | | | Classical | $4.0 \cdot 10^5$ |
| | [011] | 5.1(b), 5.2(b) | Hybrid | $3.9 \cdot 10^6$ |
| | | | Classical | $4.0 \cdot 10^5$ |
| | [111] | 5.1(c), 5.2(c) | Hybrid | $1.1 \cdot 10^6$ |
| | | | Classical | $4.0 \cdot 10^5$ |
| ²⁹ Si | [001] | 5.6(a,b) | Hybrid | 382768 |
| | | | Classical | 456384 |
| | [011] | 5.7(a,b) | Hybrid | 398896 |
| | | | Classical | 168098 |
| | [111] | 5.8(a,b) | Hybrid, cluster 1 | 331040 |
| | | | Hybrid, cluster 2 | 647527 |
| Classical | | | 348932 | |
| Ca ₁₀ (PO ₄) ₆ F ₂ | [001] | 5.10 | Hybrid, unlike spins and disorder | 281496 |
| | | | Hybrid, unlike spins | 37868 |
| | | | Hybrid | 44878 |
| | | | Hybrid, single chain | 93562 |

Table A.2: The number of computational runs behind the plotted correlation functions of Chapter 5. The time length of each run is $10 T_0$, where T_0 is the time range where the correlation function is plotted in the respective figure.

Appendix B

Overview of SpinLattice library

Facilitation of the numerical simulations, so different in the type of approximations and in the character of the lattices considered, required creation of a programming library combining generality of approach with an efficient code implementation. [SpinLattice](#) library is the result of this endeavor. It is not the most general and, probably, not the most efficient version of the program that could be written, but it is certainly a convenient tool.

B.1 The choice of the programming language

The first versions of the library were written in Python language, specifically its 2.7 version. The simulations of Chapter 4 used the Python implementation. More computationally-demanding simulations of Chapter 5 required heavy optimization and restructuring of the code. In the process, a decision was made to rewrite the library in Julia language (version 0.6.x). As a result, the current version of the library is written in the latter language.

[Julia](#) is a relatively new and steadily developing language, which was designed with numerical simulations and parallelism in mind from the start. It combines the interactivity and simplicity of Python with the speed and the efficiency of Fortran or C. Moreover, if one uses it in conjunction with a [Jupyter notebook](#), then the overall experience is quite close to the one you get while interacting with Mathematica or Matlab. At the same time, Julia is still a general-purpose programming language and it is Open Source.

The key feature allowing Julia to be so fast is the multiple dispatch. It means that the same name can label different functions with different sets of input parameters and different behaviour. The choice of the particular function is determined by the tuple of input argument types. When the function is run in the Julia interactive shell, the compiler looks at the types of input parameters, chooses a

particular function and compiles its version, which is optimised for the set of input types and is as efficient as something one would get by compiling a C or a Fortran code. Combined with its flexible system of parametric types, it allows one to write very general and fast code in an economical fashion. One good illustration of the potential of Julia is [JuliaDiffEq library](#). Among all the different useful elements, it contains implementations of a multitude of integrators for Ordinary Differential equations (see <https://github.com/JuliaDiffEq/OrdinaryDiffEq.jl>), which are compatible with user-defined Julia structures, provided they have an array interface. The usefulness of this feature is easily shown, once we consider, for example, hybrid simulations. The state of the hybrid lattice is parameterized by a complex array corresponding to the wave function of the quantum cluster and by three real arrays corresponding to three components of classical spins. If one were to use Fortran integrator library such as, for example, LSODA, one would have to put wave function and three components of classical spins into one large complex array. Not only the efficiency is lost due to storing real values in complex format, but such a layout of data is also inconvenient to work with. Needless to say, availability of such a library as JuliaDiffEq was one of the motivations driving the transition of SpinLattice library to Julia language.

B.2 Quick start guide

Running a simulation with the use of the SpinLattice library is a multi-step procedure.

First, one needs to specify a `Lattice` one wants to simulate. In particular, one needs to specify the set of primitive vectors, coordinates of the lattice nodes in the unit cell, the coupling constants, and a homogeneous external magnetic field.

The next step is to build the Lattice Problem, or, alternatively, `LProblem`. This structure contains information about the Model approximation, the set of correlation functions we want to calculate and about the maximal time we want our simulation to run. There are four basic variations of Models: `Exact`, `PureClassical`, `Clustered` and `Hybrid`. The first two variations correspond to treating the whole lattice quantum mechanically or classically respectively. `Clustered` implies a division of the lattice into identical non-entangled clusters. Finally, `Hybrid` corresponds to the Hybrid Lattice approximation described in this thesis.

Finally, one can run the simulation of the `LProblem`. At this step, one can choose the number of runs for statistical averaging and the integrator from JuliaDiffEq library, which is used to solve the equations of motion. It is also possible to control the output file and the logging file: after each run, the program makes an entry into the logging file. The entry contains the information about the serial

number of the run and about the time it took. The logging file provides the means to track the simulation progress and to estimate the efficiency of the program.

Let us illustrate the above discussion by several examples of scripts.

Listing B.1: task_caf2_001.jl

```

1 using SpinLattice
2
3 L = Lattice((9,9,9), (-0.5,-0.5,1.0), Interaction(MDI(0,0,1)), (0.,0.,0.))
4 LP = build_problem(L, SpinLattice.Hybrid(), (1,1,9); Tmax = 6.0, timestep = 2.0^-7,
   delimiter = 10., links = (:all, :allq)), axes = [:x]);
5 parallel_simulate(LP, 50000, OrdinaryDiffEq.RK4(), SpinLattice.Logger{:local, :file}()
   ; adaptive=false, dt = LP.timestep)

```

Listing B.2: task_caf2_111.jl

```

1 using SpinLattice
2
3 L = Lattice((9,9,9), (-0.5,-0.5,1.0), Interaction(MDI(1,1,1)), (0.,0.,0.))
4 LP = build_problem(L, SpinLattice.Hybrid(), SpinLattice.SpinArray(L, [(i,i,i) for i=1:
   9], :diag); Tmax = 6.0, timestep = 2.0^-7, delimiter = 10., links = (:all, :allq)),
   axes = [:x]);
5 parallel_simulate(LP, 50000, OrdinaryDiffEq.RK4(), SpinLattice.Logger{:local, :file}()
   ; adaptive=false, dt = LP.timestep)

```

The Listings B.1, B.2 contain the scripts which were used to run hybrid simulations for FID in CaF₂ and magnetic fields along [001] and [111] crystal directions respectively (see Fig. 5.1(a,b)). The structure of the scripts is identical. The first line tells the program to load `SpinLattice` library. In line 3, the `Lattice` structure is constructed. The signature of the function call is `Lattice(dims, Js, Jfunc, hs)`. Here `dims` is the size of the lattice in terms of the basis cells, `hs` is the external magnetic field, `Js` and `Jfunc` parameterize the coupling constants:

$$J_{i,j}^\alpha = J_s[\alpha] \cdot J_{\text{func}}(\mathbf{r}_i - \mathbf{r}_j), \quad (\text{B.1})$$

The arguments `MDI(0,0,1)` and `MDI(1,1,1)` specify that the spins interact with truncated magnetic dipolar-dipolar interaction for the magnetic field along [001] and [111] crystal directions respectively. Another possible choice of the coupling function is `nearest_neighbours`.

`LProblem` structure is constructed in line 4. The signature of the function call is `build_problem(Lattice, Model, args...; kwargs...)`. The tuple `args` contains the arguments that parameterize the model used. For `Hybrid` model, one needs to specify the subset of lattice sites used to construct the quantum cluster. There

are two ways to do that. The first is to specify the dimension of a block of spins. This block is a parallelepiped with the faces parallel to the lattice boundaries. It is the approach used in Listing B.1. The other way is to directly specify coordinates of the lattice sites which comprise the quantum cluster. This goal is achieved with the help of `SpinArray` structure. The signature of its constructor is `SpinArray(Lattice, array_of_coordinates, label)`. This second approach is adopted in Listing B.2. The `Exact` and `PureClassical` models do not require additional parameters. The `Clustered` model requires the size of the block to be specified; the dimensions of the block must be divisors of the corresponding dimensions of the `Lattice`.

The dictionary of keyword arguments `kwargs` specifies the correlations functions to calculate and the running time of the simulations. Currently supported correlation functions are of the form:

$$C_{\alpha}^{(\mathcal{L}_1, \mathcal{L}_2)}(t) = \langle \mathcal{M}_{\alpha}^{\mathcal{L}_1}(t) \mathcal{M}_{\alpha}^{\mathcal{L}_2} \rangle, \quad \mathcal{M}_{\alpha}^{\mathcal{L}_p} = \sum_{i \in \mathcal{L}_p} S_i^{\alpha}. \quad (\text{B.2})$$

Keyword argument `axes` specifies the choices of α and the keyword argument `links` specifies the pairs of subsets of lattice sites $(\mathcal{L}_1, \mathcal{L}_2)$. It may be a single pair or multiple pairs:

$$\text{links} = (\mathcal{L}_1, \mathcal{L}_2) \quad \text{or} \quad \text{links} = ((\mathcal{L}_1, \mathcal{L}_2), (\mathcal{L}'_1, \mathcal{L}'_2), (\mathcal{L}''_1, \mathcal{L}''_2), \dots) \quad (\text{B.3})$$

The subset of spins can be specified either by a symbol such as `:all` and `:allq`, or by a `SpinArray`. The symbol `:all` corresponds to the whole lattice, the symbol `:allq` corresponds to the spins of the quantum cluster, this symbol works only for the `Hybrid` model.

The correlation functions are calculated from 0.0 to `Tmax` with time step `tstep`. The keyword argument `delimiter` specifies that the equations of motion are integrated till `delimiter · Tmax`. The correlation functions are extracted from timeseries of observables (see Section 3.2), which are calculated from 0.0 to `delimiter · Tmax` with time step `tstep`.

Finally, the code in line 5 proceeds with the simulations. The scripts of Listings B.1 and B.2 were executed by a command of the form: `julia -p nworkers script.jl`. It means that in addition to the main master process, `nworkers` slave processes are started. The `parallel_simulate` function in line 5 of the scripts runs the simulations on each of the slave processes and on the master process in parallel. The signature of the function call is `parallel_simulate(LProblem, nTrials, integrator, logger; kwargs...)`. Here, `nTrials` denotes the number of initial conditions for statistical averaging, `integrator` specifies the method of integration of the equations of motion (in

all the examples the 4-th order Runge-Kutta method is used) and `logger` specifies logging and saving of the results. Keyword arguments `kwargs` are passed to the integrator. The meaning of the keyword arguments used in Listings B.1 and B.2 is the following: the integrator is told not to use adaptive time-stepping; instead, a fixed time-step is provided. We should note that all these arguments are applied to each of the parallel processes. For example, if `nworkers = 15` and `nTrials = 1000`, then each of the parallel processes will do 1000 runs, so that the total statistics would be 16000 runs.

Let us also describe a more complicated example, which is shown in the Listing B.3.

Listing B.3: `task_si_111.jl`

```

1 using SpinLattice
2
3 basis = 0.5*hcat([0,1,1],[1,1,0],[1,0,1])
4 cell_vecs = [[0,0,0],[0.25,0.25,0.25]]
5
6 L = SpinLattice.Lattice((9,9,9), (-0.5,-0.5,1.0), SpinLattice.Interaction(SpinLattice.
    MDI((1,1,1))), (0.,0.,0.), basis, cell_vecs, :fcc, :diamond)
7
8 spins = [((3,3,3), 1), ((3,3,3), 2)]
9 spins1 = [(spin[1].+vec, spin[2]) for vec in [(1,0,0),(0,1,0),(0,0,1)] for spin in
    spins]
10 spins2 = [(spin[1].-vec, spin[2]) for vec in [(1,0,0),(0,1,0),(0,0,1)] for spin in
    spins]
11
12 sar = SpinArray(L, vcat(spins, spins1, spins2), :DBFG)
13 sar2 = SpinArray(L, spins, :central)
14
15 LP = build_problem(L, Hybrid(), sar; Tmax = 3., tstep = 2.0^-8, delimiter = 10., links
    = (:all, sar2), axes = [:x]);
16
17 parallel_simulate(LP, 50000, OrdinaryDiffEq.RK4(), SpinLattice.Logger{:local, :file}()
    ; adaptive=false, dt = LP.tstep)

```

It corresponds to the hybrid simulations of FID in ^{29}Si -enriched silicon for the external magnetic field along the [111] crystal direction (see Fig. 5.8). Specifically it corresponds to the simulation for quantum cluster 1 (see Fig. 5.5 (c)). In this case the full signature of the `Lattice` constructor is used:

```
Lattice(dims, Js, Jfunc, hs, basis, cell_vecs, lattice_label, basis_cell_label)
```

The columns of `basis` matrix are cartesian coordinates of the primitive vectors of the lattice, `cell_vecs` is an array of cartesian coordinates of basis cell nodes. For FID calculations in CaF_2 (Listings B.1 and B.2) we did not specify the last

four arguments, so the fallback values were used. The fallback `basis` is a unit matrix, the fallback `cell_vecs` array contains single zero vector, fallback values of `lattice_label` and `basis_cell_label` are `:cubic` and `:simple` respectively.

A different format is used to represent the lattice site coordinates:

```
(basis_cell_coord, index_inside_basis_cell)
```

For example, in $((3,3,3), 1)$, $(3,3,3)$ are the coordinates of a particular basis cell in terms of primitive vectors, and 1 is the index of a particular node inside this basis cell. Cartesian coordinates of the lattice site are:

```
basis*basis_cell_coord .+ cell_vecs[index_inside_basis_cell]
```

List of Figures

| | | |
|-----|--|----|
| 3.1 | Sketch of a hybrid lattice: a cluster of spins $1/2$ surrounded by an environment of classical spins. The quantum cluster is described by a wave function $ \psi\rangle$. Classical spins are represented by three-dimensional vectors. | 38 |
| 4.1 | Correlation functions $C_\alpha(t)$ for one-dimensional periodic chains with nearest neighbours interactions. The interaction constants are indicated above each plot. The left column of plots compares the results of hybrid simulations with the reference plots obtained by direct quantum calculations. The right column does the same for purely classical simulations. For both hybrid and classical simulations, the full lattice size is 92. The sizes of quantum clusters in hybrid simulations and in reference quantum calculations are indicated in the plot legends. | 46 |
| 4.2 | Size dependence of correlation functions $C_\alpha(t)$ for one-dimensional periodic chains with nearest-neighbour interactions obtained from direct quantum calculations. The interaction constants are the same as in Fig. 4.1. The present figure illustrates that quantum reference plots used in Fig. 4.1 represent the thermodynamic limit. | 47 |
| 4.3 | Correlation functions $C_\alpha(t)$ for one-dimensional periodic chains with nearest-neighbour interactions. The notations here are the same as in Fig. 4.1. For both hybrid and classical simulations, the full lattice size is 92. Lines in (a,a') labeled as "Analytical" are Gaussians that represent the analytical result for the spin- $1/2$ XX chain in the thermodynamic limit [51]. | 48 |
| 4.4 | Correlation functions $C_\alpha(t)$ for two-dimensional periodic lattices with nearest-neighbour interaction. The notations in (a,a',b,b') are the same as in Fig. 4.1. For both hybrid and classical simulations, the full lattice size is 9×9 . The shapes of quantum clusters for hybrid simulations are shown in (c). | 49 |

| | | |
|-----|--|----|
| 4.5 | Size dependence of correlation functions $C_\alpha(t)$ for two-dimensional periodic chains with nearest-neighbour interactions obtained from purely quantum simulations. The interaction constants are the same as in Fig. 4.4. These plots illustrates that quantum results used in Fig. 4.4 as references represent the thermodynamic limit. | 50 |
| 4.6 | Correlation functions $C_\alpha(t)$ for two-dimensional periodic lattices with nearest-neighbour interactions. The notations are the same as in Fig. 4.1. For both hybrid and classical simulations, the full lattice size is 9×9 . The shapes of quantum clusters for hybrid simulations are shown in Fig. 4.1(c). | 50 |
| 4.7 | Correlation functions $C_\alpha(t)$ for two-dimensional periodic lattices with nearest-neighbour interaction. The notations are the same as in Fig. 4.1. For both hybrid and classical simulations, the full lattice size is 9×9 . The shapes of quantum clusters for hybrid simulations are shown in Fig. 4.1(c). | 51 |
| 5.1 | FIDs in CaF_2 for external magnetic field \mathbf{B}_0 along the following crystal directions: (a) [001]; (b) [011]; (c) [111]. Hybrid and classical simulations are compared with the experimental results of Ref.[52]. For both hybrid and classical simulations, the full lattice size is $9 \times 9 \times 9$. The quantum cluster in hybrid simulations was a chain extending along [001] crystal direction in (a); a chain passing through the entire lattice and oriented along the [100] crystal direction in (b) and a chain along [111] crystal direction in (c). The insets contain semi-logarithmic plots of the respective FIDs. | 54 |
| 5.2 | Illustration of the statistical uncertainty of the hybrid and the classical plots of CaF_2 FIDs appearing in Fig.5.1. Here, panels (a), (b) and (c) include hybrid and classical plots obtained not only from the full generated statistics but also from the half of it — see the plot legend. The total number of computational runs corresponding to the full generated statistics is listed in Table A.1. | 57 |
| 5.3 | Long-time fits to the experimental and computed FIDs in CaF_2 for external magnetic field \mathbf{B}_0 along the [001] crystal direction. The three original plots are from the semilogarithmic inset of Fig.5.1(a): (a) hybrid calculation, (b) classical calculation, (c) experiment. The functional form of the fits is $C_{\text{fit}}(t) = c \cdot e^{-\gamma t} \cdot \sin[\omega(t - t_0)]$. Parameters γ , ω , c and t_0 are listed in Table 5.1. | 58 |
| 5.4 | Diamond crystal structure. The black arrows represent the primitive vectors of the lattice. | 60 |

| | | |
|------|---|----|
| 5.5 | Schemes of the quantum clusters used for the hybrid simulations: (a) cluster used for the case when $\mathbf{B}_0 \parallel [001]$; (b) cluster used for the case when $\mathbf{B}_0 \parallel [011]$; (c), (d) cluster 1 and cluster 2 respectively, used for the case when $\mathbf{B}_0 \parallel [111]$. Marked sites correspond to the central spins of the clusters. | 61 |
| 5.6 | Absorption peak lineshape (a),(a') and FID (b),(b') in ^{29}Si diamond for \mathbf{B}_0 along $[001]$ crystal direction. In the left column, we present the comparison of the hybrid and the classical simulations with two experimental curves of Verhulst et al. for the same orientation of the magnetic field. In the right column, we present the comparison of the theoretical predictions of Jensen and Lundin and Zbov with the same experimental data. The scheme of the quantum cluster used in the hybrid simulation is displayed in Fig. 5.5(a). | 62 |
| 5.7 | Absorption peak line-shape (a),(a') and FID (b),(b') in ^{29}Si diamond for \mathbf{B}_0 along $[011]$ crystal direction. In the left column, we present the comparison of the hybrid and the classical simulations with two experimental curves of Verhulst et al. for the same orientation of the magnetic field. In the right column, we present the comparison of the theoretical predictions of Jensen and Lundin and Zbov with the same experimental data. The scheme of the quantum cluster used in the hybrid simulation is displayed in Fig. 5.5(b). | 63 |
| 5.8 | Absorption peak line-shape (a),(a') and FID (b),(b') in ^{29}Si diamond for \mathbf{B}_0 along $[111]$ crystal direction. In the left column, we present the comparison of the hybrid simulations for two choices of the quantum cluster and of the classical simulations with two experimental curves of Verhulst et al. for the same orientation of the magnetic field. In the right column, we present the comparison of the theoretical predictions of Jensen and Lundin and Zbov with the same experimental data. The schemes of the quantum clusters used in the hybrid simulations are displayed in Figs. 5.5(c,d). | 64 |
| 5.9 | Scheme of a unit cell of fluorapatite in two different projections ((a) and (b)). Only F (blue) and P (red) atoms are shown. | 67 |
| 5.10 | ^{19}F FID in fluorapatite. See the text for the explanation of the plot legend. | 70 |

List of Tables

| | | |
|-----|--|----|
| 5.1 | The values of the parameters γ , ω , c and t_0 obtained from fitting the functional dependence (4.1) to the FIDs presented on the Fig. 5.1(a). The fitting plots themselves are presented in Fig. 5.3. | 55 |
| A.1 | The number of computational runs behind the plotted correlation functions of Chapter 4. The time length of each run is $10 T_0$ or larger, where T_0 is the time range where the correlation function is plotted in the respective figure. | 89 |
| A.2 | The number of computational runs behind the plotted correlation functions of Chapter 5. The time length of each run is $10 T_0$, where T_0 is the time range where the correlation function is plotted in the respective figure. | 90 |

Bibliography

- [1] Abragam, A. *Principles of Nuclear Magnetism*, (Oxford University Press, 1961).
- [2] Slichter, C. P. *Principles of Magnetic Resonance*, (Springer Berlin Heidelberg, 1990).
- [3] Yang, K.-H. and Hirschfelder, J. O. “Generalizations of classical Poisson brackets to include spin”. *Phys. Rev. A* **22**, 1814–1816 (1980).
- [4] de Wijn, A. S., Hess, B. and Fine, B. V. “Lyapunov instabilities in lattices of interacting classical spins at infinite temperature”. *Journal of Physics A: Mathematical and Theoretical* **46**, 254012 (2013).
- [5] Van Vleck, J. H. “The Dipolar Broadening of Magnetic Resonance Lines in Crystals”. *Phys. Rev.* **74**, 1168–1183 (1948).
- [6] Lowe, I. J. and Norberg, R. E. “Free-Induction Decay in Solids”. *Phys. Rev.* **107**, 46–61 (1957).
- [7] Ashcroft, N. and Mermin, N. *Solid State Physics*, (Saunders College, Philadelphia, 1976).
- [8] Bloch, F. “Nuclear Induction”. *Phys. Rev.* **70**, 460–474 (1946).
- [9] Jensen, S. J. K. and Hansen, E. K. “Sixth and Eighth Moments of the Magnetic-Resonance Lines of a Dipolar-Coupled Rigid Lattice”. *Phys. Rev. B* **7**, 2910–2917 (1973).
- [10] Zwanzig, R. “Memory Effects in Irreversible Thermodynamics”. *Phys. Rev.* **124**, 983–992 (1961).
- [11] Mori, H. “Transport, Collective Motion, and Brownian Motion”. *Progress of Theoretical Physics* **33**, 423–455 (1965).
- [12] Tjon, J. A. “Quantum Theory of Magnetic-Resonance Line Shape in a Rigid Lattice”. *Phys. Rev.* **143**, 259–263 (1966).

-
- [13] Lado, F., Memory, J. D. and Parker, G. W. “General Approach to the Line-Shape Problem in Nuclear-Magnetic-Resonance Spectra”. *Phys. Rev. B* **4**, 1406–1422 (1971).
- [14] Parker, G. W. and Lado, F. “Calculation of NMR Line Shapes Using the Memory-Function Approach”. *Phys. Rev. B* **8**, 3081 (1973).
- [15] Engelsberg, M. and Chao, N.-C. “Continued-fraction approximants to spin correlation functions. Application to NMR line shapes”. *Phys. Rev. B* **12**, 5043–5050 (1975).
- [16] Jensen, J. “Dipolar broadening of $I = 1/2$ NMR spectra of solids”. *Phys. Rev. B* **52**, 9611–9619 (1995).
- [17] Borckmans, P. and Walgraef, D. “Irreversibility in paramagnetic spin systems”. *Physica* **35**, 80–96 (1967).
- [18] Borckmans, P. and Walgraef, D. “Irreversibility in Paramagnetic Spin Systems: Free Induction Decay and Spin Diffusion”. *Phys. Rev.* **167**, 282–288 (1968).
- [19] Borckmans, P. and Walgraef, D. “Long-Time Behavior of the Free-Induction Decay in Paramagnetic Spin Systems”. *Phys. Rev. Lett.* **21**, 1516–1517 (1968).
- [20] Prigogine, I. *Non-equilibrium statistical mechanics*. Monographs in statistical physics and thermodynamics, (Interscience Publishers, 1962).
- [21] Becker, K. W., Plefka, T. and Sauermann, G. “Spin correlation function for free-induction decay in dipolar systems”. *Journal of Physics C: Solid State Physics* **9**, 4041 (1976).
- [22] Sauermann, G. and Wiegand, M. “Frequency matrix for the calculation of correlation functions in dipolar systems”. *Physica B+C* **103**, 309–314 (1981).
- [23] Fine, B. V. “NMR Spin-Spin Relaxation as Kinetics in Spin Phase Space”. *Phys. Rev. Lett.* **79**, 4673–4676 (1997).
- [24] Fine, B. V. “Theory of high temperature spin dynamics”. Ph.D. thesis, University of Illinois at Urbana-Champaign (2000). URL <http://www.thphys.uni-heidelberg.de/~fine/thesis.ps>.
- [25] Lundin, A. A. and Provotorov, B. N. “Contribution to the statistical theory of the nuclear magnetic resonance line shape”. *JETP* **43**, 1149 (1976).

-
- [26] Lundin, A. A. and Makarenko, A. V. “Shape of NMR spectra of solids”. *JETP* **60**, 570 (1984).
- [27] Lundin, A. A. “Shape of NMR spectra in solids. The pair interaction model”. *Sov. Phys. JETP* **102**, 352 (1992).
- [28] Lundin, A. A. “Asymptotic similarity of temporal correlation functions and the problem of NMR lineshape in solids”. *JETP* **83**, 759 (1996).
- [29] Gade, S. and Lowe, I. J. “Nuclear Magnetic Resonance Line-Shape Calculations for a Spin System in a Fixed Lattice”. *Phys. Rev.* **148**, 382–392 (1966).
- [30] Jensen, S. J. K. and Platz, O. “Free-Induction-Decay Shapes in a Dipolar-Coupled Rigid Lattice of Infinite Nuclear Spins”. *Phys. Rev. B* **7**, 31 (1973).
- [31] Elsayed, T. A. and Fine, B. V. “Effectiveness of classical spin simulations for describing NMR relaxation of quantum spins”. *Phys. Rev. B* **91**, 094424 (2015).
- [32] Hams, A. and De Raedt, H. “Fast algorithm for finding the eigenvalue distribution of very large matrices”. *Phys. Rev. E* **62**, 4365–4377 (2000).
- [33] Gemmer, J., Michel, M. and Mahler, G. *Quantum Thermodynamics*, (Springer-Verlag Berlin Heidelberg, 2004).
- [34] Goldstein, S., Lebowitz, J. L., Tumulka, R. and Zanghì, N. “Canonical Typicality”. *Phys. Rev. Lett.* **96**, 050403 (2006).
- [35] Popescu, S., Short, A. J. and Winter, A. “Entanglement and the foundations of statistical mechanics”. *Nature Physics* **2**, 754 EP – (2006). Article.
- [36] Bartsch, C. and Gemmer, J. “Dynamical Typicality of Quantum Expectation Values”. *Phys. Rev. Lett.* **102**, 110403 (2009).
- [37] Elsayed, T. A. and Fine, B. V. “Regression relation for pure quantum states and its implications for efficient computing”. *Phys. Rev. Lett.* **110**, 070404 (2013).
- [38] Dobrovitski, V. V. and De Raedt, H. A. “Efficient scheme for numerical simulations of the spin-bath decoherence”. *Phys. Rev. E* **67**, 056702 (2003).
- [39] Zhang, W., Konstantinidis, N., Al-Hassanieh, K. A. and Dobrovitski, V. V. “Modelling decoherence in quantum spin systems”. *J. Phys. Condens. Matter* **19**, 083202 (2007).

-
- [40] Steinigeweg, R., Jin, F., Schmidtke, D., De Raedt, H. *et al.* “Real-time broadening of nonequilibrium density profiles and the role of the specific initial-state realization”. *Phys. Rev. B* **95**, 035155 (2017).
- [41] Navez, P., Starkov, G. A. and Fine, B. V. “Classical spin simulations with a quantum two-spin correction”. *The European Physical Journal Special Topics* **227**, 2013–2024 (2019).
- [42] Wurtz, J., Polkovnikov, A. and Sels, D. “Cluster truncated Wigner approximation in strongly interacting systems”. *Annals of Physics* **395**, 341–365 (2018).
- [43] Wurtz, J. and Polkovnikov, A. “Quantum Hydrodynamics in Spin Chains with Phase Space Methods” (2018). [arXiv:1808.08977](https://arxiv.org/abs/1808.08977).
- [44] Fine, B. V. “Typical state of an isolated quantum system with fixed energy and unrestricted participation of eigenstates”. *Phys. Rev. E* **80**, 051130 (2009).
- [45] Fine, B. V. “Long-time Relaxation on Spin Lattice as a Manifestation of Chaotic Dynamics”. *Int. J. Mod. Phys. B* **18**, 1119–1159 (2004).
- [46] Gemmer, J. and Mahler, G. “Distribution of local entropy in the Hilbert space of bi-partite quantum systems: origin of Jaynes' principle”. *The European Physical Journal B - Condensed Matter* **31**, 249–257 (2003).
- [47] Álvarez, G. A., Danieli, E. P., Levstein, P. R. and Pastawski, H. M. “Quantum Parallelism as a Tool for Ensemble Spin Dynamics Calculations”. *Phys. Rev. Lett.* **101**, 120503 (2008).
- [48] Negele, J. W. and Orland, H. *Quantum Many-particle Systems (Frontiers in Physics)*, (Perseus Books, 1998).
- [49] Wigner, E. P. *Group Theory and its Application to the Quantum Mechanics of Atomic Spectra*, (Academic Press, 1959).
- [50] Sakurai, J. J. *Modern Quantum Mechanics*. Modern Quantum Mechanics, (Addison-Wesley Publishing, C., 1994).
- [51] Brandt, U. and Jacoby, K. “Exact results for the dynamics of one-dimensional spin-systems”. *Zeitschrift für Physik B Condensed Matter* **25**, 181–187 (1976).
- [52] Engelsberg, M. and Lowe, I. J. “Free-induction-decay measurements and determination of moments in CaF_2 ”. *Phys. Rev. B* **10**, 822–832 (1974).

-
- [53] Morgan, S. W., Fine, B. V. and Saam, B. “Universal Long-Time Behavior of Nuclear Spin Decays in a Solid”. *Phys. Rev. Lett.* **101**, 067601 (2008).
- [54] Sorte, E. G., Fine, B. V. and Saam, B. “Long-time behavior of nuclear spin decays in various lattices”. *Phys. Rev. B* **83**, 064302 (2011).
- [55] Meier, B., Kohlrantz, J. and Haase, J. “Eigenmodes in the Long-Time Behavior of a Coupled Spin System Measured by Nuclear Magnetic Resonance”. *Phys. Rev. Lett.* **108**, 177602 (2012).
- [56] Fabricius, K., Löw, U. and Stolze, J. “Dynamic correlations of antiferromagnetic spin- $\frac{1}{2}$ XXZ chains at arbitrary temperature from complete diagonalization”. *Phys. Rev. B* **55**, 5833–5846 (1997).
- [57] Fine, B. V. “Universal Long-Time Relaxation on Lattices of Classical Spins: Markovian Behavior on Non-Markovian Timescales”. *J. Stat. Phys.* **112**, 319–327 (2003).
- [58] Fine, B. V. “Long-Time Behavior of Spin Echo”. *Phys. Rev. Lett.* **94**, 247601 (2005).
- [59] Lundin, A. A. and Zobov, V. E. “Simulations of the Nuclear Magnetic System of a Crystal by the System of Classical Magnetic Moments”. *J. Magn. Reson.* **26**, 229 (1977).
- [60] Engelsberg, M., Lowe, I. J. and Carolan, J. L. “Nuclear-Magnetic-Resonance Line Shape of a Linear Chain of Spins”. *Phys. Rev. B* **7**, 924–929 (1973).
- [61] Lefmann, K., Buras, B., Pedersen, E. J., Shabanova, E. S. *et al.* “NMR spectra of pure ^{13}C diamond”. *Phys. Rev. B* **50**, 15623–15627 (1994).
- [62] Verhulst, A. S., Maryenko, D., Yamamoto, Y. and Itoh, K. M. “Double and single peaks in nuclear magnetic resonance spectra of natural and ^{29}Si – enriched single-crystal silicon”. *Phys. Rev. B* **68**, 054105 (2003).
- [63] Lundin, A. A. and Zobov, V. E. “Asymptotic Similarity of Time Correlation Functions and Shape of the ^{13}C and ^{29}Si NMR Spectra in Diamond and Silicon”. *JETP* **127**, 305–315 (2018).
- [64] Cappellaro, P., Ramanathan, C. and Cory, D. G. “Dynamics and control of a quasi-one-dimensional spin system”. *Phys. Rev. A* **76**, 032317 (2007).
- [65] Cappellaro, P., Ramanathan, C. and Cory, D. G. “Simulations of Information Transport in Spin Chains”. *Phys. Rev. Lett.* **99**, 250506 (2007).

- [66] Zhang, W., Cappellaro, P., Antler, N., Pepper, B. *et al.* “NMR multiple quantum coherences in quasi-one-dimensional spin systems: Comparison with ideal spin-chain dynamics”. *Phys. Rev. A* **80**, 052323 (2009).
- [67] Ramanathan, C., Cappellaro, P., Viola, L. and Cory, D. G. “Experimental characterization of coherent magnetization transport in a one-dimensional spin system”. *New Journal of Physics* **13**, 103015 (2011).
- [68] Kaur, G., Ajoy, A. and Cappellaro, P. “Decay of spin coherences in one-dimensional spin systems”. *New Journal of Physics* **15**, 093035 (2013).
- [69] Doronin, S. I., Vasil’ev, S. G., Samoilenko, A. A., Fel’dman, E. B. *et al.* “Dynamics and relaxation of multiple quantum NMR coherences in a quasi-one-dimensional chain of nuclear spins ^{19}F in calcium fluorapatite”. *JETP Letters* **101**, 613–617 (2015).
- [70] Bochkin, G., Fel’dman, E. and Vasil’ev, S. “The exact solution for the free induction decay in a quasi-one-dimensional system in a multi-pulse NMR experiment”. *Physics Letters A* **383**, 2993–2996 (2019).
- [71] Leroy, N., and Bres, E. “Structure and Substitutions in Fluorapatite”. *European Cells and Materials* **2**, 36–48 (2001).
- [72] Cho, G. and Yesinowski, J. P. “ ^1H and ^{19}F Multiple-Quantum NMR Dynamics in Quasi-One-Dimensional Spin Clusters in Apatites”. *The Journal of Physical Chemistry* **100**, 15716–15725 (1996).
- [73] Hahn, E. L. “Spin Echoes”. *Phys. Rev.* **80**, 580–594 (1950).
- [74] Doherty, M. W., Manson, N. B., Delaney, P., Jelezko, F. *et al.* “The nitrogen-vacancy colour centre in diamond”. *Physics Reports* **528**, 1–45 (2013).
- [75] Balcar, E. and Lovesey, S. W. *Theory of Magnetic Neutron and Photon Scattering*, (Clarendon Press, 1989).
- [76] Wang, P.-K., Slichter, C. P. and Sinfelt, J. H. “NMR Study of the Structure of Simple Molecules Adsorbed on Metal Surfaces: C_2H_2 on Pt”. *Phys. Rev. Lett.* **53**, 82–85 (1984).
- [77] Pennington, C. H., Durand, D. J., Slichter, C. P., Rice, J. P. *et al.* “NMR measurement of the exchange coupling between $\text{Cu}(2)$ atoms in $\text{YBa}_2\text{Cu}_3\text{O}_{7-\delta}$ ($T_c = 90$ K)”. *Phys. Rev. B* **39**, 274–277 (1989).

- [78] Slichter, C. P. “Magnetic Resonance Studies of High Temperature Superconductors”. In Schrieffer, J. R. and Brooks, J. S., eds., “Handbook of High-Temperature Superconductivity”, chap. 5, pp. 215–256, (Springer New York, 2007).